EQUILIBRIUM AND KINETIC BEHAVIOR OF THE γ/β INTERPHASE BOUNDARY IN Cu-Zn ALLOYS

EQUILIBRIUM AND KINETIC BEHAVIOR OF THE γ/β INTERPHASE BOUNDARY IN Cu-Zn ALLOYS

by

DONALD EDGAR STEPHENS, B.Eng.

A Thesis

Submitted to the School of Graduate Studies

in Partial Fulfilment of the Requirements

for the degree

Doctor of Philosophy

McMaster University

December 1972

DOCTOR OF PHILOSOPHY
(Metallurgy & Materials Science)

McMaster University
Hamilton, Ontario

TITLE: Equilibrium and Kinetic Behavior of the γ/β Interphase Boundary in Cu-Zn. Alloys

AUTHOR: Donald Edgar Stephens, B.Eng. McMaster University

SUPERVISOR: Professor G. R. Purdy

NUMBER OF PAGES: xiii, 151

SCOPE AND CONTENT:

The equilibrium behavior of the boundaries separating the β and γ crystalline phases in the copper zinc alloy system is investigated by measuring the magnitude, the relative anisotropy and the temperature dependence of the interfacial energies. A model, consistent with the interfacial energetics, is proposed and supported by observations of misfit dislocations at the boundary. The migration kinetics of the γ/β interface are determined for both dendritic and polyhedral morphologies and the atomic mechanisms of growth are inferred from the internally faulted ordered γ precipitates.

ACKNOWLEDGEMENTS

I would like to express my appreciation to Professor G. R. Purdy for his guidance and help throughout the many phases of this study. I also wish to thank many of the faculty, graduate students, and technical staff in the Department of Metallurgy and Materials Science for their helpful suggestions and aid, and to thank my wife for her continuing moral support.

Finally, I would also like to express my gratitude for the following financial support: the Ontario Graduate Fellowship Foundation, the Department of Metallurgy and Materials Science (in the form of graduate fellowships) and the National Research Council of Canada (in the form of research grants to Professor Purdy).

TABLE OF CONTENTS

LIST OF TABLES

LIST OF ILLUSTRATIONS

INTRODUCTION

The objective of this investigation is to examine, as fully as possible, the static and dynamic behavior of the boundary separating the β and γ crystalline phases in the copper zinc system; specifically, to examine the factors contributing to the interfacial energy of the stationary semi-coherent γ/β boundary and the factors controlling the mobility of the boundary during precipitate growth.

The γ/β interface separates epitaxially oriented bulk phases of slightly differing lattice parameters; the resulting structural disregistry is accommodated by a dislocation network at the boundary. The major components of the interfacial energy arise from this dislocation network and from the excess atom bond energies across the interface. The latter contribution is estimated by the cutting and juxtaposing of the β and γ lattices. This has allowed a simple model to be developed which is in accord with the measured magnitude, anisotropy, and temperature dependence of the interfacial energy.

Interface migration necessitates the motion of the dislocation network which, in the ordered γ lattice, results in the formation of an antiphase boundary (A.P.B.). The A.P.B.'s provide a marker for the kinetic measurements and indicate the mechanism of interface advance.

CHAPTER 1

CRYSTALLINE INTERFACES: PROPERTIES OF STATIONARY BOUNDARIES

The concept of interfacial free energy was developed in the original work of Gibbs and provides the basis for the present understanding of surface properties. Gibbs considers a system composed of a planar interface separating two regions of a bulk phase. By differentially and reversibly displacing the system, the first law of thermodynamics yields the variation in internal energy:

$$dE = TdS = PdV^B + \mu_i dn_i + \gamma dA \qquad (1.1)$$

where T is temperature, S is entropy, P is pressure, V is volume, μ_i is the chemical potential of the i^{th} species, n_i is the number of molecules of the i^{th} species, γ is the interfacial energy, and A is the area. The properties are considered to be uniform throughout the bulk phase and discontinuous at a region of infinitesimal thickness which is termed the Gibbs' dividing surface. This allows the differential quantities of equation (1.1) to be written as the sum of the bulk and surface excess quantities. These are denoted by the superscripts B and S respectively.

Thus, $$dE = dE^B + dE^S \qquad (1.2)$$

where $$dE^B = TdS^B + \Sigma\mu_i dn_i^B = PdV^B \qquad (1.3)$$

$$dE^S = TdS^S + \Sigma\mu_i dn_i^S + \gamma dA \qquad (1.4)$$

Introducing the Helmholtz free energy $F = E - TS$ or

$$dF = dE - TdS - SdT \tag{1.5}$$

leads to the expression

$$dF^S = -S^S dT + \Sigma \mu_i dn_i^S + \gamma dA \tag{1.6}$$

which can be regarded as the basis for most theoretical and experimental studies of interface properties. The term $\Sigma \mu_i dn_i^S$ leads to expressions useful in dealing with interface segregation or adsorption and the term γdA allows consideration of the specific surface energies.

Anisotropies in these quantities, either through preferential adsorption on certain crystallographic planes or, as occurs in crystalline solids through the intrinsic orientation dependence of γ, leads to a shape tending to minimize the excess surface free energy.

The equilibrium shape-energy relation for:

$$\gamma = \left(\frac{\partial F}{\partial A}\right)_{T,V,n_i} \tag{1.7}$$

has been determined from the calculus of variations in two dimensions by Burton et al (1950) and in three dimensions by Landau and Lifshitz (1961). As Wulff (1901) first showed, the solution requires the minimum energy morphology to satisfy the relation:

$$\frac{\gamma_{hkl}}{\lambda_{hkl}} = K \tag{1.8}$$

That is, the perpendicular distance λ_{hkl} of the surface (hkl) from the centre of the body (referred to as the Wulff centre) is directly proportional to the surface tension of that surface. An equivalent statement in terms of a geometric

construction from the polar plot of the orientation dependence of γ was also proposed. In the Gibbs-Wulff construction, a plane perpendicular to each radius vector is constructed at the γ surface; the inner envelope of all these planes is geometrically equivalent to the equilibrium particle form.

Determinations of equilibrated shapes in solid fluid systems were first systematically considered by Sundquist (1964) who observed the equilibrium morphologies of thin metal foils which were vapor annealed on inert substrates. Winterbottom (1967) extended Wulff's expression to include the effect of possible interactions between the equilibrated particles and the substrate. Most subsequent studies have avoided these interactions by determining the shapes of equilibrated bubbles or voids introduced into a metal foil by such techniques as ion bombardment (Nelson, Mazey and Barnes, 1965), creep cavitation (Farrel, Loh and Stiegler, 1967), solidification (Saunders and West, 1969) and neutron irradiation (Barnes, 1964). These studies have allowed the anisotropic behavior of the interfacial free energy of relatively contamination free internal surfaces to be determined for cubic and hexagonal lattices (Miller, Carpenter and Chadwick, 1969).

The technique has been extended to solid/liquid systems by Miller and Chadwick (1969) who studied the morphologies resulting from entrapped liquid droplets; it is extended to solid/solid systems in the present investigation by choosing a precipitate without a long range strain field. The effect of strain fields in most solid

precipitate-matrix systems prevents the attainment of an equilibrium morphology determined by the interfacial energy.

The isolated equilibrium morphologies are a result of minimizing the total surface energy. Similar minimum energy configurations tend to result when surfaces intersect to form junctions. A concept of pseudoequilibrium occurring between grain and interphase boundaries by the geometric balance of surface free energies (or surface tensions) was proposed by C. S. Smith (1948). By considering the intersection of three boundaries separating phases 1, 2 and 3 with respective dihedral angles θ_1, θ_2, and θ_3, Herring (1951) has derived the following relations between the interfacial energies, γ_{ij}:

$$\gamma_{12} = -\gamma_{13} \cos \theta_1 - \gamma_{23} \cos \theta_2 + \frac{\partial \gamma_{13}}{\partial \theta_1} \sin \theta_1 + \frac{\partial \gamma_{23}}{\partial \theta_2} \sin \theta_2 \qquad (1.9)$$

$$\gamma_{13} = -\gamma_{23} \cos \theta_3 - \gamma_{12} \cos \theta_2 + \frac{\partial \gamma_{12}}{\partial \theta_2} \sin \theta_1 + \frac{\partial \gamma_{23}}{\partial \theta_2} \sin \theta_3 \qquad (1.10)$$

$$\gamma_{23} = -\gamma_{13} \cos \theta_3 - \gamma_{12} \cos \theta_2 + \frac{\partial \gamma_{13}}{\partial \theta_3} \sin \theta_3 + \frac{\partial \gamma_{12}}{\partial \theta_2} \sin \theta_2 \qquad (1.11)$$

The terms $\frac{\partial \gamma}{\partial \theta}$ behave as applied moments, giving a rotational torque which tends to bring the boundary into low energy orientations. When γ is isotropic, the expressions can be recast to Smith's original form:

$$\frac{\gamma_{12}}{\sin \theta_3} = \frac{\gamma_{13}}{\sin \theta_2} = \frac{\gamma_{23}}{\sin \theta_1} \qquad (1.12)$$

Hoffman and Cahn (1971) have proposed a vector function $\xi(\tilde{n})$, to account for both surface tension and surface torque effects. The ξ vectors for surfaces of various orientations are equivalent to the radius vectors of the corresponding Gibbs-Wulff form. The vector formulation also becomes preferable in the analysis at point junctions as the number of independent variables decreases.

The anisotropic behavior of the specific interfacial free energy in crystalline solids is attributed to the orientation dependence of atomic bond strengths. The resulting pairwise interaction model (Herring),

$$\gamma_{hkl} = \tfrac{1}{2}(N_1 + \Sigma N_i e_i)\phi_1 \qquad (1.13)$$

assumes that the lattice energy of a crystal is obtained through the summation of all pair interactions. N_i is the number of i^{th} nearest neighbours intersecting a unit area of (h,k,l) surface; ϕ_1 is the nearest neighbour bond energy and $e_i = \phi_i/\phi_1$, thus the calculation of the anisotropy of γ requires that only the relative bond energies, e_i, be known. Mackenzie, Moore and Nicholas (1962) have calculated the broken bond densities for most of the elemental crystal structures. The pairwise interaction model was designed to account for the number of atomic bonds broken in perfect crystals at O K. At elevated temperatures Burton and Cabrera (1950) predicted a cooperative roughening phenomenon. As the surfaces become atomically rough, the crystallographic orientations are less important and more spherical shapes result. The terrace - ledge - kink model offers a structural model

for singular (flat), vicinal (stepped) and non-singular (kinked) surfaces and provides mechanisms, such as additional kink or ledge formation, for the surface roughening. The roughening can occur either with increased temperature or with impurity segregation.

At present, these two models, the pairwise interaction model and the terrace - ledge - kink model, offer the most tractable methods of analyzing the orientation dependence and the temperature dependence of surface energies in solid/fluid systems.

For solid/solid interfaces the pair interaction model is applicable to coherent boundaries by replacing the broken bond potential with an appropriate atomic interaction potential. Additional structural parameters, however, characterize the interface and affect the energy associated with it.

Besides the anisotropy of surface energies stemming from the orientation of the boundary (γ plot), there exists the possibility of misorientation and structural changes between the two bulk lattices (θ plot). The resulting interfacial disregistry can be accommodated either elastically or by a type of dislocation array.

A review by Kinsman and Aaronson (1972) on the structure of solid-solid interfaces has shown the similarities in the types of dislocations occurring at grain and interphase boundaries. When the dislocations provide accommodation for a small amount of misorientation or misfit, the Burger's vectors tend to be those of the matrix dislocations. As the

interfacial disregistry increases, the interfacial dislocations tend to have Burger's vectors peculiar to the boundary.

Read and Schockley (1950) developed a simple model to predict the interfacial energy based on the dislocation density required to relieve a misorientation, θ. The analysis applies to low angle symmetric tilt (described by a parallel array of edge dislocations) and to twist (described by two orthogonal sets of screw dislocations) boundaries and yields an energy per unit area:

$$E_b = E_o\theta(A - \ln \theta) \tag{1.14}$$

where

$$E_o = \frac{Gb^2}{4\pi(1-\nu)} \tag{1.15}$$

$$\theta = b/D \tag{1.16}$$

$$A = \ln \alpha \tag{1.17}$$

G = shear modulus, b = Burger's vector, ν = Poissons ratio D = dislocation spacing and α = constant whose exact value could be determined from an exact integration of the stress field due to all the dislocations.

In high angle boundaries, various degrees of lattice coincidence (Frank, 1950) occur as a result of variations in either crystal misorientation or boundary position. The degree of lattice coincidence Σ, is described by the reciprocal of the fraction of sites coinciding (Brandon, 1966), thus orientations of maximum lattice coincidence correspond to a cusp in the interfacial energy. Small departures from the cusp orientation lead to the formation of bands of good and bad fit. These bands have a unique displacement vector and are termed grain boundary dislocations (Levy, 1969; Ishida, 1969).

Irrational habit planes between solid phases such as those observed for Widmanstatten precipitates by Malcolm and Purdy (1966) contain similar regions of good and bad atomic fit and presumably allow a parallel description by interphase boundary dislocations (Kinsman and Aaronson, 1971).

The experimental observations of grain boundaries in naturally occurring systems are complemented by the carefully controlled, artificially prepared, tilt and twist boundaries of Schober and Baluffi (1969, 1970, 1971). Their investigations have clearly shown the presence of unique grain boundary dislocations.

Equivalent control of interphase boundary parameters describing crystal misorientation, boundary position and lattice misfit has not yet evolved. The observations to date have been of a random nature in that the individual parameters had to be determined in each case. The effect of crystal misorientation is presumed to be similar to that in grain boundaries. In solid state transformations the precipitate orientation usually results from the nucleation event and often leads to the development of unique relationships in crystallographic orientation. As a result most quantitative determinations of interphase misfit dislocation networks are for specific boundary planes which separate phases of fixed misorientation. By appropriate alloying additions, the difference in lattice parameters can be varied; the resulting control of misfit is useful in the study of the density of the interphase dislocations. Cline, Walter,

Koch and Osika (1971) have controlled the misfit in NiAl-Cr eutectics by the addition of Mo and have studied the resulting structures as a function of misfit.

The relief of lattice mismatch by a dislocation array depends on the component of the Burger's vector in the edge orientation in the boundary plane. Weatherly and Nicholson (1967) have shown that one-dimensional mismatch such as that occurring in some needle shaped precipitates could be accommodated by edge loops of a single Burger's vector. Two-dimensional misfit found in disc-shaped precipitates required at least two dislocation arrays. Similarly, a three-dimensional precipitate, such as a cube or a sphere, would require a minimum of three sets of dislocations. The combination of these three sets yields different efficiencies of misfit accommodation as the interface orientation is varied. Investigations into the various interface structures for the different morphologies have been reported. Studies involving needle shaped precipitates include:

A in AlMgSi and	
β' in Al Cu Mg	(Weatherly and Nicholson, 1967)
Cr in CuCr	(Hall, Aaronson and Kinsman, 1972)
α' in Al Zn	(Aaronson, Laird, Kinsman, 1970)

The interface networks at the following disc shaped precipitates are:

θ',θ in AlCu	(Weatherly, 1970,1971; Weatherly and Sargent, 1970; Aaronson and Laird, 1968)
γ' in AlAg	(Hren and Thomas, 1963; Laird and Aaronson, 1967, 1969)

η in CuSi (Kinsman and Aaronson, 1971)

UC_2 in UC (Whitton, 1964)

US_2 in US (Kinsman, Aaronson, Laird, 1967)

Spherical precipitates include:

γ' in Ni_3 (Ti Al) (Weatherly and Nicholson, 1967)

Co in CuCo (Phillips, 1966)

The results of most studies have indicated that interphase dislocations are primarily of edge character, exhibiting wide variations in their effectiveness of misfit accommodation. This is mainly due to the mechanism of coherency loss.

The interface dislocations result either from nucleation at the interphase boundary or from the acquisition of existing lattice dislocations. The nucleation of interfacial dislocations depends on the loss of coherency criteria (Brooks, Ashby and workers). Brown and Woolhouse (1970) have shown that, for a misfitting spherical particle, a critical misfit of 0.05 is necessary for the nucleation of interface dislocations by prismatic loop punching. The elastic stress necessary for dislocation nucleation also provides a driving force for the climb of lattice dislocations to the boundary. The mechanisms are competitive and depend on the supply of appropriate matrix dislocations. Rastogi and Ardell (1971) have investigated γ' precipitates from α NiSi alloys and found that, for particle sizes >0.2 μm, the misfit of 0.003 was accommodated by the adsorption of matrix dislocations. Once the dislocations are in the boundary, dislocation interactions

cause their rearrangement into networks. It also appears possible that the matrix dislocations can spiral around the precipitates and form an array of dislocation loops. The interface dislocations which originate in the lattice are dependent in accommodating lattice mismatch on the original Burger's vector. This can result in certain "intruder" dislocations at the interface which offer little contribution to relief of misfit (Aaronson and Kinsman, 1970).

The acquisition of matrix dislocations is dependent on the matrix dislocation density and, in certain cases, on the rate of interface advance. A potential oversupply results during Widmanstatten precipitate tip migration. Hawbolt (1971) has recently investigated the dislocation accumulation ahead of a growing α rod in β brass. The interface structure occurring during growth conditions such as this requires further investigation.

In addition to accommodating misfit, the interfacial dislocations with displacement components out of the boundary may provide built-in nucleation sites for the lateral growth mechanism of interface advance. The dislocation (or partial) is often coincident with the step and thereby allows observations of ledge migration during growth by in-situ heating in the electron microscope (Aaronson, Kinsman and coworkers (1968, 1969); Weatherly (1971)).

CHAPTER 2

DYNAMIC PROPERTIES OF INTERPHASE BOUNDARIES

The increased knowledge of the structure of interfaces can be combined with the migrational characteristics of interfaces to enhance the understanding of phase transformations, grain growth and recrystallization. The interface mobility is a structurally dependent property and a function of the driving force. By determining appropriate values for the mobility and for the driving force, the growth kinetics can be analyzed.

In phase transformations, the interface mobility is associated with the deviation from the local equilibrium required to advance the interface. It is possible to regard the velocity of the boundary either in terms of this deviation (Shewmon, 1965);

$$v = \mu o(C_{\beta} - C_i)^n \qquad (2.1)$$

or in terms of the remaining supersaturation driving the diffusional process (Zener, 1949):

$$v = \frac{D_{eff}\ \nabla Cn}{(C_i - C\alpha)} \qquad (2.2)$$

where C_{β} and C_{α} are the equilibrium interface concentrations in the β and α phases respectively.

C_i is the actual interface concentration in the β phase

μo is a mobility coefficient

n describes the velocity dependence of the deviation from local equilibrium

D_{eff} is a corrected diffusion coefficient

∇Cn is the concentration gradient normal to the interface.

Interphase boundary migration usually requires the coupling of the diffusion fluxes (Russell,1970):

$$\frac{J_A}{J_B} = X \tag{2.3}$$

where J_A/J_B is the ratio of fluxes of A and B atoms. The chemical diffusity determined by semi-infinite diffusion couple experiments corresponds to vacancy sources and sinks being readily available (Baluffi and Seigle, 1955). This implies that the interface must be able to absorb or generate a vacancy flux equivalent to the difference in atomic fluxes. This is clearly not possible for many interfaces (Li, Blakely and Fiengold, and Russell, 1970). Russell obtained flux relations for the constraint of equation 2.3:

$$J_A = -\left(\frac{D_A D_B}{XD_A C + D_B(1-C)}\right)\frac{\partial c}{\partial x} \tag{2.4}$$

$$J_B = -X\left(\frac{D_A D_B}{XD_A C + D_B(1-C)}\right)\frac{\partial c}{\partial x} \tag{2.5}$$

where the bracketed term represents the effective diffusivity, D_{eff}, and is a function of the individual diffusion coefficients

D_A and D_B and of the matrix composition c.

Cahn (1961) has proposed that an allowance must also be made for the effect of coherency strain energy. In rapidly propagating systems, the large concentration gradient may necessitate corrections for the stored elastic energy due to self stressing as well as for the incipient surface energy associated with this steep concentration profile. Fick's second law:

$$\frac{dc}{dt} = \tilde{D} \frac{d^2c}{dx^2} \tag{2.6}$$

becomes (Cahn):

$$\frac{dc}{dt} = \tilde{D}\left\{\left[1 + \left(\frac{2n^2Y}{\partial^2 f/\partial c^2}\right)\right] \frac{d^2c}{dx^2} - \left[\frac{2K}{\partial^2 f/\partial c^2}\right] \frac{d^4c}{dx^4}\right\} \tag{2.7}$$

where f is the Helmholtz potential per unit volume

n is an expansion coefficient with composition

K is the gradient energy coefficient

and for cubic crystals:

$$Y|k,k,l| = \tfrac{1}{2}(C_{11} + 2C_{12}) \times \left(3 - \frac{C_{11} - 2C_{12}}{C_{11} - 2(C_{11} - C_{12} - 2C_{44})(h^2k^2 + h^2l^2 + k^2l^2)}\right) \tag{2.8}$$

The latter relation leads to an anisotropic effective diffusion coefficient and possibly explains preferred growth directions in early stages of precipitate shape development.

The development of precipitate morphologies also follows from the inherent instabilities accompanying a gradient of supersaturation. This is analogous to a gradient leading to

the planar interface breakdown found in constitutional supercooling (Chalmers and Rutter,1953). Mullins and Sekerka (1963,1964) have developed an elegant quantitative description of interface stability by superimposing a perturbation of infinitesimal amplitude on a moving boundary and investigating the wavelength dependence of growth. The induced curvatures due to the perturbations give rise to variations in the equilibrium interface concentrations. This capillarity effect, given by the Gibbs Thomson expression $C_\beta^r = C_\beta^o(1 + \Gamma K)$ causes the decay of very short wavelength perturbations. Longer wavelengths grow increasingly more slowly because of insufficient time for lateral diffusion; hence, maximum growth results for intermediate wavelengths. Mullins and Sekerka have shown that both planar and spherical shapes (at larger radii) develop instabilities during isothermal advance. The magnitude of the diffusion gradient normal to the interface determines the propensity towards instability, so any factor affecting the gradient has a corresponding effect on the interface instability. The major factors contributing towards the stabilization of the shape of an advancing interface are capillarity, interface diffusion, interface reaction and highly anisotropic interfacial energies.

Besides giving a critical curvature for the growth of perturbations, capillarity also provides the driving force for surface diffusion. The effect of surface diffusion on the stability has been considered quantitatively by Shewmon (1965), Nichols and Mullins (1965) and Coriell and Parker (1966). Qualitatively, interfacial diffusion reduces the

lateral gradients set up by the perturbation, thereby decreasing the tendency for the perturbation to grow.

Interface kinetics is a lumped parameter term used to describe the chemical reaction necessary for interface advance. A critical amount of free energy is necessary for interface migration. Once the supersaturation exceeds a certain value, the interface will advance either in a continuous mode or by the lateral propagation of steps (Cahn, 1960). When the interface is advancing normal to itself, the interface kinetic term arises from a deviation from local equilibrium occurring at the interface. The corresponding decreased diffusion gradient is a stabilizing influence (Shewmon 1965; Nichols and Mullins 1965). During interface advance by the lateral growth mechanism, the stationary boundary normal to the overall advance direction can support a chemical potential difference across the boundary.

The effect of anisotropic interfacial energy on the interface stability depends on the degree of anisotropy. Cahn (1966) has shown that weakly anisotropic energies are ineffective in stabilizing an interface. The perturbations that do develop, however, will be distorted and will reflect the characteristics of the equilibrium shape. As the anisotropy of surface free energy increases, the orientation of the boundary becomes more important. Boundaries in the cusp orientation may be stabilized by strong anisotropy since any shape perturbation must involve a type of nucleation (Shewmon, 1965). Boundaries not in cusp orientations readily develop perturbations exhibiting low energy facets; however further growth of the

perturbations is then limited.

Sufficiently large driving forces result in interface motion and microscopic shape oscillations. The subsequent growth of the instabilities can occur whenever a gradient exists ahead of the interface; the only absolute stabilizing factor therefore is in the limit of pure reaction control. During diffusional growth, the oscillations are believed to lead to formation of dendrite or needle morphologies. The kinetics of dendrite and needle growth was first formulated by Zener (1949) who argued that solute rejection would occur over a constant distance of approximately twice the tip radius. This implied a constant lengthening rate:

$$v = - \frac{\tilde{D}}{(C_\beta - C_\alpha)} \frac{(C_B - C_O)}{r} \left(1 - \frac{r_c}{r}\right) \qquad (2.9)$$

where the last term accounts for the effect of capillarity in reducing the gradient of more sharply pointed precipitates. When $r = r_c$, the critical radius for nucleation, the diffusion gradient vanishes and $v = 0$. There exists a multiplicity of solutions as an infinite number of selections of velocity, v, and tip radius, r, are possible.

The mathematical description of dendritic growth was first attempted by Ivanstov (1947) who showed the growth shape of an isothermal dendrite was a paraboloid of revolution. Since the growth rate is determined uniquely by thermal diffusion, the solution is obtained in terms of $v \cdot r$ pairs.

Temkin (1960) considered a non-isothermal dendrite modified for capillarity and interface kinetics yielding an interface temperature T:

$$T = T_m - \Delta T_E - \Delta T_K \tag{2.10}$$

where T_m = is the equilibrium melting temperature

ΔT_E = is the decrease in equilibrium melting temperature due to curvature

ΔT_K = is the kinetic undercooling required for interface migration and is a function of the normal interface velocity.

Temkin assumed the Ivanstov shape and found the Laplacian solution to the diffusion equation. Besides yielding an infinite set of v.r pairs, Temkin's solutions exhibited a maximum in the function v vs. r. The value of v giving a unique r was chosen as optimum; this corresponds to invoking the maximum velocity principle.

Successive refinements (Horvay and Cahn, 1961; Bolling and Tiller, 1961; Kotler and Tarshis, 1969) have assumed the Ivanstov shape and the Temkin interface temperature and have led to the rigorous mathematical solution to the complete heat flow equation (Trivedi, 1970; Holzmann, 1970):

$$(T_m - T_\infty)\,\frac{C_L}{\Delta H} = P_L\, e^{P_L}\, \varepsilon_1(P_L)\left[1 + \frac{\gamma}{V_r 2}\, L_2(p) + \frac{1}{\mu_o r}\, L_1(p)\right] \tag{2.11}$$

where T_m = equilibrium melting temperature

T_∞ = temperature of the supercooled bath

C_L = heat capacity of the liquid

ΔH = enthalpy of formation

P_L = thermal Peclet number of the liquid = $\frac{Vr}{2D}$,

$\varepsilon_i(p_1)$ = exponential integral function

and the first bracketed term gives the Ivanstov solution, the second accounts for curvature and the third term considers interface kinetics. Temkin's analysis yields $L_1(p)$ and $L_2(p)$ constants while Trivedi's solution determines these parameters as complicated functions of the peclet number.

By replacing the heat equation with the diffusion equation, the growth of a dendrite needle from a supersaturated solid solution is (Trivedi, 1970):

$$\Omega_o = pe^{P}E_1(p) \left[1 + \frac{V}{V_c} \Omega_o R_1(P) + \frac{rc}{r} \Omega_o R_2(P) \right] \qquad (2.12)$$

where Ω_o is the dimensionless supersaturation

$= (C_o - C_\infty)/(C_o - C_P)$

P is the dimensionless velocity = Vr/2D

V_c is the limiting velocity = $\mu o(C_o - C_\infty)$

$R_1(p)$ and $R_2(p)$ are complex functions tabulated by Trivedi.

The growth kinetics of dendrites and rods have been measured by quantitative metallographic studies of quenched specimens of proeutectoid ferrite in steel (Townsend and Kirkaldy, 1969) and of α rods in β brass (Repas and Heheman, 1967; Bainbridge and Doherty, 1970; and Purdy, 1971). The results indicated that the lengthening kinetics were consistent with the maximum velocity principle, as applied to the volume diffusion control model.

An interface advancing by the lateral velocity, v, of linear ledges of height, a, and spacing b, has a normal rate of migration G_L:

$$G_L = \frac{av}{b} \tag{2.13}$$

Jones and Trivedi have determined the diffusion controlled ledge velocity by computing the solute diffusion field around a step. They found the solution could be represented by:

$$v = \frac{2D}{3a} \Omega_o \tag{2.14}$$

Normally it is not possible to supply the necessary ledges without a nucleation step. Suggested mechanisms include: repeated two dimensional nucleation (Cahn, Hillig and Sears, 1964):

$$G_N = aAN \tag{2.15}$$

where A is the interface area

N is the rate of nucleation per unit area of boundary

or formation of a pole dislocation and the subsequent growth by spiral ledges (Burton and Cabrera, 1950)

$$G_S = \frac{\omega a}{2\pi} \tag{2.16}$$

where ω is the angular velocity of the spiral. The spiral mechanism has been observed by Weatherly (1971) on flat Θ surfaces in Al-Cu alloys using hot stage electron microscopy. Similar studies in alternate systems by Aaronson, Kinsman and workers (1967, 1968, 1969) have found considerable randomness to the spacing, height and motion of ledges.

CHAPTER 3

RELEVANT PROPERTIES OF THE COPPER ZINC SYSTEM

The objectives of the investigation involve determining, as fully as possible, the equilibrium and kinetic characteristics of a mobile semicoherent boundary separating the β and γ crystalline phases in the copper-zinc alloy system. The structural and chemical similarity of the two phases, and the unique orientation relationship:

$$\{110\}_{\beta} \;//\; \{110\}_{\gamma}$$

$$\langle 111\rangle_{\beta} \;//\; \langle 111\rangle_{\gamma}$$

allow a theoretical model of the boundary to be developed consistent with experimental observations.

The β phase is a body centered cubic structure, based on the stoichiometric 3/2 electron compound CuZn, and has a lattice parameter 2.9539 A (Massalski and Kittl, 1963). At higher temperatures, a random atom distribution exists. An ordering reaction occurs between 454°C and 468°C (Hansen, 1958) to yield the CsCl structure which results in having the corner sites occupied by one atomic species and the body-centered positions occupied by the other. At lower temperatures (20°C to -131°C) a martensitic transformation gives rise to an orthorhombic structure (Jolley and Hull, 1964).

The γ phase is a 21/13 electron compound having Cu_5Zn_8 stoichiometry. The structure may be described in terms of two clusters, each comprising 26 atoms; one is centered at the origin (0,0,0) and the other is centered at (½,½,½). The lattice is usually considered a distorted defect superstructure of the body centered cube of which 27 pseudo-cells are stacked together in a 3x3x3 array with the two sites at the supercell corners and body centered positions left vacant (Pearson, 1972). The atom positional parameters, determined by Bradley and Gregory (1931), show the atoms considerably displaced from their ideal positions. The structure, illustrated in Fig. 1, contains four independent sites. Neutron diffraction studies of Heidenstam, Johansson and Westman (1968) indicate that zinc and copper atoms collapse around a copper vacancy to form a cluster built up of zinc atoms on the inner tetrahedral, I.T., and cubo-octahedral, C.O., sites and copper atoms on the outer tetrahedral, O.T., and octahedral, O.H., positions. The structure exhibits a predominance of unlike nearest neighbour contacts and may be described as built up of interpenetrating distorted icosahedra (Pearson, 1972).

Uncertainty existed as to the limits of solubility in the temperature range 300°C to 500°C. The phase diagram in Hansen (1958) indicated decreasing solubility on the 300° to 400°C regime while Elliott (1961), reported increasing solubility due to a eutectoid reaction at 250°C. The extent of the β phase field was redetermined in this investigation

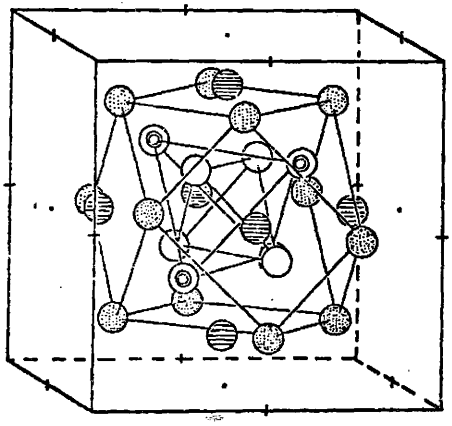

= IT	0.10	0.10	0.10
= OT	-0.17	-0.17	-0.17
= OH	0.35	0	0
= CO	0.30	0.30	0.05

Fig. 1: The atomic distribution and positional parameters in γ brass established by neutron powder diffraction by Heidenstam et al (1968). The designation of the sites: I.T. = inner tetrahedral, OT = outer tetrahedral, OH = octahedral, CO = cubo-octahedral position

by measuring the volume fraction of γ precipitate in 52 wt% Zn specimens equilibrated within the two phase region. The results are shown in Fig. 2 as volume fraction since this also indicates the degree of supersaturation produced during up or down quenches within this temperature range. Fig. 2 demonstrates that the present experimental values agree best with those predicted from the Hansen version of the phase diagram; for a given composition, the relative supersaturation decreases steadily as the temperature is increased above 350°C. The Hansen diagram is therefore adopted for the balance of this study.

Phase stability requires that the principal minors of the matrix of elastic coefficients be positive (Callen). For cubic systems the conditions are:

$$C_{11} > 0$$

$$C_{44} > 0$$

$$C_{11}^2 - C_{12}^2 > 0$$

$$C_{11} + 2C_{12} > 0$$

$(C_{11}^2 - C_{12}^2)$ is 0.445 for β brass (as compared with 3.628 for α iron) indicating the system is on the verge of instability.

The elastic properties of β brass have been determined by McManus (1963) as a function of composition and temperature throughout the β phase field. The compositional variation near the limits of the β phase field has been questioned by Morton and Head (1970) who obtained

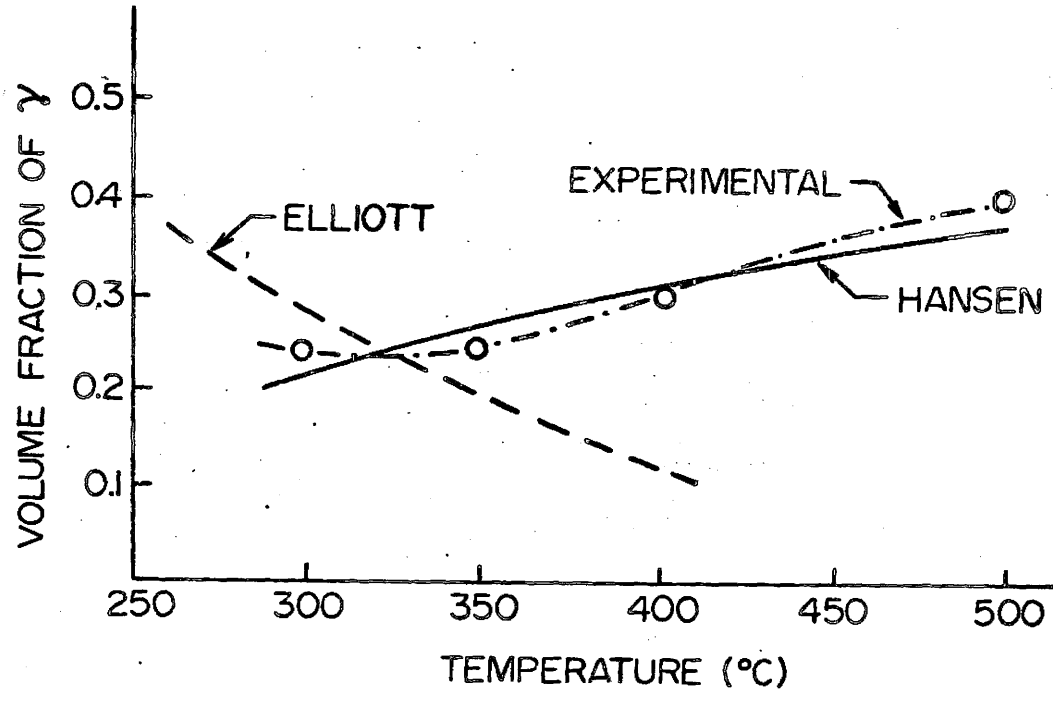

Fig. 2: The volume fraction of γ precipitates is determined as a function of temperature and the solubility compared with the data in Hansen (1958) and Elliott (1965)

relative values by considering the directional instabilities of glide dislocations. They suspect the decreased anisotropy beyond 49 at % Zn reported by McManus is due to the presence of a dispersion of γ precipitates. By choosing an appropriate composition, the temperature dependence of the elastic properties can be examined.

The results of the calculations of Young's modulus Y_{hkl} given by equation 2.8 (Cahn, 1961) are shown in Table 1. The relative values, indicating a measure of the anisotropy, are independent of temperature in the range considered. The elastic anisotropy may contribute significantly to both the equilibrium and the kinetic behavior of an interphase boundary.

Phase transformation kinetics are usually based on the rate of solute transport. The compositional and temperature dependence of the diffusion coefficients have been measured in the β phase by Landergren, Birchenall and Mehl (1956); and Kuper, Lazarus, Manning and Tomizuka (1956) and in the γ phase by Mehl and Lutz (1961).

The intrinsic and chemical coefficients, plotted in Fig. 3, are related through a function given by Darken (1948) involving a thermodynamic parameter, $\left(1 + \frac{\partial \ell n \gamma}{\partial \ell n c}\right)$, which can be determined from data in Hultgren, Orr, Anderson and Kelley (1963).

TABLE 1 Variation in elastic properties in the β phase as a function of temperature, expressed as $Y_{hkl} \times 10^{-12}$ (dynes/cm^2)

	300°C	400°C	500°C
$Y_{<100>}$	2.04	1.91	1.75
$Y_{<110>}$	2.51	2.30	2.12
$Y_{<111>}$	1.92	1.75	1.62
$\frac{Y_{<110>}}{Y_{<110>}}$	1	1	1
$\frac{Y_{<111>}}{Y_{<110>}}$	0.76	0.76	0.76
$\frac{Y_{<100>}}{Y_{<110>}}$	0.82	0.82	0.82

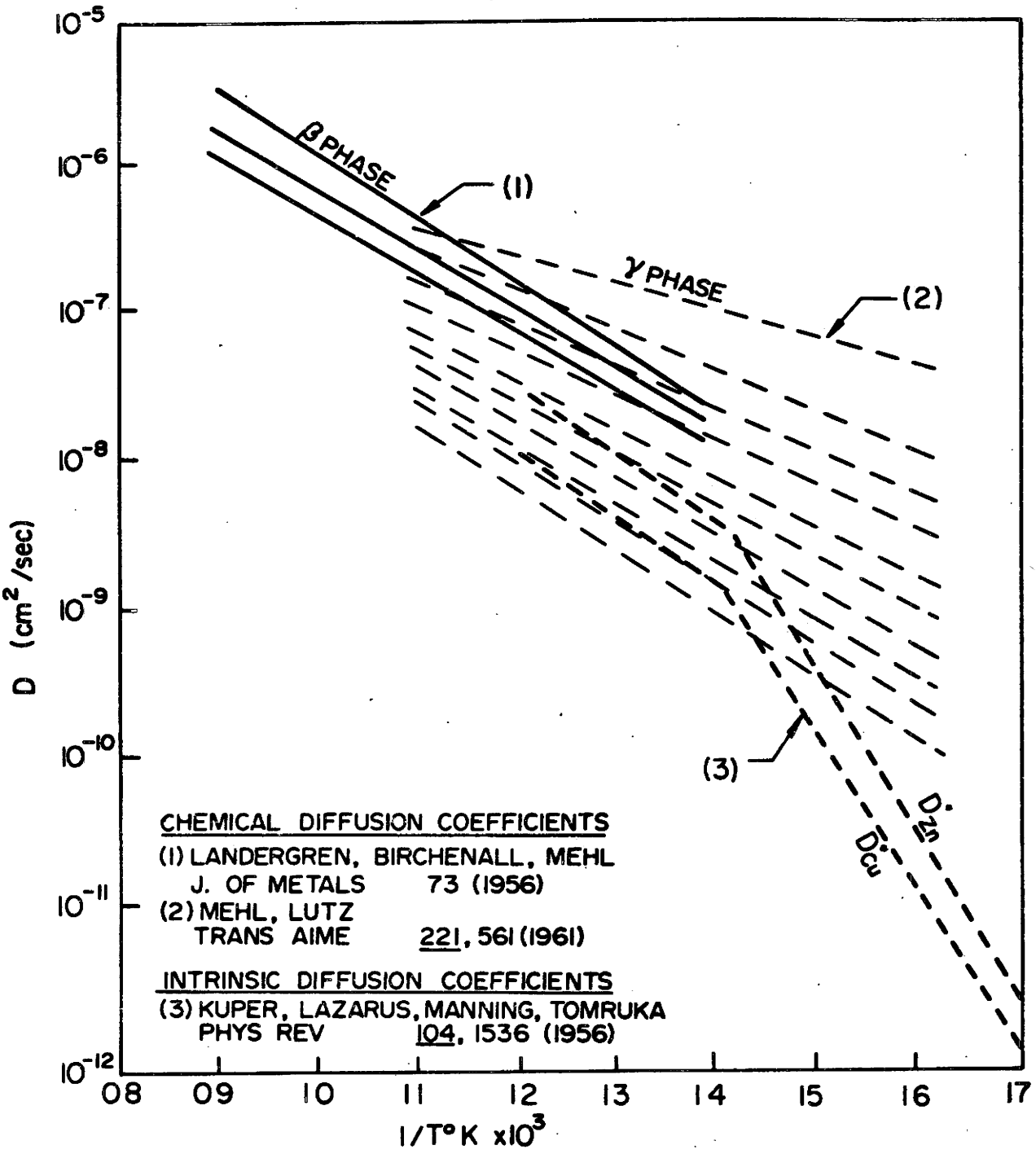

Fig. 3: The chemical and intrinsic diffusion coefficients in the β and γ phases of copper-zinc alloys are plotted as a function of temperature

CHAPTER 4

EXPERIMENTAL

4.1 Preparation of Alloys

Brass alloys having compositions shown in Table 2 were prepared from zone refined zinc and copper rods of 99.999% purity which were supplied courtesy of Cominco Product Research Centre, Sheridan Park, Ontario. Measured amounts of the metals were sealed in Vycor capsules evacuated to 10^{-5} mm.Hg and heated to 1000°C until the complete dissolution of copper in molten zinc had occurred. After agitation and quenching, the resulting 17 mm. diameter rods were checked for homogeneity by comparing the distribution of precipitates at various sections. Compositions were determined by dissolving one gram of alloy in an electrolyte (20 ml. HNO_3, 30 ml. H_2SO_4, 100 Ml. H_2O, 5 ml. H_2O_2) and electro-depositing copper on a platinum cathode. The rods were found to be homogeneous throughout their length and of the desired alloy composition.

Samples used in the transmission electron microscope studies were further vacuum cast to 5 mm. utilizing joined Vycor tubes of different diameters. The rods were then reduced to 3 mm. to fit directly into the microscope by rotation in a 25% H_3PO_4, 25% HAc, 50% HNO_3 chemical polishing

TABLE 2 Nominal compositions of alloys prepared from high purity copper, zinc and tin

Specimen No	Composition (wt/o)			Comments
	Cu	Zn	Sn	
C	49	51		β and γ phase studies
D	48	52		
E	53	47		β single phase
F	39	61		γ single phase
A				β and α phase studies
R-1	49	51		Alloys used in interface
R-2	49	48	3	stability study
R-3	56	38	6	(Robertson (1968))
R-4	50.5	45	43	
B	53	42	5	Proposed compositions
G	55	40	5	yielding zero misfit
H	53	43	4	based on Robertson's results

solution. Single crystals were required for some of the dendrite growth studies. These were grown in evacuated Vycor capsules in a vertical travelling furnace designed for directional solidification experiments (Hone, 1970) and ideally suited to growing single crystals.

The rods were sectioned before heat treatment using the Geoscience Sea-Saw multiple wire cutter. A reciprocating array of tungsten wires in a 15 micron silicon carbide/oil abrasive slurry slices the sample with minimum deformation.

4.2 Heat Treatments

A series of experiments were undertaken to examine the precipitate morphologies of faceted γ precipitates after 500 hour isothermal treatments in low melting point 1:1 $NaNO_2$: KNO_3 salt baths. Samples were solution treated at 800°C, quenched to retain the β phase and aged at 300°C, 350°C, 400°C and 500°C. Some of the equilibrated structures were subsequently quenched to a second salt bath at a different temperature (and supersaturation) to study growth characteristics of the precipitates. The precipitation kinetics of both α and γ dendrites were compared by quenching directly to the salt baths from the single phase β region. Table 3 designates the heat treatments followed.

After appropriate heat treatments the specimens were prepared for optical microscopy and Kossel diffraction, for the scanning electron microscopy or for replica and

TABLE 3 Heat Treatments:

Purpose	Alloy	Solution Treatment Temperature	Quench	Aging for Equilibration (500 hr)	Quench	Aging for growth or dissolution (various times)
I. Equilibrium shape determination:						
a) faceted idiomorphs	D	800°C	0°C	300°C	0°C	
	D	800°C	0°C	350°C	0°C	
	D	800°C	0°C	400°C	0°C	
	D	800°C	0°C	500°C	0°C	
b) grain boundary allotriomorphs	D	800°C	0°C	350°C	0°C	
	D	800°C	500°C	500°C	0°C	
	A	800°C	500°C	500°C	0°C	
II. γ phase structural domains:						
a) γ precipitated from β matrix	C	800°C	0°C	350°C	0°C	
	C	800°C	0°C	350°C	0°C	300°C
b) γ single phase	F	800°C	0°C	350°C	0°C	
	F	800°C	0°C	350°C	0°C	300°C
III. γ/β interface structures:						
a) dendritic morphology	G	800°C	500°C	500°C	0°C	
	C	800°C	500°C	500°C	0°C	
b) faceted morphologies	C	800°C	0°C	350°C	0°C	
	D	800°C	0°C	350°C	0°C	
IV. Interface stability during growth	R-1	800°C	0°C	350°C	300°C	300°C
	R-2	800°C	0°C	350°C	400°C	400°C
	R-3	800°C	0°C	350°C	500°C	500°C
	R-4					
V. Kinetics of precipitate growth						
a) dendritic growth	A	800°C			520°C	520°C
	C	800°C			520°C	520°C
	D	800°C			520°C	520°C
b) planar interface migration	C	800°C	0°C	350°C	400°C	400°C
	D	800°C	0°C	350°C	400°C	400°C

transmission electron microscopy.

4.3 Light Microscopy and Kossel Diffraction

The morphological studies, encompassing a large number of γ precipitates, were made using the Ziess Ultraphot II metallograph coupled with Kossel microdiffraction orientation determinations using the Acton Electronprobe Analyzer. The Kossel technique (Lonsdale (1947), Morris (1968)) allowed lattice orientations of the precipitates and the matrix to be measured and the micrographs of the γ precipitates to be correlated to sections of their equilibrium dodecahedral shape. The edge curvatures of the faceted precipitates were measured and a three-dimensional model of shape and of relative surface free energies was constructed. Observations of grain boundary allotriomorphs allowed an estimate of the absolute surface energies, including corrections for torque terms. The high mobility of the coherent γ/β boundary was noted as the γ precipitates grew into the grain with shared orientation. Usual metallographic procedures were followed; alcoholic ferric chloride etchant and oil immersion lens gave adequate contrast and resolution at the precipitate matrix interface.

Kossel diffraction is a useful technique in determining orientations (Bevis and Swindells,1967) and lattice parameters (Peter and Ogilvie, 1965) of crystals too small for conventional X-ray determinations because the X-ray source for Kossel diffraction is the characteristic X-ray emission due to bombardment with high energy electrons.

The high energy incident electrons which hit a crystal surface result in various interactions. The electrons that are backscattered provide the signal monitored in scanning electron microscopy . Those electrons passing through the crystal yield an image whose intensity distribution reflects the internal crystal structure. This is the basis of transmission electron microscopy. Diffraction, according to Bragg's law, gives patterns yielding crystallographic data. The deceleration of primary electrons due to lattice interactions may cause either the emission of secondary electrons or the emission of X-rays characteristic of the element present. The intensity of X-rays is proportional to the concentration of the element and is measured with the electron microprobe analyzer. Bragg diffraction is also possible with the production of secondary electrons and X-rays to give Kikuchi and Kossel lines respectively.

The pattern recorded on plane photographic film for Kossel diffraction (Fig. 4) is a gnomic projection of excess and deficit cones of X-rays with a semi-apex angle $\phi_{hkl} = 90 - \theta_{hkl}$ where θ_{hkl} satisfies the Bragg condition: $\sin \theta_{hkl} = \frac{\lambda}{2d_{hkl}}$. The observed radius on the film is $R_{hkl} \approx D \tan \phi_{hkl} = D\left(\left(\frac{2d_{hkl}}{\lambda}\right)^2 - 1\right)^{\frac{1}{2}}$ where D is the specimen to film distance. Thus a simple measurement of the radius allows the cone to be indexed. Various methods are available to give accurate orientation measurements. This requires transferring information on the film to a stereographic projection. Bevis and Swindells (1967) give an analytical

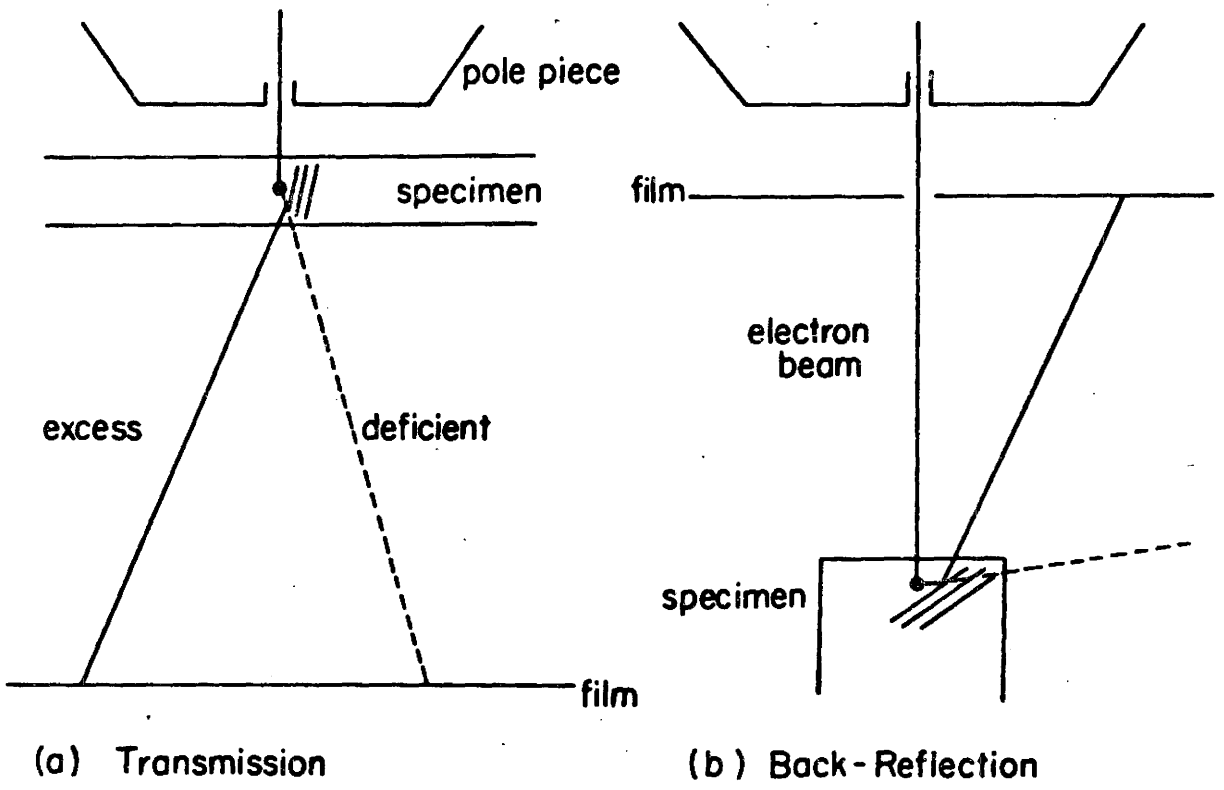

Fig. 4: The diffracted excess and deficit cones of X-rays for a) transmission and b) back reflection Kossel microdiffraction.

method; however, in most determinations a direct graphical method is sufficient. Gnomic and stereographic projections are simply related as the angles of rotation are the same, and the radial angles of the gnomic projection are twice those of the stereographic projection. The orientation of the surface normal will be located along an angular distance $\delta \approx \phi \pm \arctan (L/D)$ along a diameter from a point on the circle. By marking the film and sample (line scan of electron beam provides a contamination trace), it is a simple matter to completely specify crystal orientation.

Both back reflection and transmission Kossel patterns were obtained using the Kossel camera attachment for the Acton Microprobe. This consists of a specimen goniometer stage (translation, rotation and tilt) and film holders above and below the specimen. The back reflection mode is more awkward to use. Since the film is inside the evacuated chamber, partial shutdown and re-evacuation is required in order to change the film. In addition, the specimen can only be observed with the CRT image from back-scattered electrons or specimen current, since the specimen placement is far beyond the objective lens pole piece in order to accommodate the film holder. In back reflection the patterns have a much weaker intensity and the film must be shielded to prevent darkening from the backscattered electrons. The transmission mode yields more lines, makes use of normal probe optics and has the film mounted in an external cassette. The added advantage is that the geometry of the diffracted beam allows determination of lattice

constants. This was attempted in Cu-Zn alloys for coexisting β and γ phases by Robertson (1968); however no suitable pattern could be obtained for γ brass. The present study therefore uses the Kossel technique only for orientation measurements.

4.4 Electron Microscopy

Symmetric precipitation reactions, of α rods and γ dendrites from a supersaturated β matrix, were examined at equivalent supersaturations and temperatures to enable direct comparison of lengthening rates. The alloys were solution treated at 800°C and quenched to a salt bath at 520°C ± 5 for various times. By measuring the longest rod or dendrite, the migration distance as a function of time was obtained. The α rods were observed with a Cambridge Stereoscan II scanning electron microscope (S.E.M.) using a deep etching technique developed by Purdy (1970). A 30 gm/liter alcoholic ferric chloride etchant attacks only the β phase, leaving the α rods untouched. Purdy's observation in the scanning electron microscope yielded striking photographs of α rod formation for isothermal aging at 400°C. Preliminary studies showed that, due to extensive nucleation, it was not possible to obtain γ dendrites at 400°C for the supersaturations Purdy used. Therefore, the direct comparison was carried out at a higher temperature using a similar deep etching technique for α rod formations. Because no etchant could be found for the preferential attack in the β-γ system, the γ lengthening kinetics were measured using optical metallography.

The interface motion, induced by a small change in supersaturation, was initially studied by observing whether shape instabilities developed in a moving γ/β boundary. Samples were subjected to a duplex heat treatment, then sectioned and electropolished in 2:1 methyl-nitric acid solution at $-20^{o}C$. Single stage Au-Pt shadowed carbon replicas were made by standard evaporation techniques and removed by partial dissolution of the metal in 10% Br-methanol solution. The replicas were observed at 80 KV in the Phillips EM 300 electron microscope.

The major portion of the microscopy encompassed the determination of γ/β interface structures and the characteristics of planar interface movement. This entailed the preparation of thin films. Most conventional techniques resulted in different rates of polishing for the β and γ phases with greatest attack noted at the interface. After considerable experimentation, a jet polishing method, operated at a higher potential (20 - 100 volts), was found to be most satisfactory. The samples were sliced to discs measuring 3mm x 0.8 mm and mounted by means of an acetone soluble cement and either chemically planed (using cloth soaked in a nitric/acetic/phosphoric (2:1:1) acid solution), or mechanically abraded (600 grit paper) to a thickness of 0.04 to 0.08 mm. After ultrasonic cleaning in acetone, the discs were placed in a PTFE holder and jet polished. A 30% phosphoric acid electrolyte was fed through a 0.6 mm diameter probe anode to the specimen. The probe position

was adjustable along three orthogonal directions to allow centering the jet and to control the polishing profile by varying the probe to specimen distance. As the distance decreased, the profile became increasingly concave, thus dishing the specimen and assuring that the thinnest region was at the centre of the disc. Voltage was applied from 0 - 50 V, DC power supplies in series. Current and voltage measurements were recorded; however, the best results were obtained by careful visual inspection for pitting (due to excessive current) or surface dulling (due to film formation). A high intensity microscope light was focussed on the sample with a solid quartz tube which, coupled with a telescope on the opposite side, allowed detection of the first hole on the thin region. The flow was then immediately stopped and the disc thoroughly rinsed in methanol, dried, and placed in an appropriate holder for direct insertion into the microscope.

4.5 Calibration of Phillips EM 300

The use of transmission electron microscopy for the quantitative analysis of lattice defects demands a detailed calibration of the instrument because of the importance of those parameters which are dependent on the excitation current in each lens. The versatility of the Phillips EM 300 stems from its wide choice of lenses - a most useful feature when obtaining images and diffraction patterns. The present calibration is designed to allow the operator to utilize the microscope fully by recording image rotations and magnifications for all the operational modes.

The basic ray diagrams and inversions are illus - trated in Fig. 5 for both images and diffraction patterns which show the excitation of the four magnification lenses. The diffraction lens and the intermediate lens are varied with the magnification selector switch for the different operational modes: M, SA, SC, D+1. The objective lens is varied for focussing and the projector lens is normally operated at maximum excitation. Each magnetic lens adds a magnification multiplication factor accompanied by an image rotation - the amount being a function of the lens current (I). Eyre (1970) recently calibrated an EM 300 and obtained expressions which illustrate this:

$$Rm = 4.4\ I_{D.L.} + 4.8\ I_{I.L.} - 1.75\ I_{O.L.} + 126_{P.L.}$$

for the object to image rotation and

$$Rm = 4.4\ \Delta I_{D.L.} + 4.8\ \Delta I_{I.L.}$$

for the image to diffraction pattern relation. When employing these functions, the diffraction and intermediate lens currents are read on the 0 - 30 scale; the objective lens current is read on the 0 - 100 scale to give ten times the actual lens current in amperes. The following calibration, however, offers greater accuracy and convenience.

The magnifications and image rotations were determined for the goniometer specimen stage at 100 KV at each magnification selector switch position by photographing a ruled replica grating of 54,864 lines per inch, and measuring the line spacings and orientations from the plates (Fig. 6a). All measurements were made at 0^{o} tilt and specimen

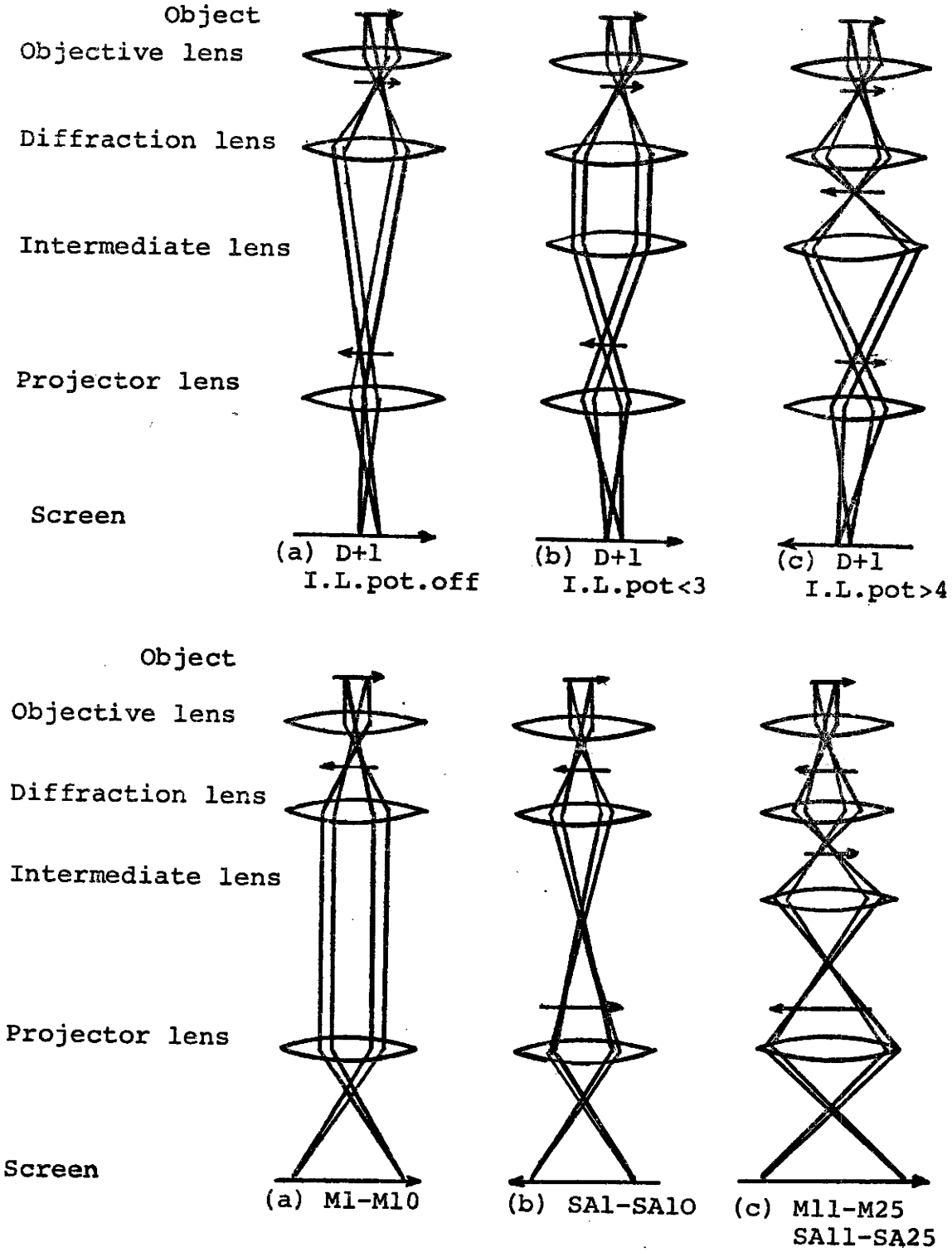

Fig. 5. Schematic representation of the magnification lens geometry of the Phillips EM 300 electron microscope (Eyre, 1970)

(a)

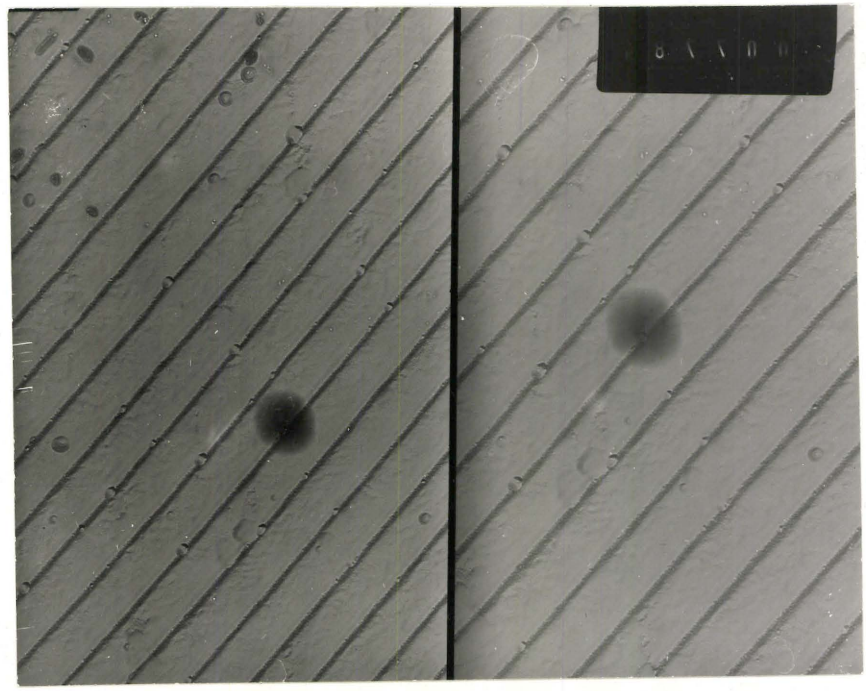

(b)

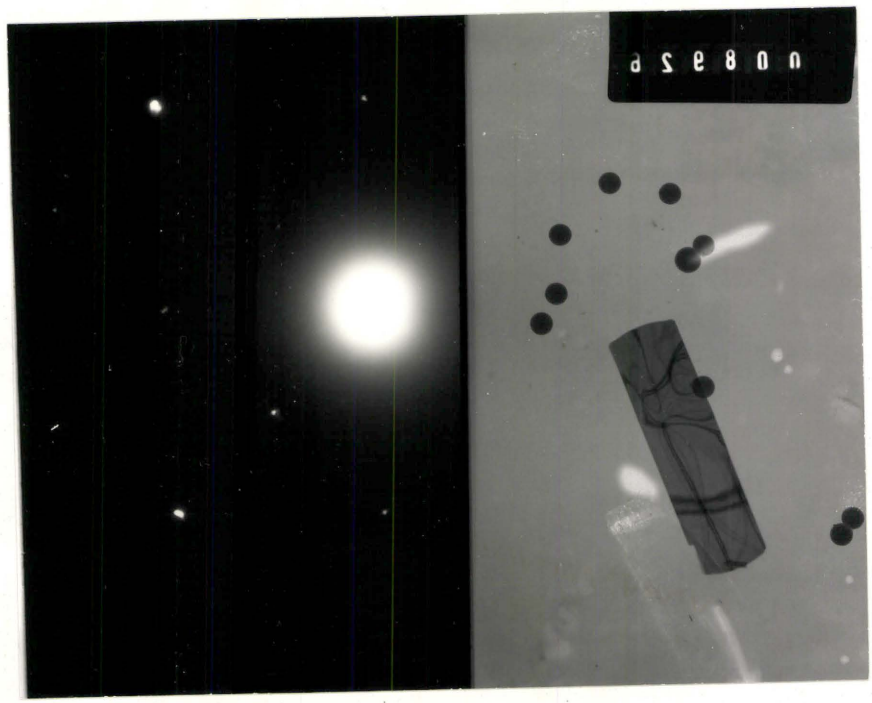

Fig. 6: The magnification and rotation calibration using a) ruled replica grating and b) evaporated MoO_3 crystals with a spray dispersion of polystyrene spheres (0.264 μm) on a Formvar substrate.

height adjusted to accommodate the liquid N_2 cooled anti-contamination device. The relative orientations between the image and the diffraction patterns were found by vapor depositing MoO_3 on a Formvar substrate. Magnifications and rotations were simultaneously checked by spraying a colloidal suspension of polystyrene spheres 0.264μ ±.0060μ diameter onto the substrate (Fig. 6b). The calibration is given in the Appendix.

CHAPTER 5

Results and Discussion: The Interfacial Energies of Stationary γ/β Boundaries

5.1 Introduction

As a result of these experiments, a model for the γ/β interface has been developed; the model is at least qualitatively consistent with all that can be inferred about the energetics of the interface, the temperature dependence of the interfacial energies, and the migrational characteristics of these boundaries.

The atomic structure at the interface between the β and γ phases is considered to have two major components contributing to the excess free energy associated with the boundary. The first, a structural term, arises from the presence of a dislocation network which is accommodating the lattice misfit between the two phases. The network is found, in section 5.2, to consist mainly of partial dislocations of the type $\frac{a}{2}\langle 111\rangle_\beta$. The second component is a chemical term which depends on the strength of the atomic bonds across the interface. At temperatures below the order-disorder transition in the β phase, both crystals possess long range order and the requisite anti-phase bonding contributes a significant component to the interfacial energy

and its anisotropy. Above the order-disorder temperature, the interfacial bonding energy changes very little but the zero state (in the $\beta \rightarrow \beta'$ transition) changes in such a way that the chemical contribution is minimized.

Anisotropies in the structural and chemical terms, primarily due to the orientation dependence of misfit accommodation efficiencies and the orientation dependence of atomic bond densities respectively are reflected in the equilibrium morphologies. In the following sections, these morphologies provide a measure of the magnitude (section 5.4) the orientation dependence (section 5.6), and the temperature dependence of the anisotropy (section 5.7) of the energy associated with the γ/β interphase boundary.

The migration of the γ/β interface, discussed in chapters 6 and 7, involves the compositional and structural rearrangements of the $\beta \rightarrow \gamma$ phase transformation, and is accompanied by the climb of the interface dislocation network. Depending on the origin of the dislocations, they may or may not be forced to trail faults. In circumstances where faults are left behind the interface dislocations, they provide a useful indication as to the detailed mechanism of interface migration.

5.2 Interfacial Dislocation Networks

The structural component of the interfacial free energy was found to consist of a dislocation network necessitated by the difference in lattice parameters of the γ and β phases. By determining the displacements and the geometric configurations associated with the dislocation

arrays, the structural contribution of the interfacial energy can be estimated.

The dislocation structure at the interphase boundary of a dodecahedron shaped γ precipitate equilibrated at 400°C is shown in Fig. 7. The section intersects the four {110} planes as designated and the characteristics of the dislocation network on each faceted interface is tabulated in the accompanying table. The dislocations in the {110} interface planes are oriented along the <112> and <110> directions with respective Burger's vectors of $\frac{a}{2}$<111> and a <001>. The strong [011] two beam reflection condition of Fig. 7 renders one set of $\frac{a}{2}$<111> dislocations invisible; the alternate $\frac{a}{2}$ <111> array and the subsequent interaction product of a <100> segments can readily be observed.

The geometric configuration of the interface dislocation network can be observed directly in Fig. 8 where a {110} γ/β interphase boundary is contained within the plane of the foil. In the first micrograph (a) the $[0\bar{1}\bar{1}]$ operating reflection permits visibility of the $\frac{a}{2}$ $[\bar{1}\bar{1}1]$ and $\frac{a}{2}$ $[\bar{1}1\bar{1}]$ arrays. The second, b) corresponds to a $[\bar{1}01]$ reflection resulting in a strongly diffracting $\frac{a}{2}[\bar{1}00]$ array and a weakly diffracting $a[100]$ array. The complete configuration of the interface dislocation network, given by the superposition of the three arrays, is illustrated schematically in Fig. 9 with the directions of the dislocation lines and their corresponding Burger's vectors for the (011) interphase boundary indicated.

The dislocation networks were observed for the

(a)

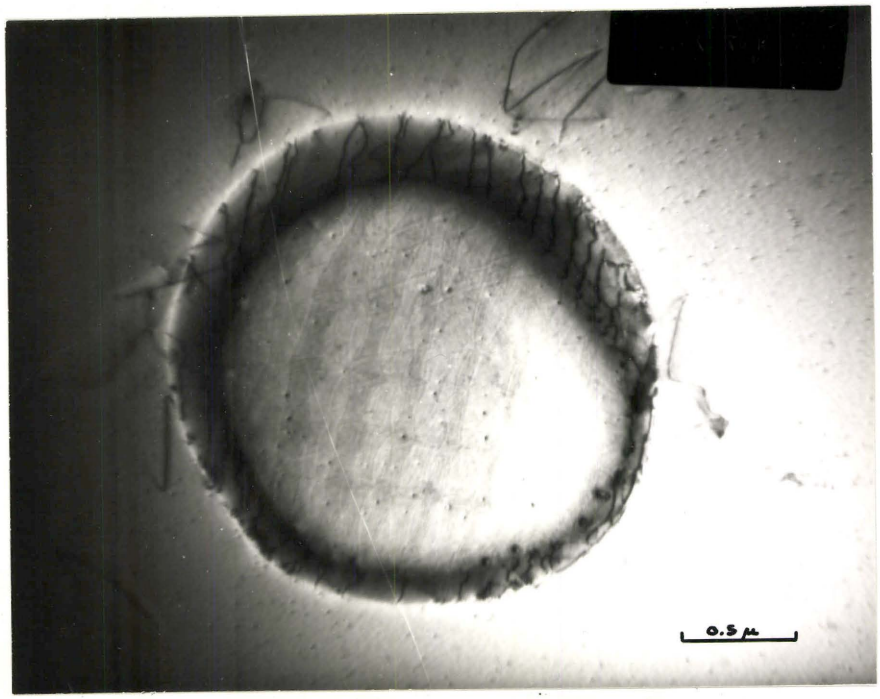

(b)

{110} Plane	Dislocations visible <111> type u	<111> type b	<100> type u	<100> type b	Invisible <111> type u	<111> type b
101	$[\bar{1}21]$	$\frac{a}{2}[11\bar{1}]$	$[\bar{1}01]$	$a[010]$	$[12\bar{1}]$	$\frac{a}{2}[\bar{1}11]$
110	$[\bar{1}12]$	$\frac{a}{2}[1\bar{1}1]$	$[1\bar{1}0]$	$a[001]$	$[1\bar{1}2]$	$\frac{a}{2}[\bar{1}11]$
$10\bar{1}$	$[121]$	$\frac{a}{2}[1\bar{1}1]$	$[101]$	$a[010]$	$[1\bar{2}1]$	$\frac{a}{2}[111]$
$1\bar{1}0$	$[112]$	$\frac{a}{2}[11\bar{1}]$	$[110]$	$a[001]$	$[11\bar{2}]$	$\frac{a}{2}[111]$

Fig. 7: A transmission electron micrograph of a (100) section of a γ precipitate showing a) the misfit dislocation at the interphase boundary and b) the contrast behavior for the $[01\bar{1}]$ operating reflection.

(a)

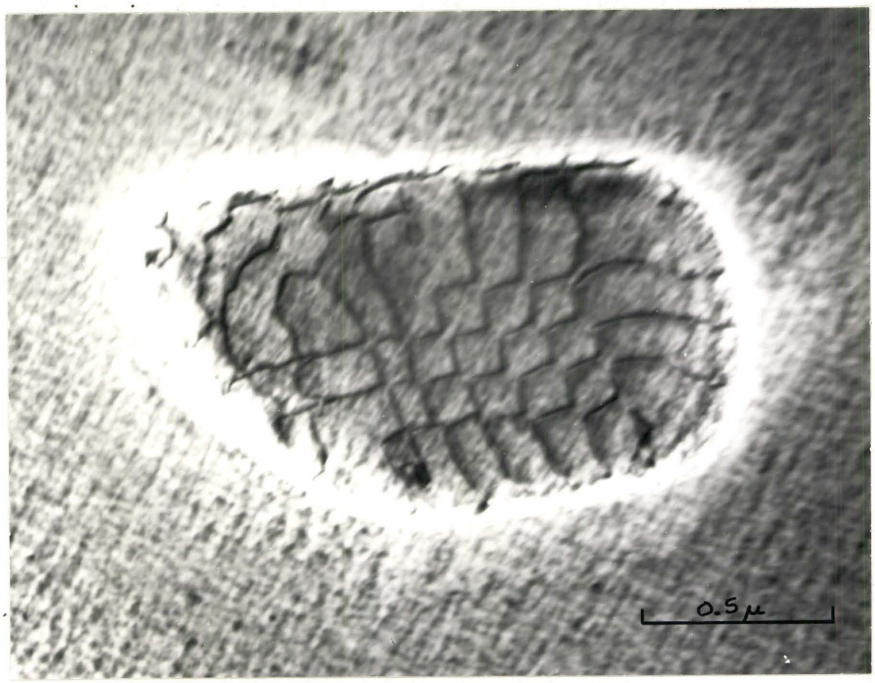

(b)

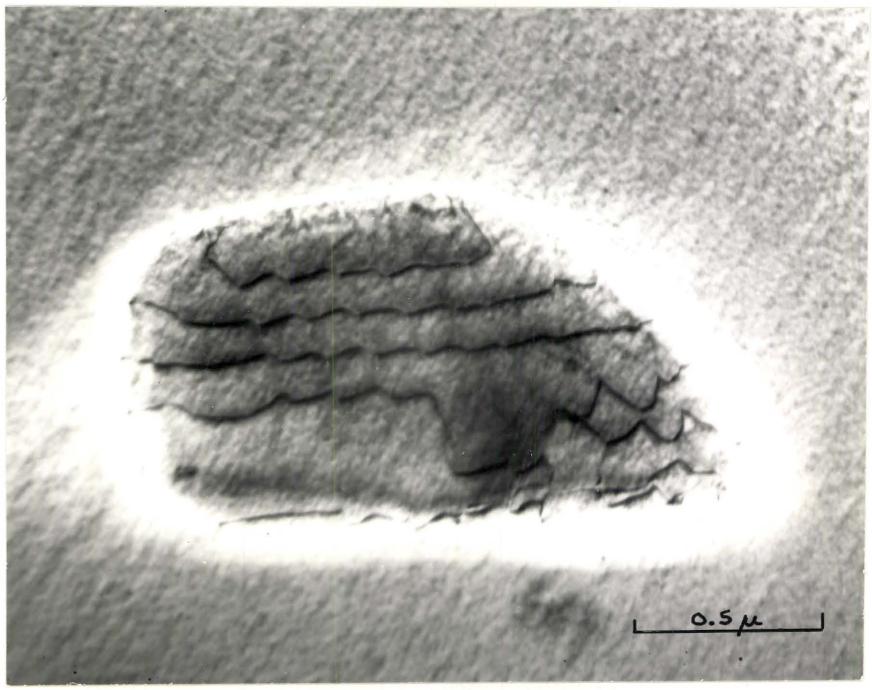

Fig. 8: The misfit dislocations observed by transmission electron microscopy on a (011) interphase boundary contained within the plane of the foil for a) $[01\bar{1}]$ and b) $[\bar{1}01]$ two beam conditions.

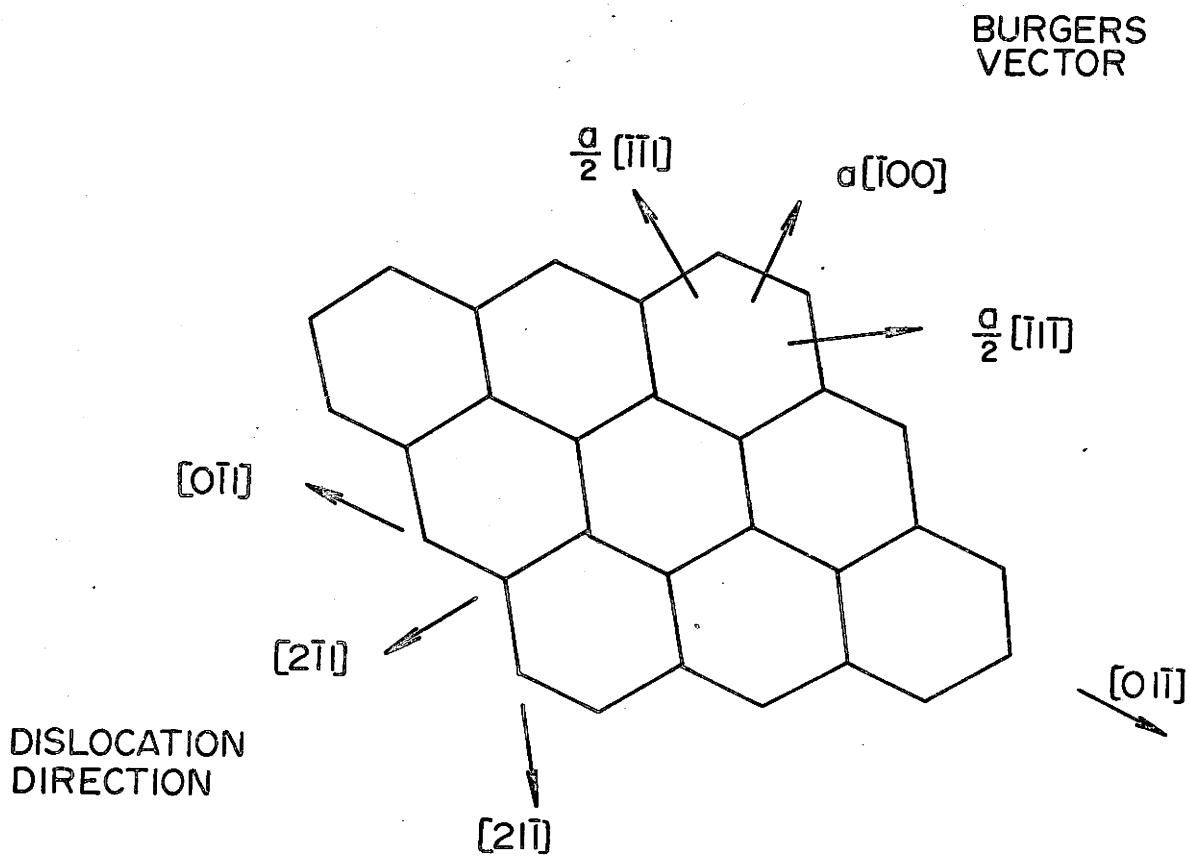

Fig. 9: Schematic representation of dislocation configuration on a (011) faceted boundary of a γ polyhedra precipitate determined by superimposing Fig. 8(a) and (b)

complete γ/β interphase boundaries bounding the precipitates. In Fig. 10, the [112] foil normal allows access to all the low index orientations by using the goniometer stage in the electron microscope. For example, when coupled with the appropriate specimen rotation, a $\pm 45^{o}$ tilt yields the (101) and (011) planes normal to the electron beam and allows the dislocations to be observed on the left and right interphase boundaries respectively. Similarly, the (001) and (111) orientations show the top and bottom precipitate interfaces.

Each characteristic diffraction pattern of planes normal to the electron beam allows certain possible reflections with the two-beam condition obtained by minute specimen tilts or rotations. The corresponding observed dislocation contrast is shown in Table 4. The γ precipitate was equilibrated at $500^{o}C$ and therefore exhibited a relatively isotropic morphology. The {110} cusp orientations are designated in Fig. 10, and the dislocations on these boundary planes will be either visible (V) or invisible (O), depending on the diffracting conditions. The results tabulated are consistent with the dislocation contrast model for elastically anisotropic crystals of Head, Loretto and Humble (1967) who found the usual isotropic invisibility criteria ($g.b = 0$ and $g.b \times \mu = 0$) were valid only for pure edge and pure screw dislocations lying perpendicular to a symmetry plane of the crystal. The observation of normal contrast behavior of the γ/β interfacial dislocations on {110} planes confirm the pure edge character and allow determination of the Burger's vector.

[001]

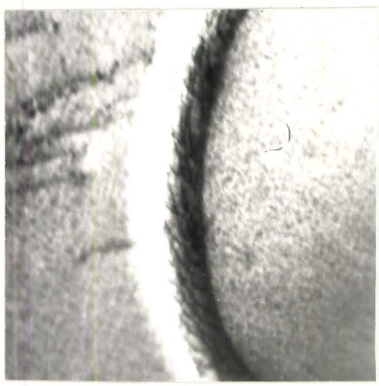

[101]

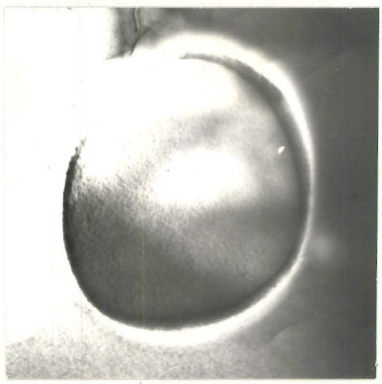

[112]

[011]

[111]

Fig. 10: Transmission electron micrographs of interfacial dislocations continuously encompassing a γ precipitate observed at the orientations shown by appropriate rotations with the goniometer stage.

TABLE 4

Micrograph Number	Plane normal to electron Beam	Operating Reflection	Dislocations on Plane (101) b=[$\bar{1}11$]	(101) b=[$11\bar{1}$]	(011) b=[$11\bar{1}$]	(011) b=[$1\bar{1}1$]	(110) b=[$1\bar{1}1$]	(110) b=[$\bar{1}11$]
8729	112	$1\bar{1}0$	v	o				
8733	112	$\bar{1}10$	v	o	o	v	v	v
8737	112	$1\bar{1}0$	v	o			v	v
8739	212	$10\bar{1}$			v	o	o	v
8741	212	$\bar{1}01$	v	v			o	v
8747	513	$\bar{1}\bar{1}2$	v	v				
8749	513	$11\bar{2}$	v	v				
8752	112	$1\bar{1}0$	v	o	o	v		
8756	112	$\bar{1}10$	v	o	o	v		
8759	112	$1\bar{1}0$	v	o			v	v
8762	111	$0\bar{1}1$			v	v	v	o
8765	111	$\bar{1}01$			v	o	o	v
8770	221	$0\bar{1}2$		v	v	v		
8774	113	$21\bar{1}$		v	v			
8778	001	$\bar{1}\bar{1}0$	o	v	v	o		
8782	001	$1\bar{1}0$	o	v	v	o		
8784	112	$\bar{1}10$	v	o			v	v
8787	112	110	v	o	o		v	v
8791	101	$10\bar{1}$	v					
8793	101	$\bar{1}01$	v	v			o	v
8796	011	$2\bar{1}1$			v	v	v	o

The observations of similar dislocation contrast for varying interface orientations suggests no complex reactions occur among dislocations as the interface orientation is varied from {110}. The dislocations remain predominantly <111> types at the corners of the faceted γ polyhedra. Fig. 11 illustrates a <111> corner observed with various <110> reflections. The specimen has been equilibrated at 350°C (100 hr.) to obtain a smoothly rounded corner and subsequently upquenched to 400°C (30 min.) causing growth of adjacent facets and effectively pinning the corner. This results in an increased possibility of dislocation reactions. The boundary shown contains three sets of dislocations: $[11\bar{1}]$, $[1\bar{1}1]$ and $[\bar{1}11]$. The visibility of each set in the regions marked I, II and III of Fig. 11 are tabulated below (Table 5).

The absence of complex dislocation interactions permits the interface dislocation network to be described by major <111> grids encompassing the precipitate . The spacing of the dislocations to completely relieve the misfit is:

$$m = \frac{b}{\delta} \tag{5.1}$$

where b is the component of the Burger's vector in the edge orientation in the boundary plane

and the misfit, δ, is

$$\delta = \frac{a_1 - a_2}{\frac{1}{2}(a_1 + a_2)} \tag{5.2}$$

where a_1 and a_2 are the lattice parameters which have been determined by Robertson (1968) for the γ/β phase boundary composition: a_γ = (2.95375 x 3) A and a_β = 2.9445 A.

The expected interdislocation spacing of $\frac{a}{2}$<111>

a)

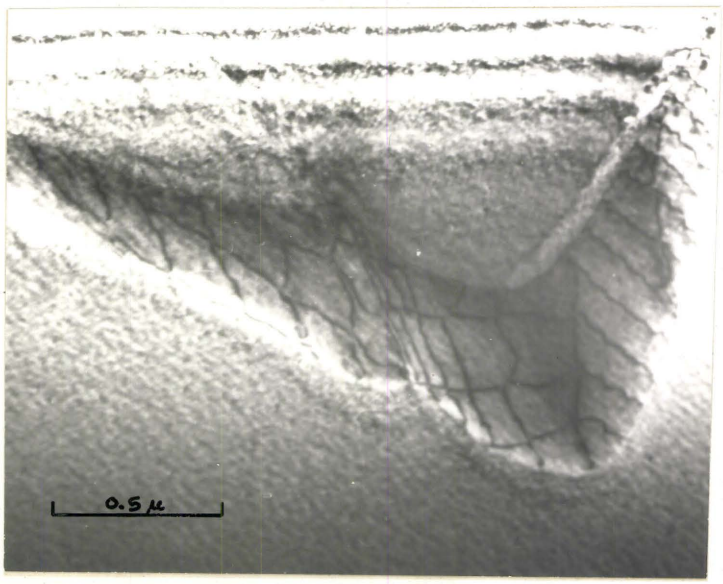

b)

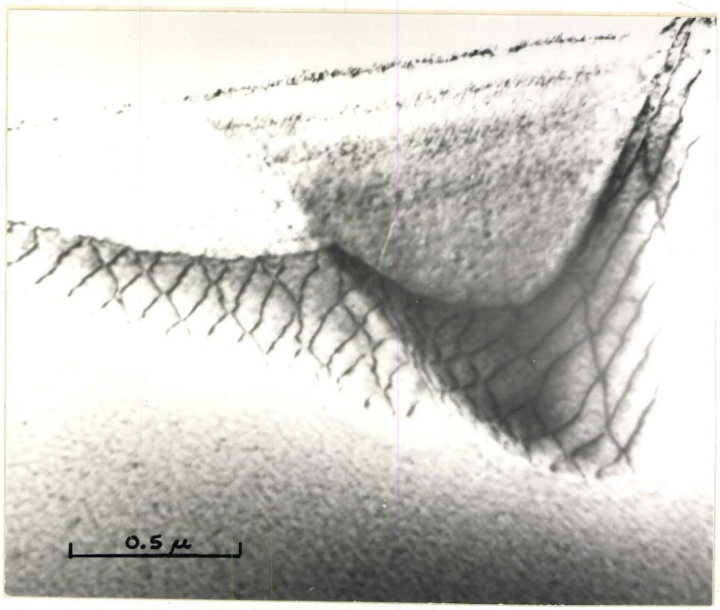

Fig. 11: Transmission electron micrographs of interfacial dislocation networks at a <111> corner after an equilibration treatment at 350°C and a growth treatment at 400°C, observed with a) $[0\bar{1}1]$, b) $[\bar{1}01]$

TABLE 5: Dislocations observed at a complex <111> corner illustrated in Fig. 11

	g	I	II	III
a)	$0\bar{1}1$	$11\bar{1}$	$11\bar{1}$	$1\bar{1}1$
		$1\bar{1}1$	$1\bar{1}1$	
b)	$\bar{1}01$	$\bar{1}11$	$11\bar{1}$	$\bar{1}11$
		$11\bar{1}$	$\bar{1}11$	
c)	$1\bar{1}0$	$\bar{1}11$	-	$\bar{1}11$
		$1\bar{1}1$		$1\bar{1}1$

parallel arrays on a {110} interface plane resulting from the difference in lattice parameters is about 800A. The observed spacing of about 1200 A is in reasonable accord with the predicted values measured under similar conditions (i.e. specimens which are equilibrated in the $\beta+\gamma$ phase field, quenched, and subsequently observed at room temperature). The difference in thermal expansion coefficients of the two phases tends to increase the density of dislocations with temperature.

Van der Merwe (1963) has calculated the structural component of the energy as a function of misfit and found the minimum energy interface at small misfits ($\delta < 0.1$ per cent) was associated with a constrained coherent boundary having the misfit stored elastically in the lattices. At larger misfits, an unconstrained dislocation interface provided the lowest energy.

The misfit between the β and γ lattices is 0.3 per cent; the observations are therefore consistent with an interface dislocation network completely compensating the lattice disregistry. The γ precipitates can be assumed to be essentially free of long range stresses and will be unimpeded from attaining an equilibrium morphology consistent with minimizing the chemical (due to "wrong" atomic bonds across the interface) and the structural (due to the misfit dislocation network at the interface) components of the interfacial energy.

5.3 Theoretical Estimate of the γ/β Interfacial Energy

The structural and chemical components of the energy of the γ/β interphase boundary are considered to be independent. The structural contribution arises from the interface dislocation network accommodating the lattice misfit and is estimated simply as:

$$\frac{\text{energy}}{\text{area}} = \left(\frac{\text{energy}}{\text{unit disl. length}}\right)\left(\frac{\text{length}}{\text{area}}\right)$$

The energy associated with the observed dislocation grid at the boundary is evaluated. Variations in the density of dislocations required to relieve misfit with interface orientation are shown to contribute to the expected anisotropy of the structural interfacial energy.

The principal chemical contribution is due to the difference in near neighbour atomic interactions at the interface. The enthalpy of the boundary

$$\frac{\text{energy}}{\text{area}} = \left(\frac{\text{atoms}}{\text{area}}\right)\left(\frac{\text{bonds}}{\text{atom}}\right)\left(\frac{\text{energy}}{\text{bond}}\right)$$

is estimated by the juxtaposition of the two crystal lattices. The anisotropy of the chemical component is estimated from the variation in bond densities with interface orientation.

The sum of the two components provides an estimate of the energy of the partially coherent boundary separating the β and γ phases. The specific dislocation energies and excess bond energies are now considered.

The energy associated with a misfit compensating dislocation array between two lattices of parameters a_1 and a_2

in an isotropic media is given by(Van der Maue, 1964):

$$E = \frac{\mu c}{4\pi^2}\{1 + \beta - (1+\beta^2)^{\frac{1}{2}} - \beta \ln|2\beta(1+\beta^2)^{\frac{1}{2}} - 2\beta^2|\} \qquad (5.3)$$

where $c = \frac{1}{2}(a_1 + a_2)$

$$\beta = 2\pi\delta(\frac{\Omega}{\mu}) \qquad (5.4)$$

$$\frac{1}{\Omega} = \frac{(1+\sigma_\alpha)}{\mu_\alpha} + \frac{(1+\sigma_\beta)}{\mu_\beta} \qquad (5.5)$$

and: μ, μ_α, μ_β are the shear moduli for the boundary α, and β respectively

σ_α, σ_β are the Poisson ratios within the two phases.

Setting $\sigma_\alpha = \sigma_\beta = 1/3$ and $\mu_\alpha = \mu_\beta = \mu$, E becomes a function of μ and δ only. For an $\frac{a}{2}$<111> grid (of spacing 1200A) on a (110) planar interface, the calculated energy is 60 ERGS/cm^2.

A better estimate is possible by considering the effect of anisotropic elasticity. The total energy per unit length of an edge dislocation having Burgers vector $\underline{b} = (b_1, b_2, b_3)$ referred to axes lying in the interface and normal to it can be written (Head 1964):

$$\xi = \varepsilon^o\left[\frac{K_{11} + (b_1^2+b_2^2) + K_{33}(b_3^2)}{4\pi}\right]\ln\frac{R}{ro} \qquad (5.6)$$

where the inelastic core energy ε^o is usually taken as $C_{44}\, a^2/_{10}$ on the assumption that the core stresses approach the theoretical shear strength $C_{44}/_{30}$. R and ro represent the outer and inner cut off radii and are taken equal to

the interdislocation spacing and 5a respectively. Analytic expressions exist for the specific orientations desired, that is, for edge dislocations in the (010) and (110) planes. Foreman(1965) reported:

$$K_{11} = (C_{11}+C_{12}) \left[\frac{C_{44}(C_{11}-C_{12})}{C_{11}(C_{11}+C_{12}+2C_{44})}\right]^{\frac{1}{2}} \qquad (5.7)$$

for an edge dislocation a[010] lying along [100] in the (001) plane. Head (1964) determined the analytic expression for an edge dislocation lying in the (110) plane along a [111] direction:

$$K_{11} = \tfrac{1}{2} \left[\frac{S_{11}}{S_{44}} (S_{11}S_{44} - S_{15}^2)\right]^{-\frac{1}{2}} \qquad (5.8)$$

where S_{ij} are functions of the elastic stiffness coefficients.

By assuming similar elastic constants for both γ and β phases, the total energy per unit length of interfacial dislocation was estimated to be 1.54×10^{-4} ergs/cm for a $\langle 010 \rangle$ dislocations on the {001} plane and 1.34×10^{-4} ergs/cm for $\frac{a}{2}\langle 111 \rangle$ dislocations on the {110} plane. The total structural contribution to the interphase boundary energy depends on the dislocation density required to relieve misfit. Substituting the observed spacings of 1200Å for a dislocation of Burgers vector $\frac{a}{2}[111]$ and 1400Å for a dislocation of Burgers vector a[010] results in equivalent total energies of 32.5 ergs/cm^2. It is not possible, however, to produce all the a<100> Burgers vectors necessary

for a <100> grid on {100} planes by simple dislocation reactions among $\frac{a}{2}$<111> types, consequently, it was concluded that for the purpose of estimating the structural component of the interfacial energy, one needs only to consider the major $\frac{a}{2}$<111> grids lying in {112} planes.

Similar prismatic dislocation loops on {111} planes, observed by Cupschalk and Brown (1967) in quenched β brass, were found to be circular. It is assumed, for simplicity, that the equilibrium shape of the $\frac{a}{2}$<111> interface dislocation loops on the {112} planes are also circular, and that the interface dislocation density can change locally in accord with variations in misfit accommodation efficiency. This efficiency is determined by the orientation of the interface relative to the four possible Burger's vectors of the type $\frac{a}{2}$<111> which can relieve the dilational transformation strain in this system.

The model for the interface, illustrated in Fig. 12, consists of four types of loops with Burgers vectors of $\frac{a}{2}$<111>, $\frac{a}{2}$<1$\bar{1}$1>, $\frac{a}{2}$<11$\bar{1}$>, and $\frac{a}{2}$<$\bar{1}$11> encircling the nearly spherical precipitates. The locus of maximum misfit accommodation efficiency can be represented by the trace of a <111> plane. Points on this trace exhibit the maximum relief of lattice misfit and consequently the lowest density of necessary dislocations in one direction. The {110} poles are at trace intersections and thus correspond to maximum relief in two directions, or a minimum energy configuration.

The anisotropy of the structural component can be calculated by assuming that as the component of the Burgers

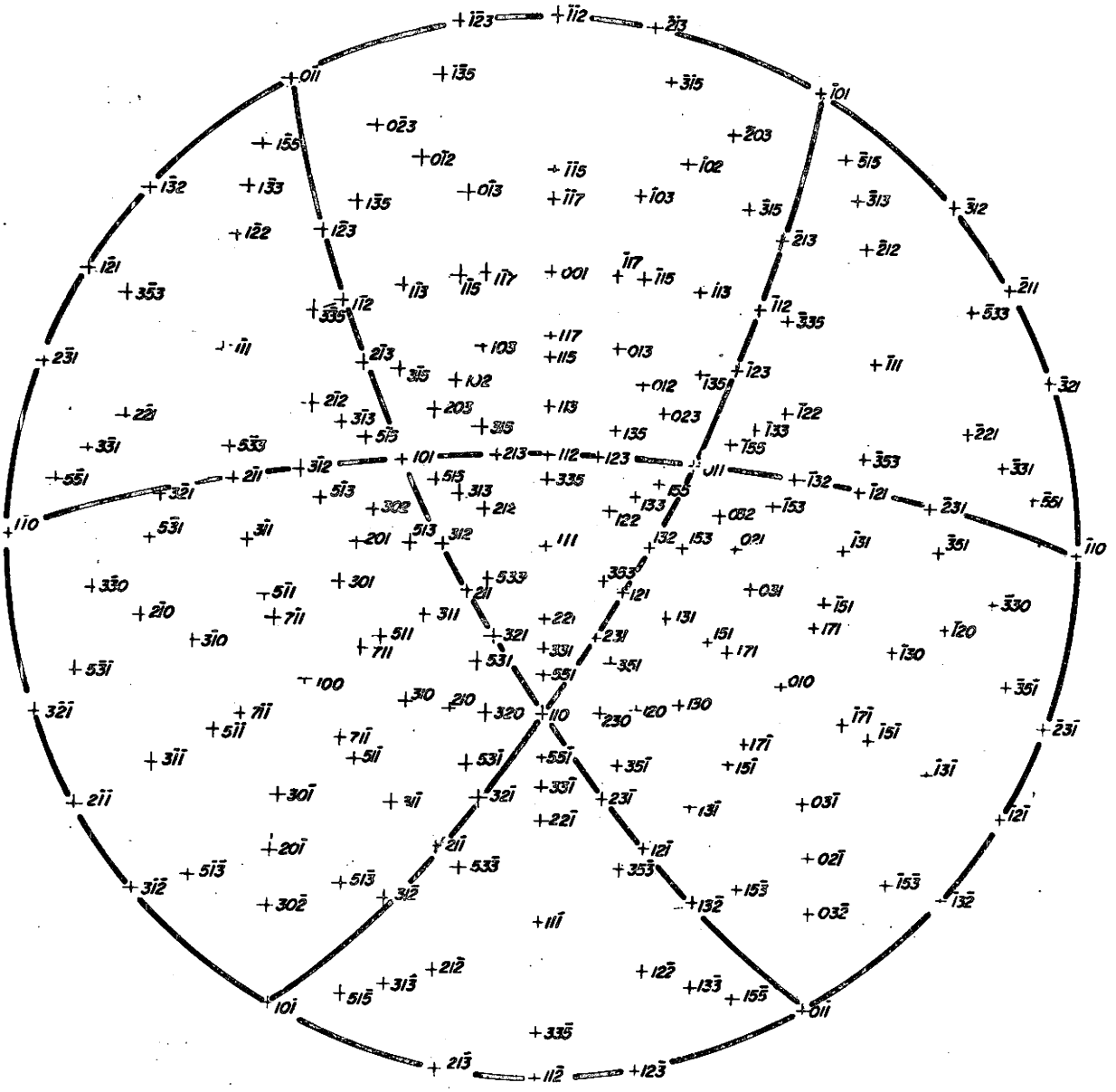

(111) Standard projection of the cubic system

Fig. 12: The interfacial dislocation arrays consist of four b = $\frac{a}{2}$<111> loops.

The trace of the extra half plane of atoms is shown stereographically for b completely in the boundary plane.

vector in the interface decreases, the density of the dislocations must increase in a corresponding manner. Thus referring to Fig. 12, we have:

$$\frac{\gamma_{111}}{\gamma_{110}} = \frac{1}{\cos 19^{o},} \quad \text{and} \quad \frac{\gamma_{100}}{\gamma_{110}} = \frac{1}{\cos 35^{o}}$$

In terms of the calculated grid energies, (γ_{110} = 32 ergs/cm^2) one finds γ_{111} is ergs/cm^2 and γ_{100} is 39 ergs/cm^2.

The chemical component of the interfacial energy is the excess energy, ΔG^s, attributed to the surface due to contributions from enthalpic, ΔH^s, and entropic, ΔS^s, terms:

$$\Delta G^s = \Delta H^s - T\Delta S^s \qquad (5.9)$$

The excess entropy of a surface derives from both a vibrational contribution and a configurational contribution. The vibrational contribution is usually estimated by considering the atoms in the grain boundary zone as a system of simple harmonic oscillators with extra degrees of freedom. The frequency and amplitude of vibration will depend on the atomic volume which is a function of the structural disorganization of the boundary. Hondros (1968) has estimated the vibrational contribution of a boundary having one-third of the sites vacant as 0.09 erg cm^{-2} ^{o}K^{-1}. The present nearly coherent boundary should therefore have a negligible vibrational contribution.

The configurational entropy of a surface is a function of the number of distinguishable ways in which the different bonds can be arranged across an interphase boundary. This component is zero for an interface separating completely ordered or completely random solutions because the juxtaposition of

the solid solutions produces an interphase boundary at which the randomness of the bond arrangements is exactly the average of crystallographically identical boundaries within the two component phases. A random/ordered α/θ' boundary in Cu-Al was found (Aaronson, Clark, Laird, 1968) to have an excess configurational entropy contribution ($T\Delta S$), of 1.45 ergs/cm^2 at 300°C. The entropic components, both vibrational and configurational, of the chemical interfacial energy in solid/solid systems are small and can normally be neglected.

The major contribution to the chemical interfacial energy is due to the enthalpic component, ΔH^s, which arises from the excess energy of the bonds across the interface, $H_{\gamma\beta}$, when compared with crystallographically equivalent boundaries in the adjacent lattices (i.e. $H_{\beta\beta}$ and $H_{\gamma\gamma}$ for the respective β and γ phases):

$$\Delta H^s = H_{\gamma\beta} - \tfrac{1}{2}(H_{\beta\beta} + H_{\gamma\gamma}) \tag{5.10}$$

where

$$H_{\gamma\beta} = n^s_{AB}V_{AB} + n^s_{AA}V_{AA} + n^s_{BB}V_{BB} \tag{5.11}$$

$$H_{\beta\beta} = n^\beta_{AB}V_{AB} + n^\beta_{AA}V_{AA} + n^\beta_{BB}V_{BB} \tag{5.12}$$

$$H_{\gamma\gamma} = n^\gamma_{AB}V_{AB} + n^\gamma_{AA}V_{AA} + n^\gamma_{BB}V_{BB} \tag{5.13}$$

where n is the bond density; the subscript refers to the type of near neighbour interactions and the superscript refers to the position of the plane cutting the atomic bonds. V is the energy of the designated bond.

The excess bond energy of a boundary separating two solid phases is a result of a variation in near neighbour interactions. The difference in bond energies arising from a

compositional discontinuity at an interface separating random solid solutions of identical orientation, structures and lattice parameter has been calculated by Servi and Turnbull (1966). This was extended, by Aaronson, Clark and Laird (1968), to a fully coherent α/θ' boundary separating a random and an ordered solid solution of Cu-Al.

In the present case, both the β' and the γ phases possess long range order, thus the positioning of individual atoms on each crystal lattice tends to have a greater effect on the near neighbour interactions than changes induced in bonding by the compositional difference between the two phases. An analogous effect occurs with the formation of an antiphase boundary in an ordered crystal where complete wrong bonding may result. Similarly, partial wrong or antiphase bonding may occur at an interphase boundary separating ordered phases. By postulating the atomic structure at the boundary, an estimate of the enthalpic contribution of the interfacial energy due to the excess bond energy is possible.

The atomic structure of the coherent γ/β interface is estimated by the cutting and juxtaposition of the β and γ lattices. The β phase has a body centered cubic lattice with the body centered and corner sites a) having exclusively copper or zinc atoms in the lower temperature ordered β' regime, and b) having a random distribution of copper and zinc atoms in the higher temperature disordered β regime. The more complex γ lattice can be derived directly from the β lattice by considering a body centered cube of vacancies formed from

a 3x3x3 array of β cells. However the atomic distribution of atoms on the γ lattice sites does not follow directly from the ordered β' structure. By comparing the atomic distribution of the β CsCl type structure and the γ structure shown in fig. 1, it is seen that half the tetrahedral sites contain differing atoms (i.e. if one removes a copper atom from a CsCl lattice all the tetrahedral sites are zinc; in the γ lattice the inner tetrahedral sites are zinc and the outer tetrahedral sites are copper) and half the octahedral sites contain differing atoms (i.e. for a similar copper atom removed, all the octahedral sites would be copper atoms in the ordered CsCl lattice while in the γ lattice, half the octahedral sites are copper and half (denoted cubo-octahedral) are zinc). It becomes apparent that the γ/β' boundary contains about half wrong or antiphase bonded atoms when compared with the ordered β lattice which exhibits complete in phase atomic bonding (i.e. unlike nearest neighbours).

The magnitude of the excess enthalpic component was estimated from the energies of the appropriate nearest neighbour interactions. V_{cu-cu} and V_{zn-zn} are estimated conventionally as the negative of one-sixth the heat of sublimation of the pure metals. V_{cu-zn} is manifested as the tendency towards ordering and is related to the ordering temperature, T_c, through the Bragg-Williams relation (Swalin, 1967):

$$\frac{kT_c}{4} = V_{AB} - \tfrac{1}{2}(V_{AA} + V_{BB}) \qquad (5.14)$$

giving: $V_{Cu-Cu} = 8.8 \times 10^{-13}$ ergs/bond

$V_{Zn-Zn} = 3.5 \times 10^{-13}$ ergs/bond

$V_{Cu-Zn} = 6.4 \times 10^{-13}$ ergs/bond

The individual bond densities of an idealized boundary based on a simplified γ brass structure* were determined on (100) and (110) planes. This allowed an estimate of the bond energies, $H_{\gamma\beta}$, $H_{\beta\beta}$ and $H_{\gamma\gamma}$, (eqns. 5.11 to 5.13 respectively) and excess surface energy, ΔH^s (eqn. 5.10) as shown in Table 6. The complicated atomic distribution of the γ brass structure results in a variation of 2-3% in the bond potential with interface position. The disconcerting oscillation of the excess interfacial enthalpy with position is probably a result of inadequacies in the model; in particular, of the assumption that the γ and β lattices are structurally similar except for the vacant sites in γ. It seems reasonable, however, to accept the qualitative inference that $H_{\gamma\beta}$ is essentially unchanged when disordered β is ordered, while rejecting the detailed variation with position shown in Table 6. Some variation of this kind probably exists and leads to minimum energy positions for the planar interface. A similar result was encountered by Aaronson, Clark and Laird (1968) and avoided by assuming a modified atomic structure. Having accepted the limitations of this type of a calculation in this system, it is of interest to note a) that the excess

*The structure is formed from a b.c.c. array by removing corner and center atoms from a 3x3x3 stack of b.c.c. cells and properly arranging the copper and zinc atoms on these sites (such that the γ structure would be formed by the collapse of atoms into the vacant sites.

TABLE 6: Average Bond Energies of (100) and (110) sections ($\times 10^{-13}$ ergs/bond) where $n = n_{AA} + n_{BB} + n_{AB}$

Enthalpy	Section	β' (Ordered) (100)	β' (Ordered) (110)	β (Random) (100)	β (Random) (110)
$H_{\gamma\beta}/n$	0 - 1/6	-5.6323	-5.5956	-5.7261	-5.5956
	1/6-1/3	-5.8567	-5.8567	-5.8567	-5.8567
	1/3-1/2	-5.8201	-5.8567	-5.7261	-5.8567
		-5.7697	-5.7697	-5.7697	-5.7697
$H_{\gamma\gamma}/n$	0 - 1/6	-5.1711	-5.1434	-5.1711	-5.1434
	1/6-1/3	-5.4044	-5.4600	-5.4044	-5.4600
	1/3-1/2	-5.1711	-5.1434	-5.1711	-5.1434
		-5.2489	-5.2489	-5.2489	-5.2489
$H_{\beta\beta}/n$	0 - 1/6	-6.4200	-6.4200	-6.2950	-6.2950
	1/6-1/3	-6.4200	-6.4200	-6.2950	-6.2950
	1/3-1/2	-6.4200	-6.4200	-6.2950	-6.2950
		-6.4200	-6.4200	-6.2950	-6.2950
$\Delta H^s/n$	0 - 1/6	+0.1633	+0.1861	+0.0070	+0.1236
	1/6-1/3	+0.0555	+0.0833	-0.0070	+0.0208
	1/3-1/2	-0.0245	-0.0750	+0.0070	-0.1375
		+0.0648	+0.0648	+0.0024	+0.0024

energy of the surface is due to the difference in standard states of the disordered β and ordered β' phases. The average magnitude of the excess energy (0.0648×10^{-13} ergs/bond) is one quarter of the A.P.B. energy ($\frac{kT_c}{4} = 0.256 \times 10^{-13} \frac{\text{ergs}}{\text{bond}}$) b) The excess energy of the disordered γ/β boundary is an order of magnitude less than the ordered γ/β' boundary. The difference in excess energy is expected to be proportional to the long range order parameter s (Swalin, 1967):

$$n \frac{(1 + s)}{(1 - s)} = \frac{2 T_c s}{T} \qquad (5.15)$$

Thus, at any temperature, T, less than the order-disorder

transition in the β phase, T_c, the magnitude of the chemical term can be estimated.

c) The net energy per bond, H/n, is similar for (100) and (110) planes; this implies the factor determining the anisotropy of the total chemical energy is the density of bonds being cut by an interface plane, (hkl). Considering the ordered β lattice as representative of the bond directions, the orientation dependence of the energy can be written (Cupschalk and Brown, 1967):

$$\Delta H^{chem} = \frac{-4h}{a_o^2\sqrt{h^2 + h^2 + l^2}} \frac{\Delta H^s}{n} \text{ for } h > (k+1) \quad (5.16)$$

and

$$\Delta H^{chem} = \frac{-2(h + k + l)}{a_o^2\sqrt{h^2 + k^2 + l^2}} \frac{\Delta H^s}{n} \text{ for } h < (k+1) \quad (5.17)$$

Taking $a = 2.95 \times 10^{-8}$ cm and $\frac{\Delta H^s}{n} = 0.0648 \times 10^{-14}$ ergs/bond one arrives at the value of $\Delta H^{chem}_{\gamma\beta'} = 20$ ergs/cm^2 for {110} and 28 ergs/cm^2 for {100}.

The complete orientation dependence of ΔH^{chem} and the resulting coherent precipitate shape are shown in Fig. 13 for calculations based on nearest neighbour interactions (Mackenzie, Moore and Nicholas, 1962).

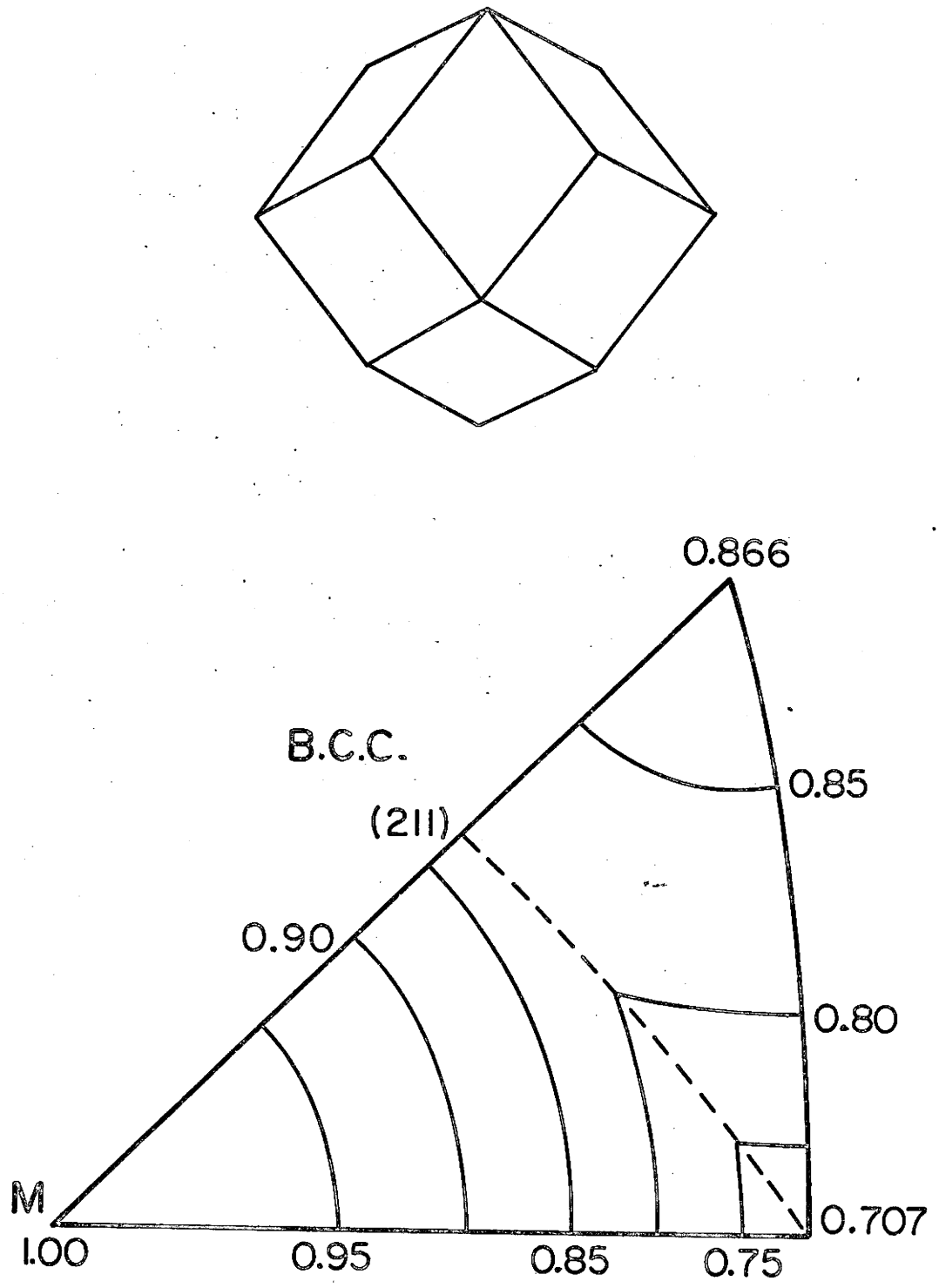

Fig. 13. Relative interfacial energies for nearest neighbour pairwise interaction model and resulting equilibrium shape. (for body centered cubic lattice (MacKenzie Moore and Nicholas).

Calculations of the theoretically expected values of both the structural and chemical contributions of the interfacial energy is given in Table 7. The structural contribution due to the misfit compensating dislocation grid is calculated using the observed configurations and considering anisotropic elasticity in the β matrix. The chemical contribution arises from the excess atomic bonding at the interface. The model, based on a B.C.C. vacancy γ structure of correct atomic positions, allows the magnitude, the temperature and the orientation dependence of the chemical term to be estimated.

5.4 Magnitude of the γ/β Interphase Energy

The geometric description of a grain or interphase boundary must include both misorientation parameters to relate the orientations of the crystal lattices on either side of the boundary, and boundary position parameters to define the orientation of the interface. Most measurements of relative interfacial energies are based on boundary geometry effects (either at a junction, or of isolated particle shape) and therefore allow the analysis to include the effects of both crystal and interface orientation. The controlled variation of these orientation parameters is not possible in most systems and analysis usually involves correlating a large number of individual observations.

Dihedral angle measurements between interfaces at equilibrated junctions, which separate regions of differing crystal and interface orientation, yield relative surface energies from a triangle of forces relationship (Smith, 1948) modified for surface torques (Herring, 1951).

TABLE 7: γ/β Interfacial energies (ergs/cm^2) based on a theoretical model of the structure of the interphase boundary

Temperature (°C)	Chemical Component (110)	(100)	Structural Component (110)	(100)	Total Interfacial Energy (110)	(100)	$\frac{\gamma(100)}{\gamma(110)}$
300	15	21	32	39	47	60	1.28
350	13	18	32	39	45	57	1.27
400	10	14	32	39	42	53	1.26
500	0.6	1.0	32	39	33	40	1.21

This technique is used primarily to calculate surface energies as a function of lattice misorientation across the interface, thus describing the major factor contributing to energies of internal surfaces.

If the lattice misorientation parameters can be held constant, the application of Wulff's Theorem to isolated equilibrated shapes will yield the relative surface energy as a function of interface orientation. This condition is met in the present study by using γ precipitates equivalently oriented with the β matrix in the copper-zinc alloy system.

The orientation equivalence between the β matrix and the γ precipitates for grain boundary allotriomorphs and intragranular idiomorphs allow both the dihedral angle technique and the equilibrium shape technique to be used in determining the energies associated with the coherent γ/β interphase boundary. The low energy interface of the grain boundary precipitate is similar to the interface encompassing the intragranular precipitate, and the experimental techniques are compatible.

Measurement of dihedral angles at grain-precipitate boundary junctions allowed an independent estimate of the magnitude of the α/β and γ/β interphase energies as surface or interface nodes will tend to adjust themselves into the lowest energy configuration. In the absence of torque terms, the interfacial energy is numerically equal to the interfacial tension, σ, and at equilibrium:

$$\frac{\sigma_1}{\sin \theta_1} = \frac{\sigma_2}{\sin \theta_2} = \frac{\sigma_3}{\sin \theta_3}$$

where σ_1, σ_2, σ_3 are tensions of boundaries 1, 2 and 3,

separated by angles θ_1, θ_2 and θ_3 (Fig. 14 a)).

The equilibrium geometry was attained for the α and γ grain boundary allotriomorphs by a one week isothermal aging treatment at 520°C, a temperature giving sufficient atomic diffusion and, in the case of γ, relatively isotropic surface energies (as determined in section 5.6).

The results are plotted in Fig. 14, yielding average dihedral angles of 80°: 140°: 140° for $\theta_1:\theta_2:\theta_3$ respectively for the α allotriomorphs, and 99° : 170° : 91° for the γ grain boundary precipitates. The wide scatter in the measurements is primarily due to sectioning effects and interfacial torque terms; in either case the distribution of measurements has a maximum coincident with the corrected values (Smith).

The corresponding interfacial energy for the α precipitates is $\gamma_{\gamma\beta} \approx 0.75\ \gamma_{\beta\beta}$. For a β/β grain boundary having an energy range 400-800 ergs/cm^2, $\gamma_{\alpha\beta}$ is 300-600 ergs/cm^2. The two α/β interphase boundaries exhibited equivalent energies, which is consistent with that expected of a FCC:BCC boundary.

The γ/β interphase boundaries of the γ allotriomorphs are of two types: a) a near coherent boundary separating mutually oriented γ and β lattices, and b) an incoherent boundary which accommodates the misorientation between the β grains. This is illustrated in Fig. 15, by the similarity of the grain boundary geometry for both γ/β

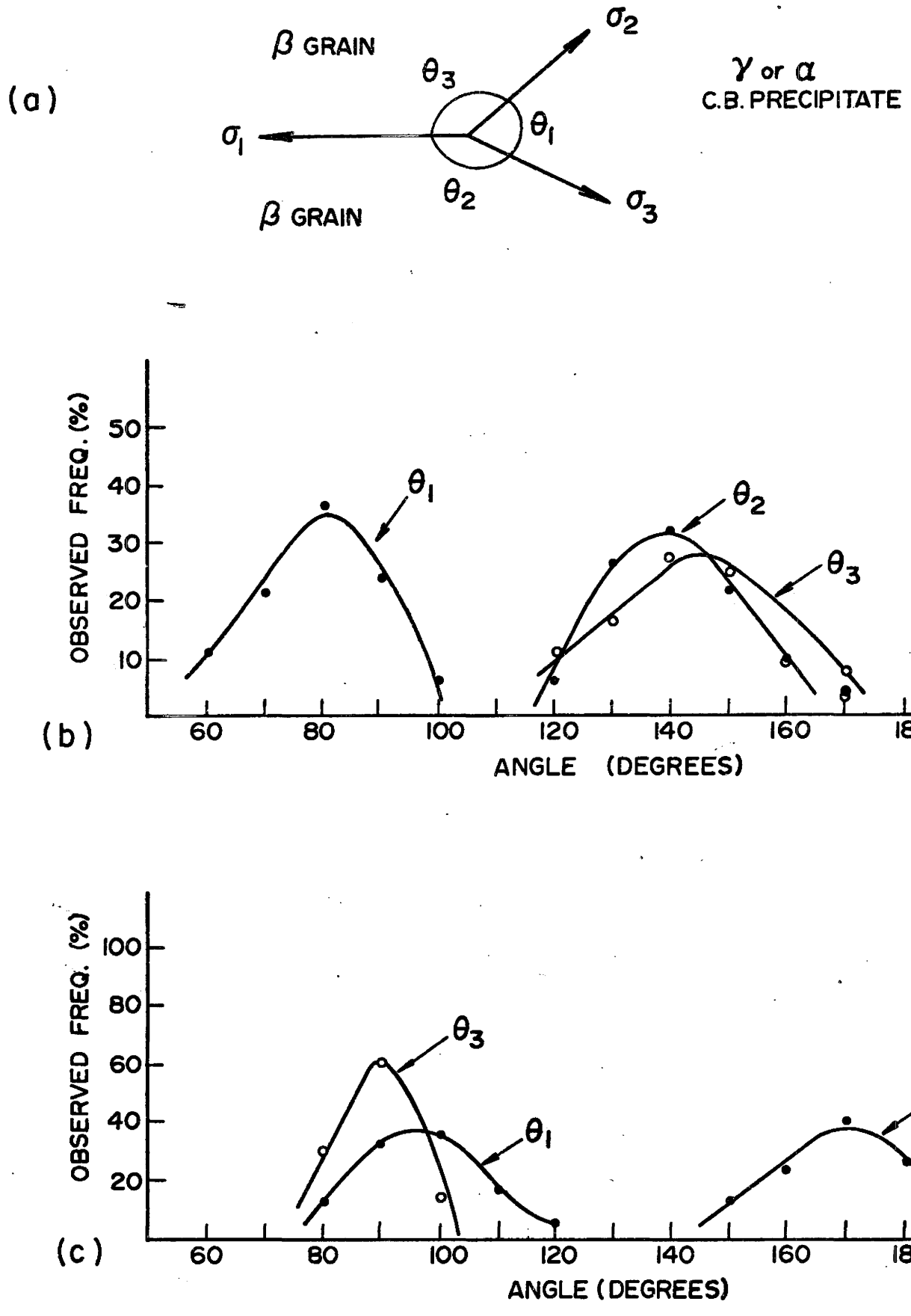

Fig. 14 : Dihedral angles, as defined in (a) are measured for (b) α and (c) γ grain boundary allotriomorphs between β crystals

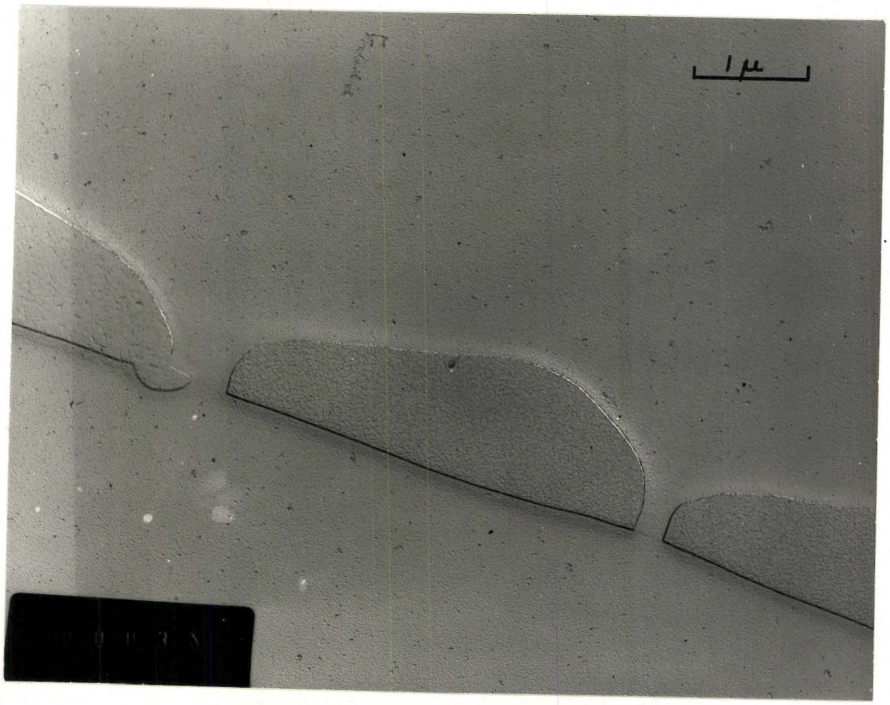

Fig. 15: A carbon replica of a γ grain boundary allotriomorph having a low energy interface separating phases of equivalent orientation and a high energy interface accommodating the misorientation between the β grains.

and β/β segments. The dihedral angle measurements give the energy of the coherent interphase boundary as 0.15 $\gamma_{\beta\beta}$ and the incoherent boundary as 0.9 $\gamma_{\beta\beta}$. For the same value of $\gamma_{\beta\beta}$, $\gamma_{\gamma\beta}$ INCOH is 350 to 700 ergs/cm^2 and $\gamma_{\gamma\beta}$ COH is 50 to 100 ergs/cm^2.

The fact that the coherent boundary of the grain boundary precipitates and the intragranular precipitates have similar orientations allows the experimentally determined values of the relative anisotropy of γ to be put on an absolute scale.

The statistical method of dihedral angle measurements has given an averaged value of the interfacial energy. The cusp oriented boundary planes would have a lower energy and contain a boundary torque component caused by the variation in surface energy with boundary orientation. The general definition of a boundary required both crystal misorientation and boundary position parameters. Gradients of boundary energy with crystal misorientation (from the Θ plot) tend to rotate the crystal lattices; gradients of boundary energy with inclination (from the γ plot) tend to rotate the boundary plane.

By detailed consideration of individual γ/β boundaries, the torque causing a boundary to rotate can be measured. In Fig. 16, the lattice misorientations have been determined by transmission Kossel microdiffraction and the boundary geometry after a 500 hour equilibration at 400°C has been measured. The electron beam contamination spots marked A to D denote the sites of the orientation measurements. The series of spots, used in a microanalysis

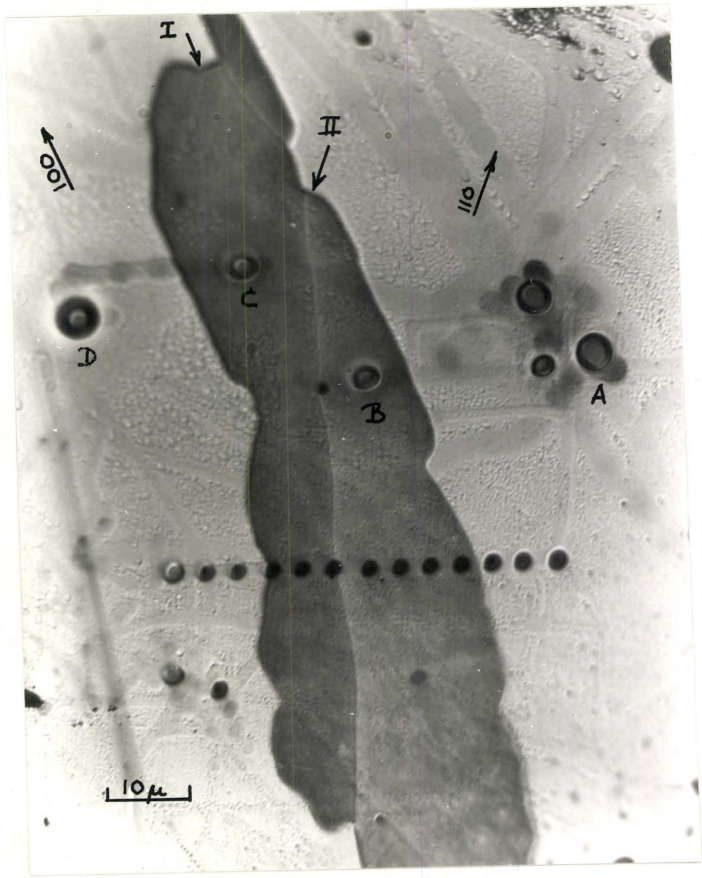

Fig. 16: The low energy γ/β interphase boundary, marked II, is rotated into a {110} cusp orientation while boundary denoted II is relatively unaffected by the rotational torques caused by the gradient in surface energy.

trace, provide exact correlation with the Kossel diffraction patterns. The grains A and D have respective surface normals near <321> and <110> yielding a 26^{o} misorientation at the B/C boundary. The boundaries A/B and C/D separate γ and β grains of equivalent crystallographic orientations, thus the variation in the geometry of the interface junctions marked I and II is due to the effect of a torque term tending to rotate the boundary into a minimum energy configuration. By comparing the crystallographic directions, <110> in grain A and <100> in grain B, with the anisotropy of interfacial energies measured in the following section by using equilibrated isolated particles, the coherent γ/β boundary at I is found to be completely free from the effect of interfacial torques and the boundary at II is in a {110} cusp orientation corresponding to a maximum in the rotational constraint. Herring (1951) showed the equilibrium geometry at a triple junction between phases was equivalent to having the sum of the components of surface tension and rotational torque equal to zero. (Eqns. 1.9 - 1.11). Hoffman and Cahn (1971) recognized that the combination of these terms reflected the equilibrium shape and introduced a vector function $\xi(\vec{n})$ where the normal components $\xi(\hat{n})_n$, represent the tendency for a surface to minimize free energy by contraction and the off-normal components, $\xi(\hat{n})_t$, represent the tendency of a surface to minimize free energy by rotation.

In the present case, the junction at I (Fig. 16) has no rotational term; the interfacial energy $\xi(\vec{n}) = \xi(\hat{n})_n$

is equal to a) $\sim$100 ergs/cm^2 using a dihedral angle measurement or b) $\sim$ 40 ergs/cm^2 using the theoretical value (section 5.3). Junction II has been rotated $\sim 30^\circ$ into the low energy orientation and the vector component $\xi(\vec{n})_n = \xi\cos 30^\circ$ gives the {110} cusp energy. This corresponds to a) 86 ergs/cm^2 based on the dihedral angle measurements and 34.5 ergs/cm^2 based on the theoretical model. The tangential contribution $\xi(\vec{n})_t = \xi\sin 30^\circ$ yields the maximum surface torque at the boundary. This is a) 50 ergs/cm^2 and b) 20 ergs/cm^2 for the respective measured and theoretical estimates of the energies of the partially coherent γ/β interphase boundaries.

5.5 Equilibrium Morphologies of Faceted γ Precipitates

Precipitation during the lower temperature isothermal treatments of supersaturated β phase resulted in the formation of faceted γ polyhedra. The boundary facets correspond to {110} planes of mutually oriented matrix /precipitates lattice thus giving a dodecahedron morphology (Fig. 17a)). A 3.1 methanol:nitric acid electrolytic etch has attacked the γ and β phases at different rates and the subsequent Au-Pt shadowed carbon replica captures the three dimensional morphology of the imbedded precipitates. The crystallographic dependence for the rate of dissolution can also be observed in the formation of the etch pits, (Fig. 17 b) at the γ/β boundary. The attack presumably originates at the stress field associated with the interface dislocations and growth causes agglomeration of the pits. The spacing of the smallest pits is consistent with the dislocation spacing (1300Å) while the larger pits are spaced at some

(a)

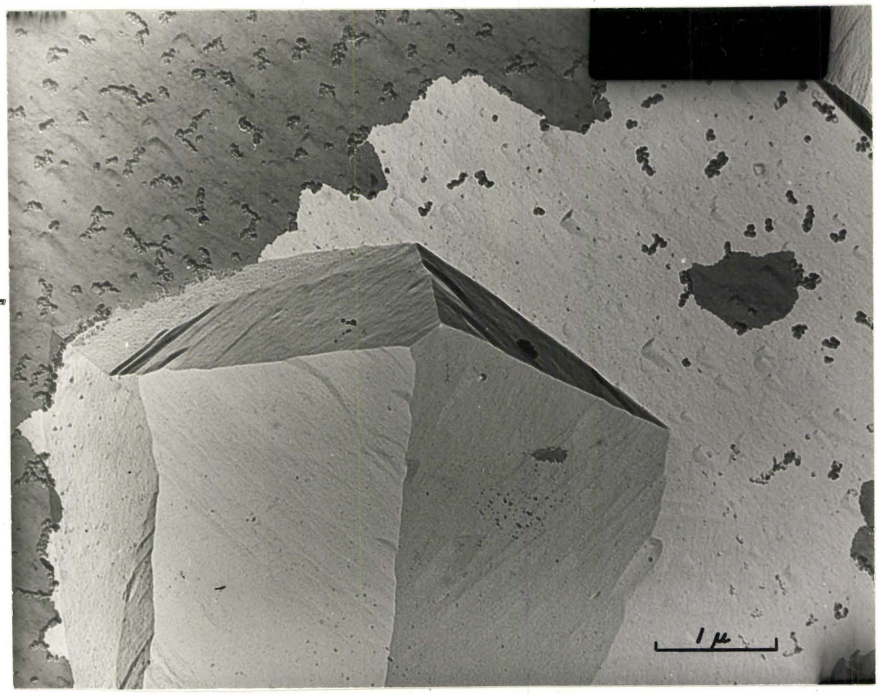

(b)

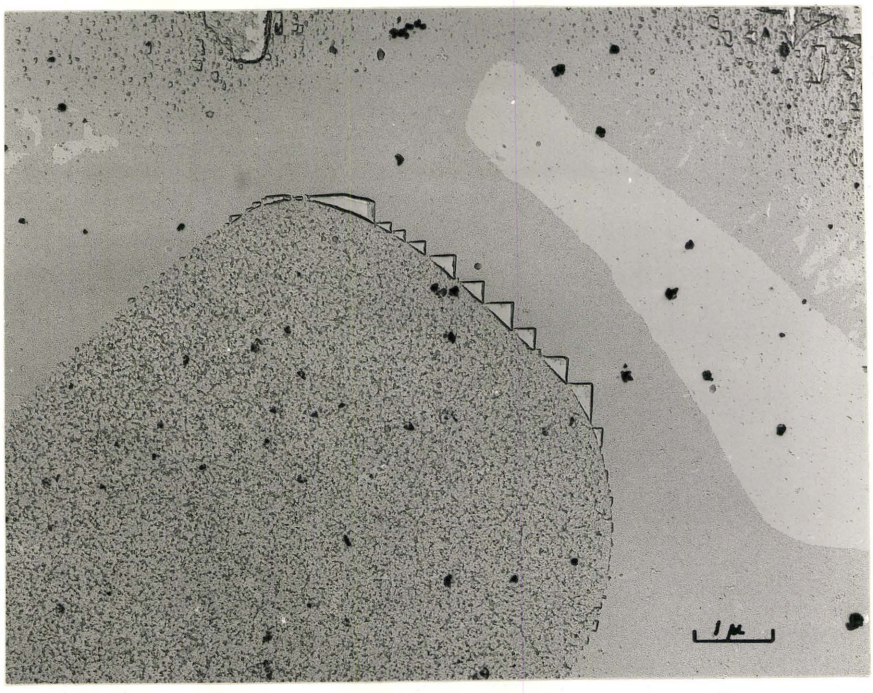

Fig. 17: Au-Pt shadowed carbon replicas exhibiting differential electrolytic attach in a methanol nitric solution and
a) captures the three dimensional morphology of the γ precipitates and
b) the formation of etch pits at the γ/β boundary.

multiple distance of the dislocation spacing. By comparing the two illustrations in Fig. 17 it is seen that the deep etched shapes are not representative of the actual morphologies . It was not possible to develop etching techniques which would preferentially attack only one phase to yield the equilibrium morphologies in relief; consequently a more cumbersome method of correlating planar sections through the precipitate to a dodecahedron model was necessary.

The equilibrated shapes (Fig. 18) exhibited corner rounding between the {110}facets; by measuring the radius at the corners the equilibrium morphology can be reconstructed. The morphology of γ precipitates in the β matrix was studied as a function of temperature by observing planar sections through the precipitates, either by optical or replica electron microscopy, and measuring the degree of rounding between adjacent {110} facets of the γ/β boundary. By determining the orientations of the individual β grains in the polycrystalline alloy using the Kossel microdiffraction technique, the measured radius of curvature was related to a {110} dodecahedron model and the sectioning effects considered. After a 500 hour isothermal equilibration treatment, the following results, based on approximately one hundred different precipitates at each temperature, were found:

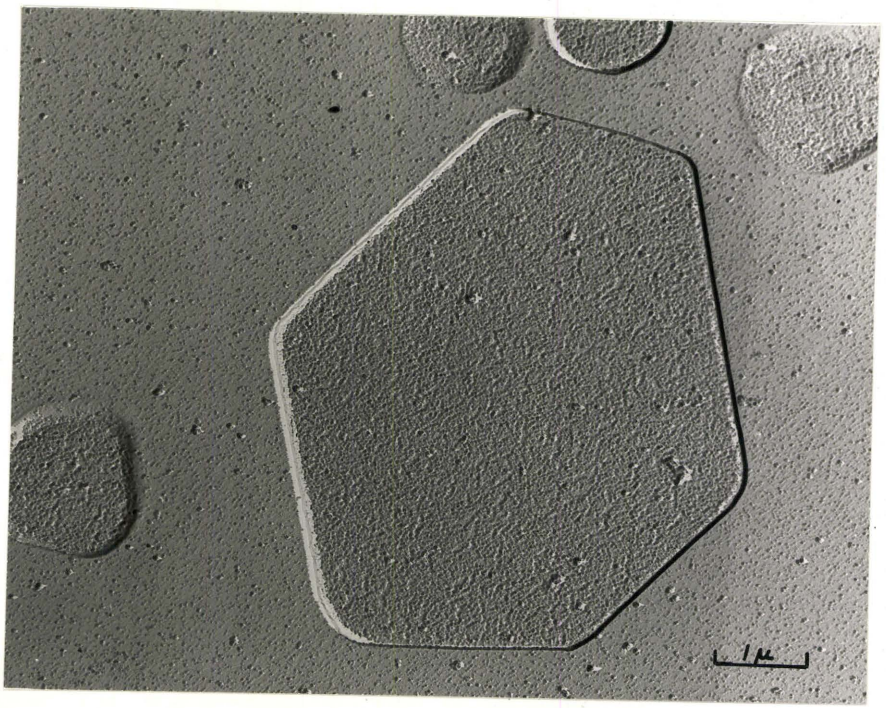

Fig. 18: Carbon replica of a γ precipitate after a 500 hour isothermal equilibration at 350°C showing {110} facets separated by rounded corners.

TABLE 8

Temperature °C	Average Corner Radius (μm)	Average Precipitate Diameter (μm)
300	3.5 ± 1.0	60 ± 5
350	8.0 ± 2.0	60 ± 5
400	11.0 ± 4.0	60 ± 5
500	150 ± 50	500 ± 50

The variation in precipitate size due to Ostwald ripening, necessitates a normalizing procedure given by the ratio of the corner radius:precipitate radius. The distribution of the observed ratios, in Fig. 19 shows the precipitates becoming increasingly spherical with temperature. At each temperature, the ratio remained constant over a wide range of equilibration times (and precipitate sizes) and indicated the observed shapes were representative of the equilibrium morphologies.

5.6 Anisotropy of the γ/β Interfacial Energy

The thermodynamic requirement that stable interface configurations minimize the total interfacial energy, $\int \gamma dA$, is consistent with an equilibrium shape defined by the inner envelope of a function, λ_{hkl}; a vector parameter proportional to the specific interfacial energy γ_{hkl} in a direction normal to the (hkl) plane and passing through the Wulff center (Eq. 1.8). In symmetric particles, the Wulff center is coincident with the particle center.

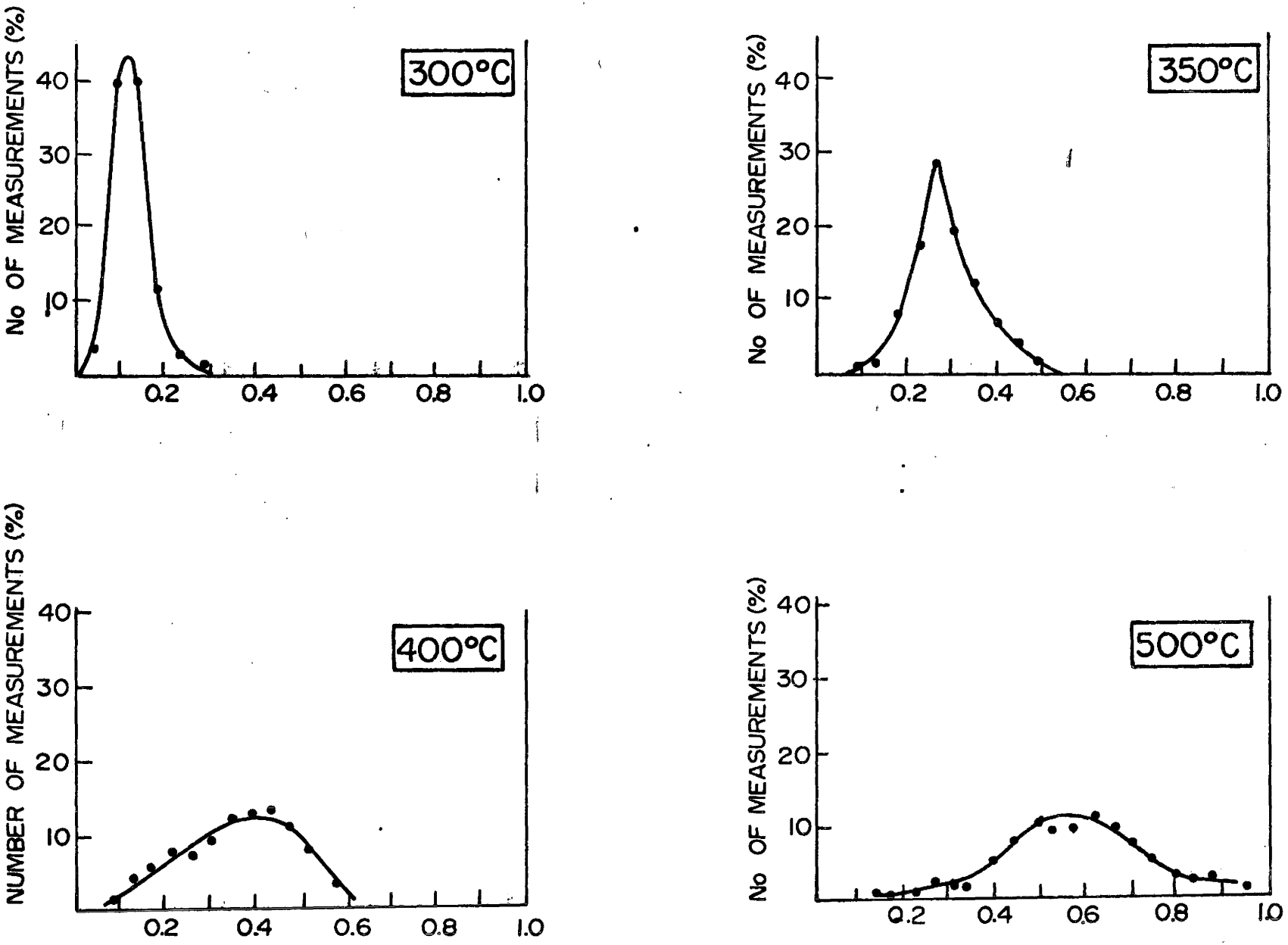

Fig. 19: Distributions of the ratio of corner : precipitate radii at various temperatures.

The orientation dependence of γ is thus reflected in the equilibrium shape; low energy cusps in the γ plot correspond to planar facets in the equilibrium morphology. The planar segments of the equilibrium shape are bounded by edges, which may be either curved or sharp. Curved edges imply that all possible interface orientations are present in the equilibrium shape and therefore define a unique γ plot. Sharp edges signify missing surface orientations and define only minimum values of the anisotropy of relative surface energies.

The measurements of equilibrated γ polyhedra in a β brass matrix were summarized in Fig. 19. With the degree of rounding at the edges of the {110} dodecahedron shaped γ precipitates known, the anisotropy of the γ/β interphase energy can be found.

Sections through the precipitate centroid are shown in Fig. 20 for (001), (111) and (110) planes; the inner solid curve corresponds to the measured equilibrated shapes and the outer dashed curve is the resulting polar γ plot. The unique determination is assured by the smoothly curved boundary separating the planar facets for interface orientations.

The effect of temperature on the precipitate morphology and on the γ/β interphase energy is illustrated in Fig. 21. The left quadrant of the [001] section represents the precipitate shape; the right quadrant represents the polar plot of surface energies. Morphologies marked A and F correspond to energies 1 and 6 respectively, and denote the range from spherical to faceted. The intermediate curves B

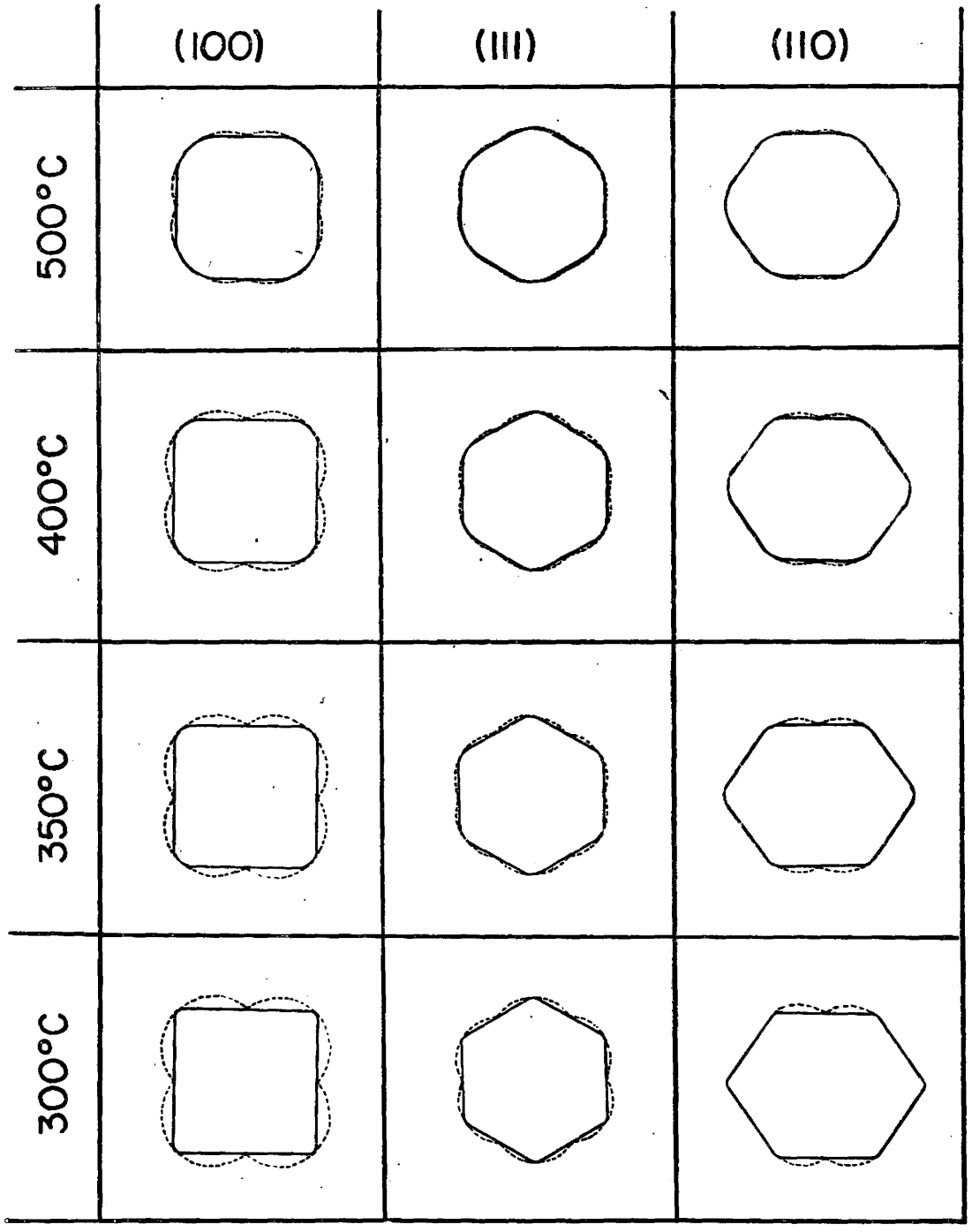

Fig. 20: The morphologies of the γ precipitates (solid curves) and the resulting Wulff Plots (dashed curves) for samples isothermally equilibrated for 500 hours at the temperatures designated.

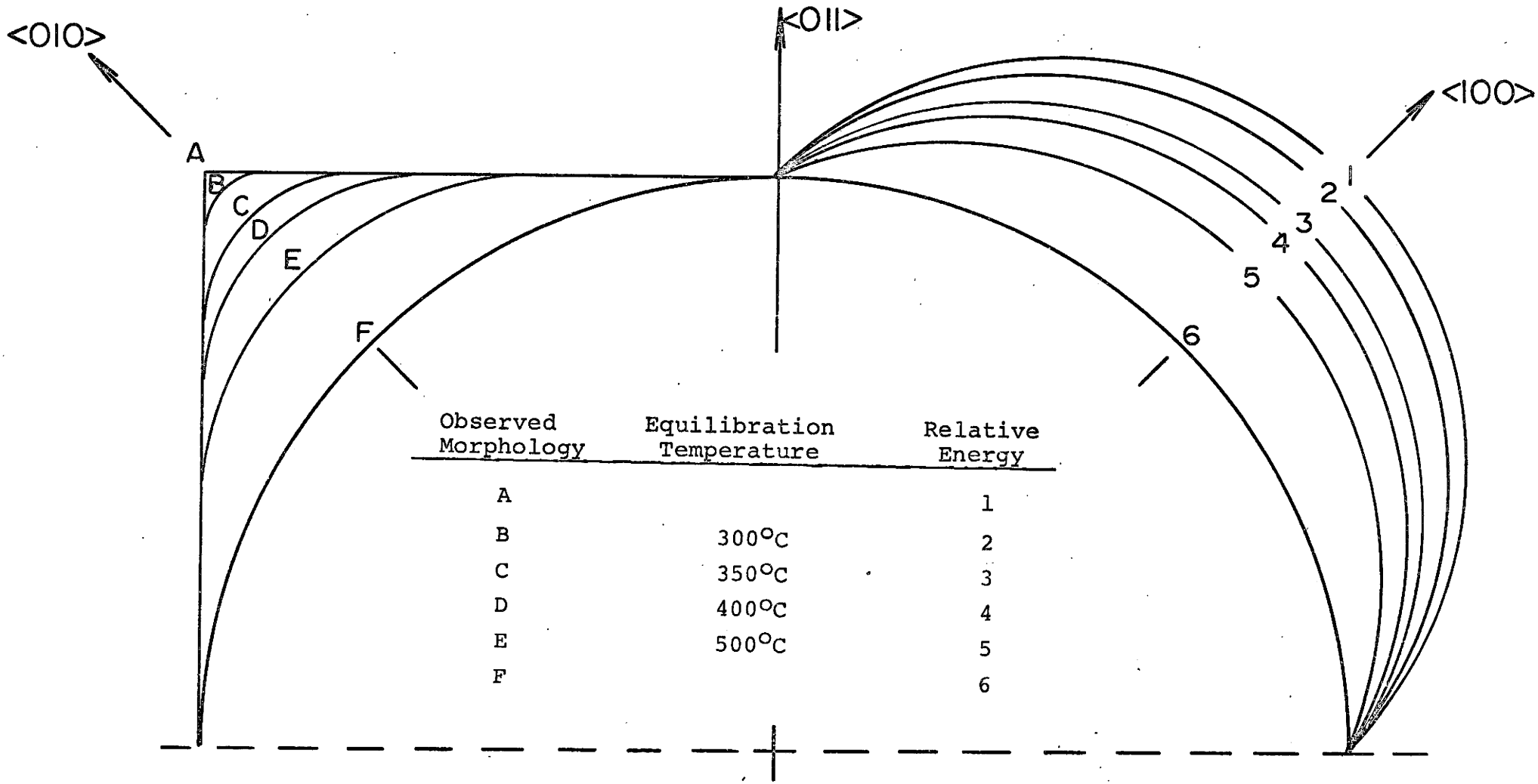

Observed Morphology	Equilibration Temperature	Relative Energy
A		1
B	300°C	2
C	350°C	3
D	400°C	4
E	500°C	5
F		6

Fig. 21: The equilibrium precipitate morphologies on a (100) section are represented on the left. The corresponding Wulff construction of the relative interfacial energies is shown on the right.

to E result from equilibration at various temperatures and allow the γ/β surface energies to be determined as a function of temperature.

By measuring the angles of intersection of iso-energy concentric circles with the polar γ plot, the results can be transferred to a unit stereographic triangle. These contours are plotted in Fig. 22 relative to γ_{100} of a completely faceted precipitate.

At low temperatures the surface energy is anisotropic with sharp cusps yielding {110} facets in the equilibrated shapes. At higher temperatures the surface energy becomes more isotropic and the precipitates tend toward a spherical shape.

The anisotropy is believed to arise from variations in the chemical and structural components of the interfacial energy; that is, the orientation dependence of the atomic binding forces and of the relaxed lattice positions respectively. The chemical bonding depends on the atom species present and their resulting bond strengths. The manner in which the induced strains are relaxed depends on the atomic structure of the interface and the elastic accommodation possible in each lattice.

For the γ/β interphase boundary, the structural contribution to the interfacial energy is due primarily to the dislocation grid relieving the disregistry between the γ and β lattices. The chemical component results from the number of wrong or antiphase bonds across the interface.

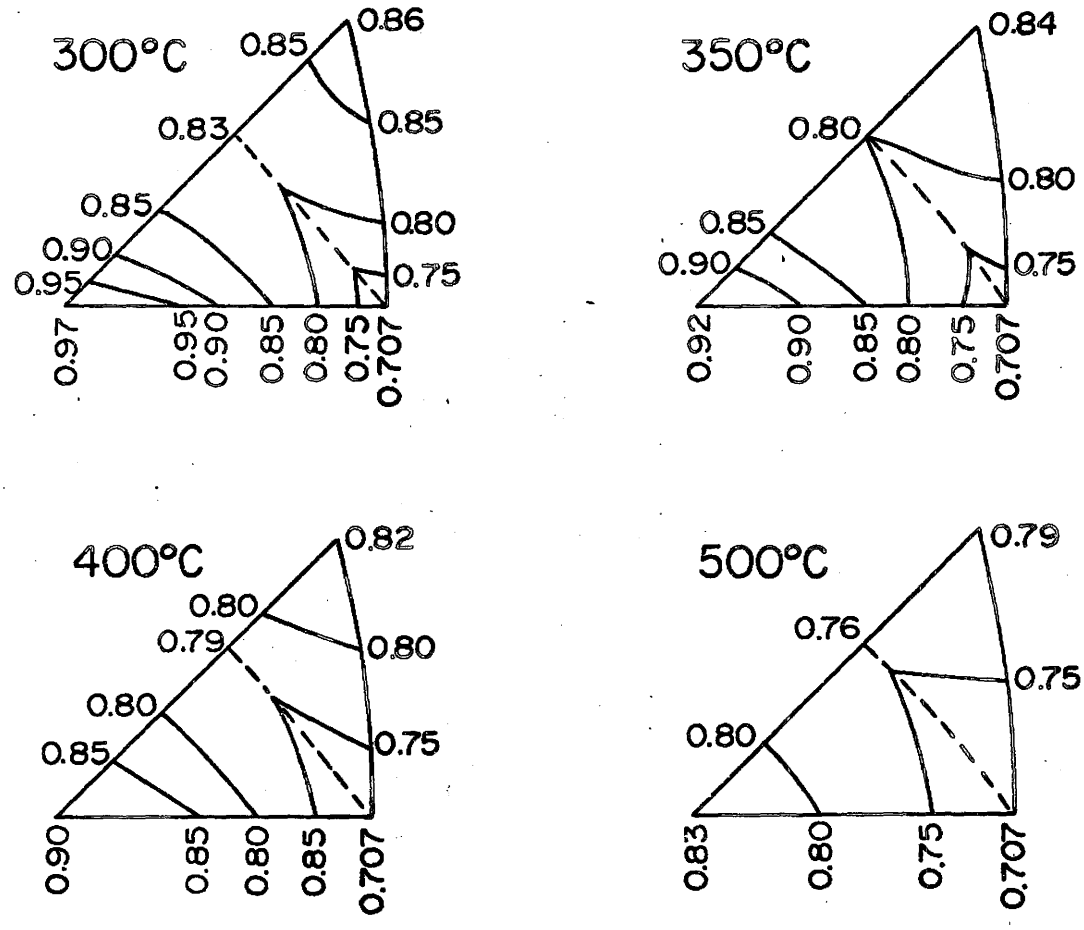

Fig. 22: Measured iso-energy contours for the unit stereographic triangle summarizes the relative anisotropy of interfacial free energy.

At temperatures above the order-disorder transition in β brass, the chemical contribution is small and the total boundary energy is dominated by the interfacial dislocation network. The network having an energy in the order of 50 ergs/cm^2, is made of dislocation loops having $\frac{a}{2}\langle 111\rangle_\beta$ Burgers vectors which result in a slight anisotropy due to the orientation dependence of the density of dislocations required in accommodating the lattice mismatch.

At temperatures below the order-disorder transition, an additional chemical contribution is imposed by the increased "antiphase" bonding across the boundary. The magnitude of the excess enthalpic chemical energy at the interface, ΔH^{chem}, depends on the difference in bonding at the γ/β interface and bonding in parallel planes in each phase. (i.e. $\Delta H^{chem} = H_{\gamma\beta} - \frac{1}{2}(H_{\gamma\gamma} + H_{\beta\beta})$). Consideration of atomic matching across idealized γ/β, γ/γ and β/β interfaces indicates that only the bonds at a β/β boundary are significantly influenced by the ordering reaction in the β phase. The interfacial enthalpy becomes a function of the long range order parameter.

An estimate of the orientation and the temperature dependence of the interfacial energy based on this theoretical model was tabulated in section 5.3 (Table 7) for the minimum (110) and the maximum (100) energy planes. The comparison with the measured temperature dependence of the anisotropy of the γ/β boundary energy is shown in Fig. 23. At higher temperatures the structural term presumably dominates yielding a relatively isotropic energy. Below the order-disorder

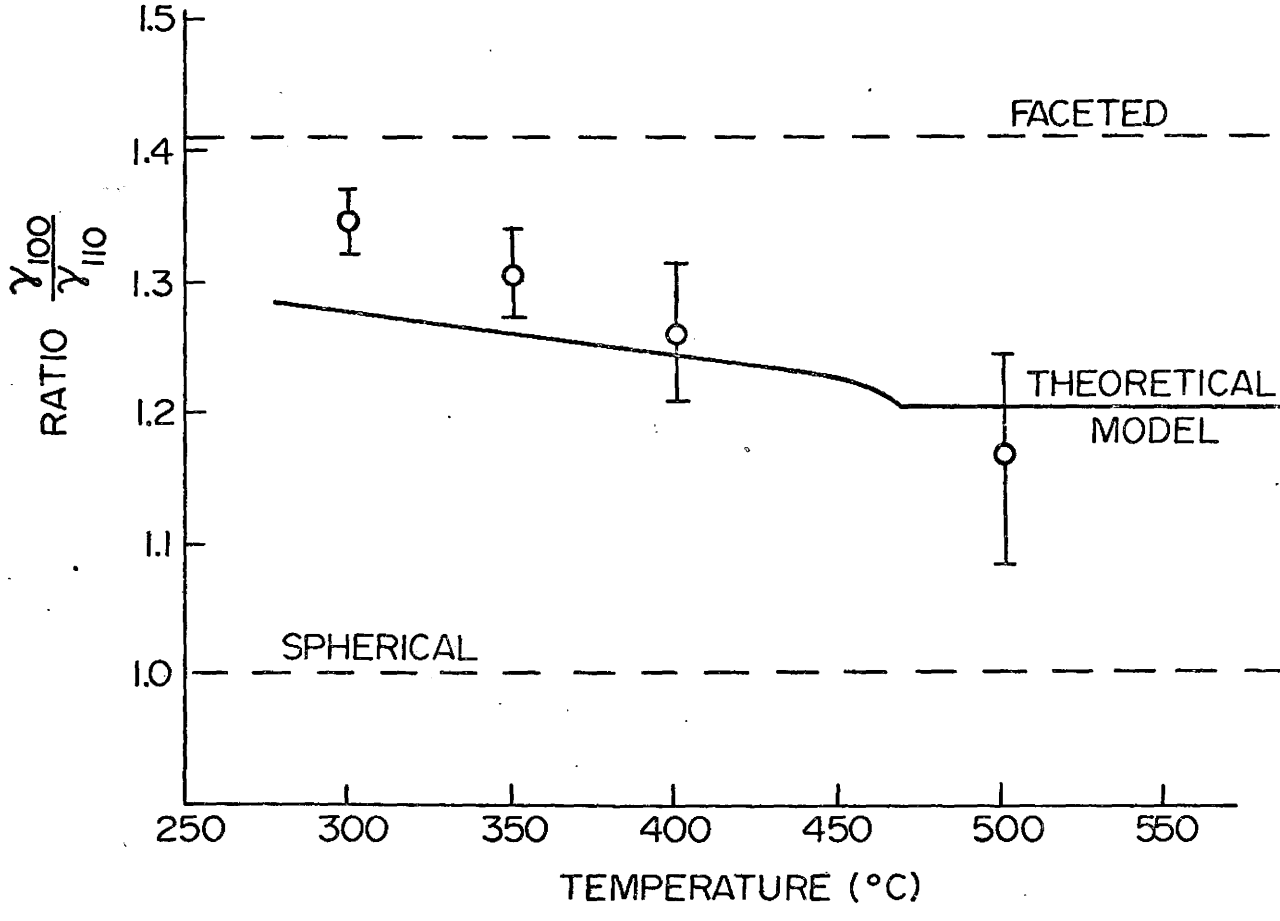

Fig. 23: A comparison of the measured temperature dependence of the maximum anisotropy of the energy of the γ/β boundary with a theoretical model based on the atomic structure of the interface.

transition, the increasing chemical contribution adds to the anisotropy of the interfacial energy and results in the formation of cusp oriented {110} faceted boundaries.

The model of the structure of the γ/β interphase boundary bases the energy on the sum of chemical and structural terms, with the net effect of anisotropy in either component proportional to its relative magnitude. The model appears qualitatively consistent with all the observations and shows the temperature dependence of the anisotropy need not be related to interfacial entropies which are expected to be low in this system.

CHAPTER 6

RESULTS AND DISCUSSION

THE MIGRATION OF γ/β INTERPHASE BOUNDARIES

6.1 Introduction

Interface mobility measures the response of a boundary to an applied driving force. In solid state transformations, the driving force arises from the change in free energy associated with the formation of the reaction products. The transformation from one phase to another, which can involve both compositional and structural changes, is accompanied by a resistance to boundary motion. The resistance is overcome by a departure from local equilibrium at the interface which causes a reduction in the free energy available for solute redistribution. In the extremes, the transformations are termed volume diffusion controlled and interface reaction controlled.

The $\beta \rightarrow \gamma$ transformation in Cu-Zn alloys is of particular interest in that both compositional and structural parameters are known, and both may contribute to the control of the kinetics of γ/β interphase boundary migration.

In the following sections, the dendritic growth at higher temperatures and the polyhedral growth at lower temperatures are considered.

By comparing the isothermal precipitation kinetics of γ dendrites and α rods from equivalently supersaturated solid solutions of β, it is possible to deduce the factors controlling the rate of interface advance. The only unequal parameter affecting the migration kinetics between the two precipitates is the interfacial free energy. This was determined by measuring the ratio of the γ/β and α/β interphase boundary energies, utilizing a dihedral angle technique at equilibrated grain boundary allotriomorphs. The relative energy measurements allowed a direct comparison of the dendrite growth kinetics. It was found that the α rods lengthened by volume diffusion control with negligible interface resistance. For an equivalent theoretical analysis, the γ dendrites lengthened at a rate less than predicted by solute diffusion. A linear kinetic coefficient was determined and tentatively attributed to the interfacial ordering reaction accompanying the boundary migration.

At a lower temperature, the interface migration characteristics of the cusp-oriented {110} boundaries of γ polyhedra precipitates were measured by observing antiphase boundary contrast effects. This allowed the inference that a ledge mechanism operated during the advance of the interface. Lateral motion of ledges on adjacent {110} facets is considered to result in an anisotropic interface advance rate which is reflected in the observed growth morphologies.

6.2 Symmetric Dendrite Precipitation Reactions

A direct comparison of the migration kinetics of the FCC/BCC Kurdjumov-Sachs oriented α/β interface with a

BCC/BCC mutually oriented γ/β interface was made. By considering similar precipitation reactions in the same β matrix, uncertainties stemming from errors in diffusion coefficients and thermodynamic parameters are reduced. The following experiments in the copper-zinc system were designed to complement the investigations of Purdy (1970), and Bainbridge and Doherty (1970).

Purdy examined the linear growth kinetics of α rods in β brass at 400°C for supersaturations, Ω_o, of 0.2 and 0.4. The analysis considered the non-ideal solution behavior of the β phase by using the thermodynamic factor described by Darken (1948):

$$e_{1\beta} = e_{1\alpha} = \left[1 + \frac{\partial \ln \gamma_{1\beta}}{\partial \ln x_{1\beta}}\right]\Bigg|_{x_{1\beta}} \qquad (6.1)$$

which relates the variation in activity coefficient, $\gamma_{1\beta}$, with the concentration $x_{1\beta}$. Calculations, using thermodynamic data from Hultgren et al (1963) show $e_{1\beta}$ to be non-unity; consequently, the Gibbs-Thomson expression and the diffusion coefficient required corrected values:

$$x_{1\beta}{}^{r} = x_{1\beta}{}^{o}\left\{1 + \left(\frac{x_{2\beta}{}^{o}}{x_{1\alpha}{}^{o} - x_{1\beta}{}^{o}}\right)\frac{2\gamma \bar{V}_{1\alpha}}{rRTe_{1\beta}}\right\} \qquad (6.2)$$

where $x_{1\beta}{}^{r}$ = solubility of component 1 in the β phase for a particle of radius r

$x_{1\beta}{}^{o}$ = equilibrium (infinite radius) solubility

γ = interfacial free energy

$\bar{V}_{1\alpha}$ = molar volume of component 1 in the α form

and: $$D = e_{1\beta} \{x_{1\beta} D^*_{2\beta} + x_{2\beta} D^*_{1\beta}\} \quad (6.3)$$

where D^*_β is the radioactive tracer diffusion coefficient. The experimental results confirmed that the fastest growing α rods are in accord with volume diffusion in the β phase controlling the α/β interphase boundary migration.

Bainbridge and Doherty measured the γ dendrite growth kinetics for low (<0.1) supersaturations in the temperature range 482°C - 526°C and reported the γ dendrites to be growing at a rate slower (x7) than the α rods. The opposite is predicted from the diffusion controlled growth model as the interface velocity varies inversely with the boundary energy. With the interface energies determined, the present investigation into dendrite growth considers the α and γ isothermal precipitation reactions at higher supersaturations where a proportionately greater departure from local equilibrium would be necessary to drive the interface.

Initial plans involved studying the γ precipitation kinetics at the same supersaturation and temperature as was used by Purdy in determining α rod kinetics. Dendritic precipitation of the γ phase, however, did not occur at 400°C since the higher nucleation rate and the more anisotropic surface energies resulted in the formation of γ polyhedra. This necessitated observing both the α and γ precipitation reactions at a higher temperature.

6.3 Kinetics of α Rod Formation

The objective in determining the α rod kinetics at 520°C was to verify the volume diffusion controlled α/β interface migration model, using Trivedi's (1970) analysis of

growth kinetics and incorporating non-ideal thermodynamic behavior (Purdy, 1970). Samples were isothermally reacted at 520°C for various times and the longest rods were measured (Fig. 24) using the Cambridge Stereoscan II scanning electron microscope with deep etched sections (Purdy, 1970). The α rods were densely packed and often interpenetrating; nevertheless, the longest rods did yield a linear lengthening rate of 30 μm/sec. The rod morphologies were similar to those observed by Purdy (1970) and had a radius < 0.25 μm.

The theoretical and experimental growth rates are tabulated in Table 10 in the following section. The excellent agreement indicates that the α rods lengthen by a diffusion limited process and gives confidence in applying the thermodynamic and diffusion data (Table 9) to the γ dendrite precipitation reaction.

6.4 Kinetics of γ Dendrite Formation

The rate of lengthening of the γ dendrites was determined in a manner similar to that used for the α rods; that is, by the measurement of the longest dendrite after appropriate isothermal reaction times at 520°C. The intergranular γ dendrites grow in opposing <110> directions which led to some uncertainty in measuring the lengths corresponding to unidirectional interface migration. The lengths which are shown in Fig. 25 for supersaturations Ω_o of 0.2 and 0.4 represent overall dendrite lengths and therefore represent an upper limit of the γ/β interface velocity.

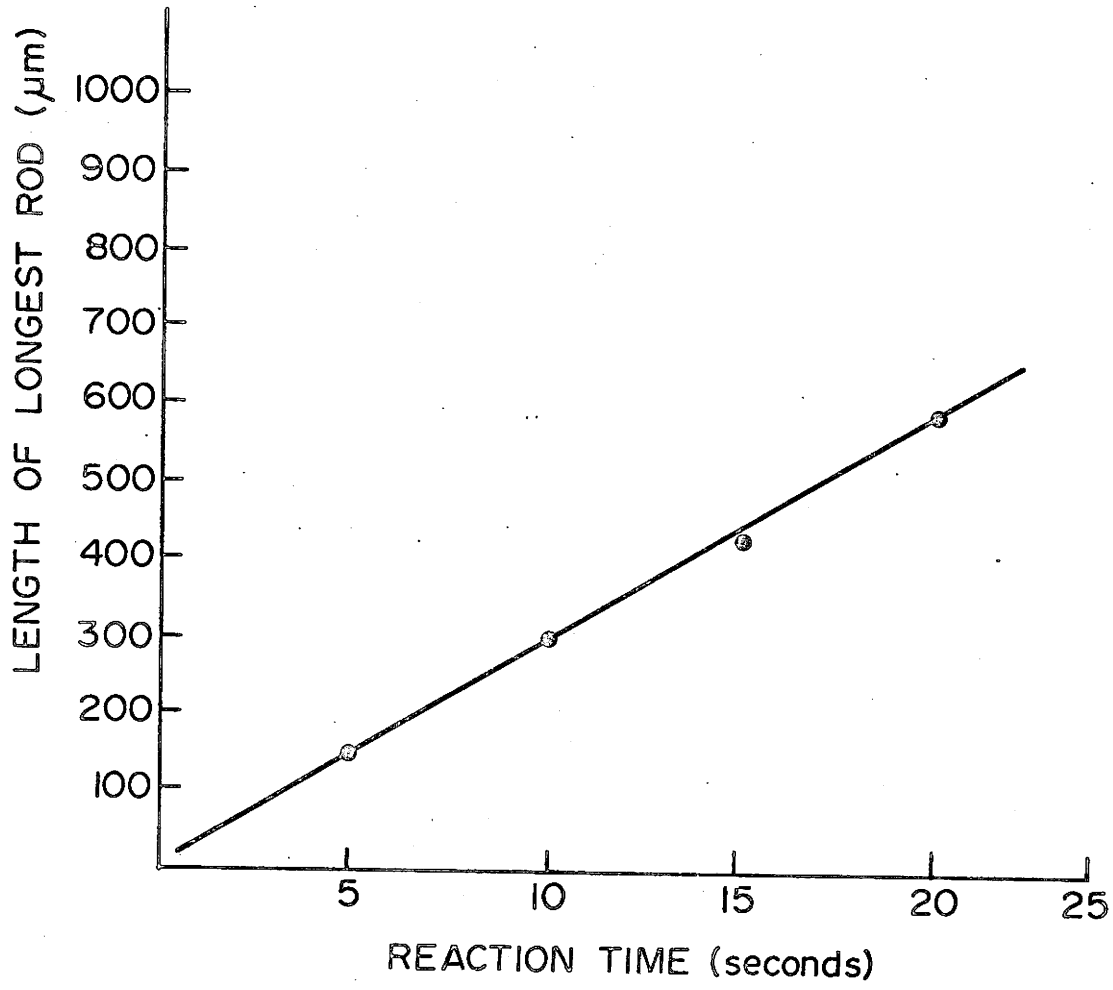

Fig. 24: Lengthening kinetics of α rod formation during isothermal growth at 520°C and supersaturation Ω_o = 0.5 yielded a linear velocity of 30 μm/sec.

TABLE 9: Parameter values used in Calculating rates at 520°C

	α rods	γ dendrites	
Symbol	Value	Value	Source
D_β	$4.2 \times 10^{-8} \frac{cm^2}{sec}$	$4.2 \times 10^{-8} \frac{cm^2}{sec}$	Kuper et al
$e_{1\beta}$	5.3	5.3	Hultgren et al
V_{ppt}	7.34 cm^3/mol	8.3 cm^3/mol	Pearson, Owen and Pickup
V'_{ppt}	7.82 cm^3/mol	8.66 cm^3/mol	Pearson, Owen and Pickup
σ	$500 mj/m^2$	$50 mj/m^2$	Measured
$x^o_{1_{ppt}}$	0.380	0.569	Hansen
$x^o_{1\beta}$	0.440	0.488	Hansen

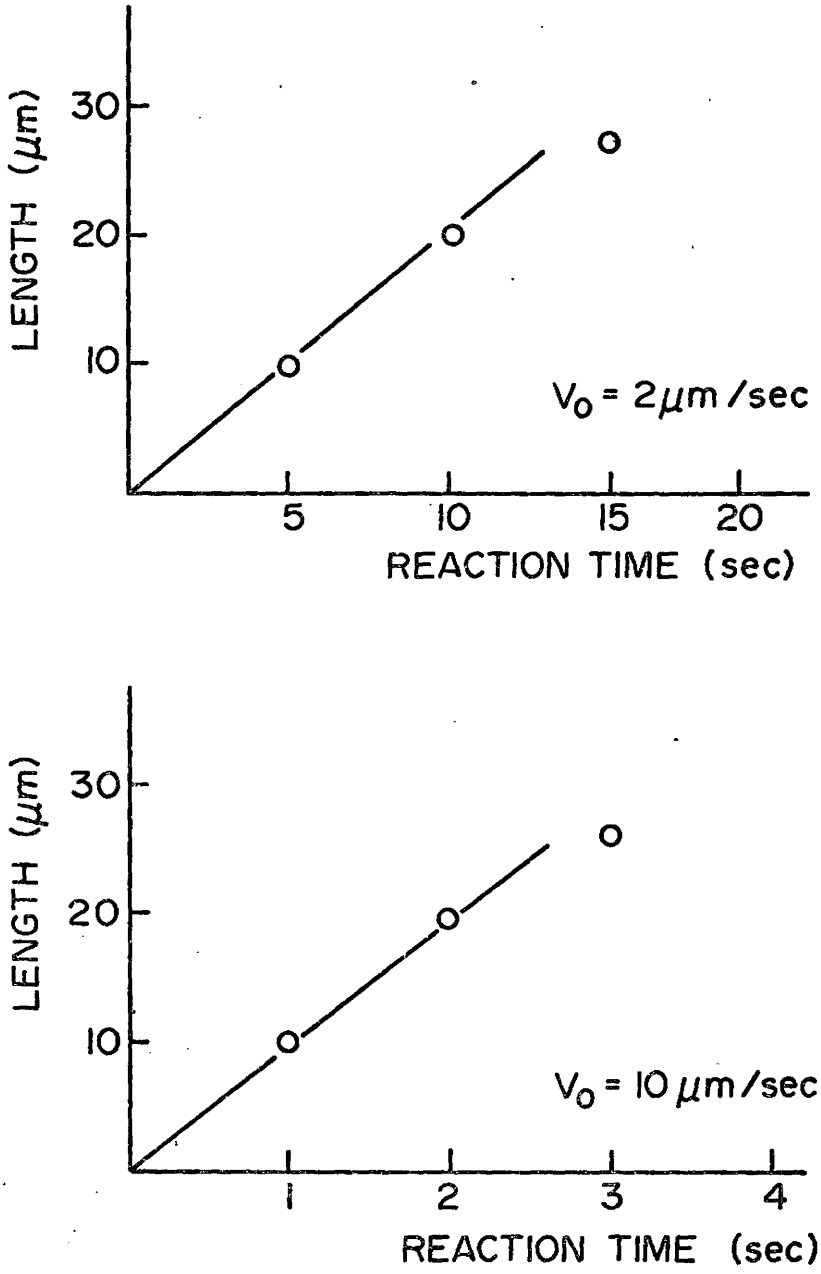

Fig. 25 : The lengthening kinetics of the formation of γ dendrites at 520°C and a supersaturation of:
a) $\Omega_o = 0.20$ and b) $\Omega_o = 0.40$

Tiller (1970) considered the available free energy to be the sum of the components necessary to provide for heat and solute transport, for formation of a non-equilibrium phase and for interface motion. Each contribution is considered "in series" and coupled. The transformation rate therefore can always be given explicitly by the solution of the appropriate diffusion equation where the interface concentration has been corrected to include the non-equilibrium and interface reaction compounds. Both of these effects are accounted for in the solution of the diffusion equation applicable to dendrite growth given by Trivedi (1970). Restated (eqn. 2.12):

$$\Omega_o = pe^{p} E_1(p) \left[1 + \frac{r_c}{r} \Omega_o R_2(p) + \frac{V}{V_c} \Omega_o R_1(p)\right] \qquad (6.4)$$

where the first term is the Ivantsov solution for an isothermal dendrite; the second term corrects the interface equilibrium concentration for curvature, and the third term accounts for a linear reaction accompanying boundary migration.

The solution involving only the first two terms was found to apply to the kinetics of α rods and led to the conclusion that the transformation proceeded by volume diffusion control. Similar calculations for the γ dendrites show the growth to be significantly slower than predicted by volume diffusion.

Constant kinetic coefficient, defined as:

$$V_c = \mu_o \left(C_\beta^r - C_\beta^\infty\right) \qquad (6.5)$$

was fitted to the data. The effect of such a term in Trivedi's solution can be seen in Fig. 26 for calculations involving a

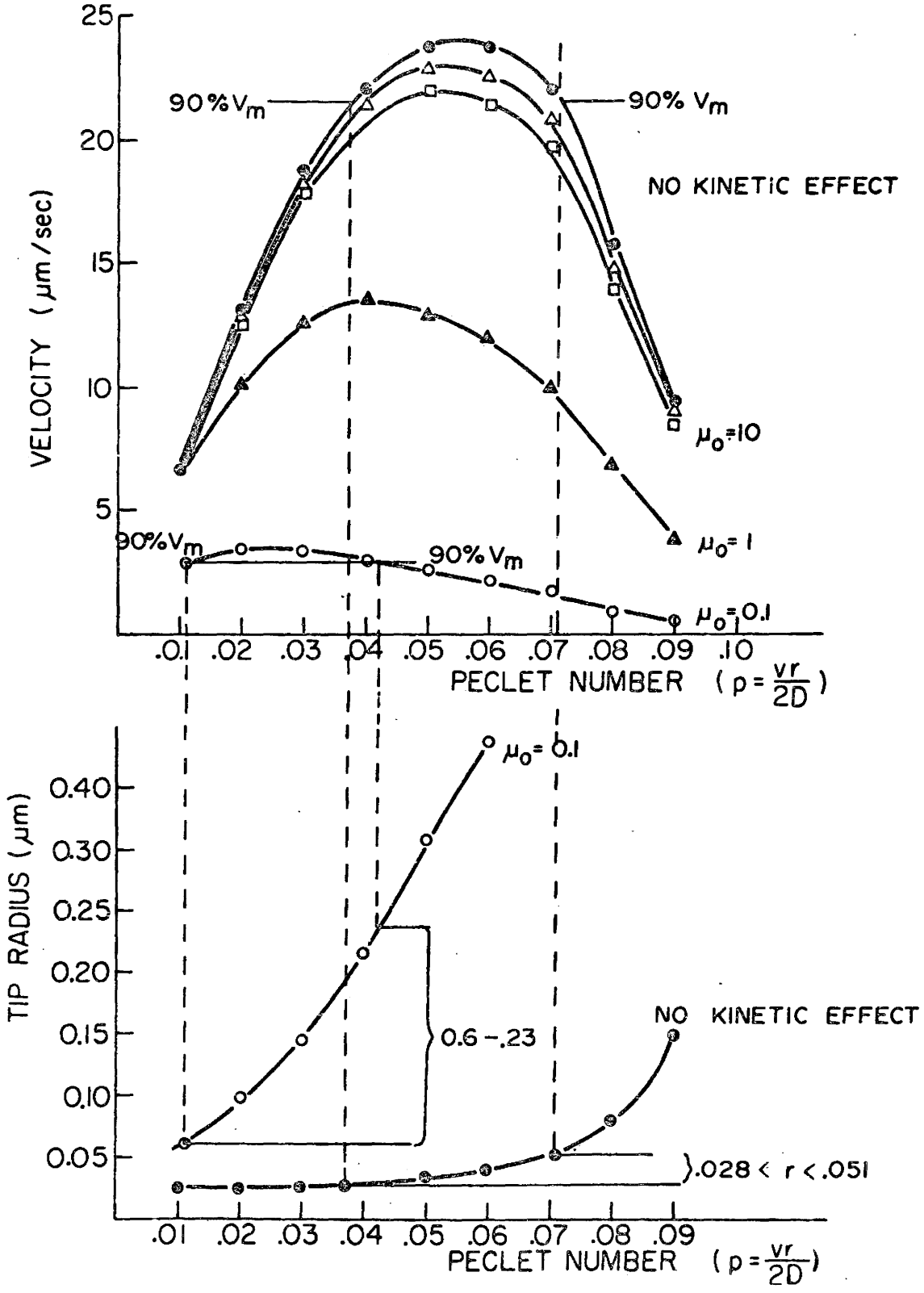

Fig. 26 : The velocity of dendrite growth and the tip radius predicted from Trivedi's (1970) analysis plotted as a function of peclet number for a dimensionless supersaturation of 0.20 illustrating the increasing effect of kinetic control (μ_o decreasing)

supersaturation of $\Omega_o = 0.2$. The solid line represents the volume diffusion controlled solution; the dashed lines illustrate the effect of increasing kinetic control. In either case an optimization criterion is necessary to define a unique solution. While no proper theoretical basis exists for the choice, experimental evidence tends to support choosing a radius of tip curvature which maximizes the tip velocity. This principle should hold regardless of v - r pair selection when measurements are based on maximum length observations. It was found that a kinetic coefficient $\mu_o = 0.08$ was consistent with the data. This is shown in Table 10. The reduced maximum velocity resulting from an interface kinetic term is accompanied by an increased tip radius and is in agreement with the observations.

The data and theoretical curves are plotted as a function of supersaturation in Figure 27. The increased velocity occurring at the higher supersaturations provide enhanced sensitivity in determining the deviations due to kinetic effects.

The value of $\mu_o = 0.08$ obtained is a measure of the γ/β interface resistance to motion. This resistance is usually attributed to the atomic attachment mechanisms which cause rearrangements of atom species and/or atom sites, resulting in a compositional and structural barrier to growth. The equilibrium behavior of the γ/β interphase boundary which was determined in the previous chapter was considered for similar compositional and structural terms and is useful in determining the cause of the kinetic coefficient.

TABLE 10: COMPARISON OF OBSERVED AND CALCULATED QUANTITIES

No Interface Kinetic Effect $\mu_o = 0.08$

Supersaturation Ω_o	Observed Maximum Velocity (μm/sec)	Observed Range of Tip Radii for Longest Rods (μm)	Calculated Maximum Velocity (μm/sec)	Calculated Tip Radii for V $0.9V_{max}$ to V_{max} (μm)	Calculated Maximum Velocity (μm/sec)	Calculated Tip Radii for V 0.9 V_{max} to V_{max} (μm)
α in β, 400°C (1)						
0.2	0.16	0.13 - 0.25	0.15	0.13 - 0.25		
0.4	4.7	< 0.05	7	0.03 - 0.05		
α in β, 520°C (3)						
0.5	30	0.1 - 0.2(5)	35	0.11 - 0.19		
γ β, T.varied (2)						
0.5	0.3	0.4 - 0.7	0.5	0.16 - 0.32	0.25	0.24 - 0.52
0.10	1.0	0.2 - 0.4	3.6	0.06 - 0.10	0.8	0.12 - 0.34
γ in β, 520°C (3)						
0.2	2	< 0.25	24	0.03 - 0.06	2.7	0.08 - 0.25
0.4	10	< 0.50	245	0.01 - 0.02	8.2	0.05 - 0.43

(1) Purdy, 1970 (2) Bainbridge and Doherty, 1970 (3) Present investigation

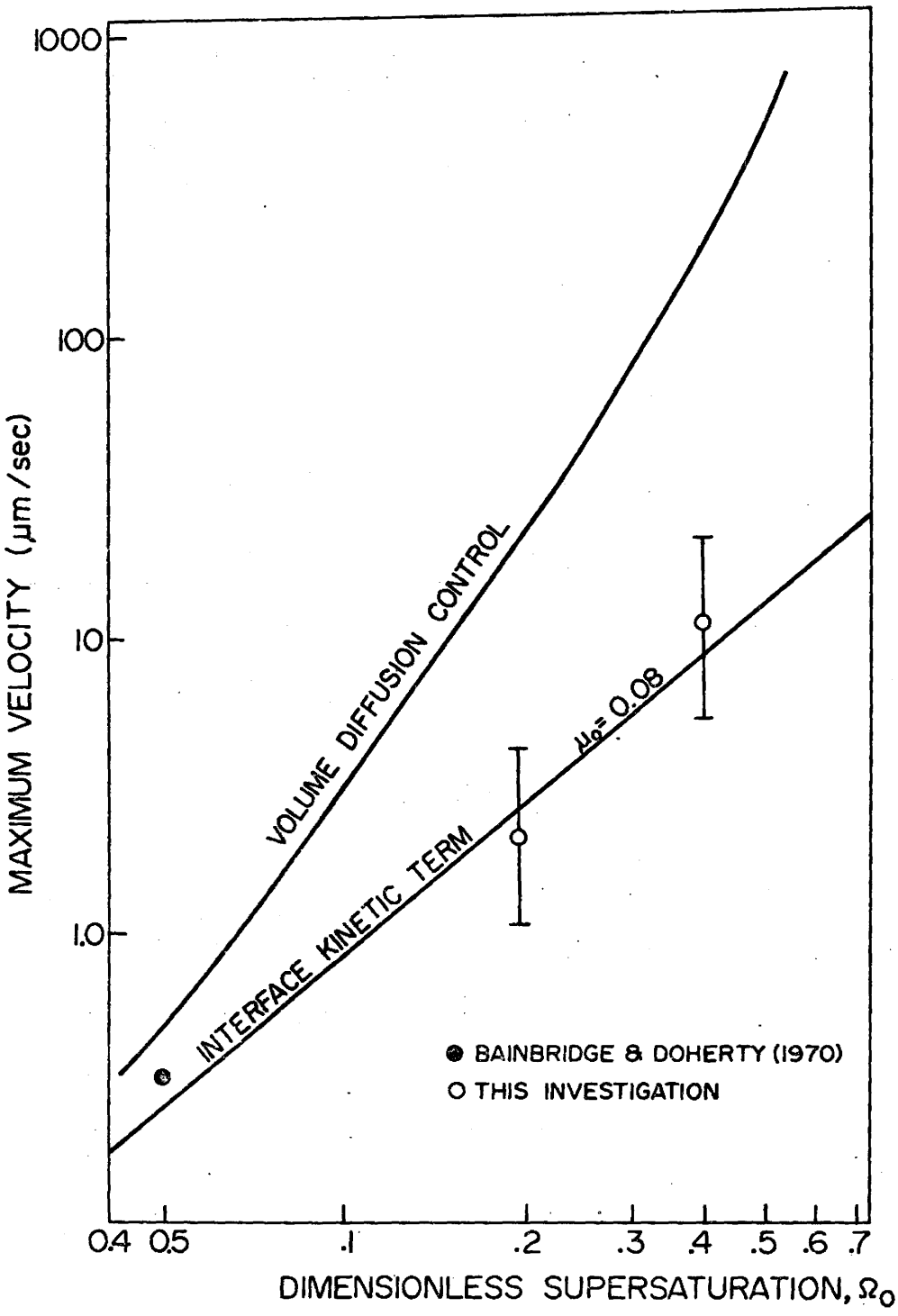

Fig. 27 : The maximum velocity of a parabolic dendrite tip (Trivedi, 1970) is plotted as a function of supersaturation and a linear kinetic coefficient accounting for the deviation from the rates predicted by volume diffusion, is determined.

The partially coherent γ/β interface was found to separate mutually oriented β and γ phases of slightly differing lattice parameters. The misfit or volume transformation strain is accommodated by an interface dislocation network.

The similarity of the two phases, both in structure and in composition, discredit the potential barriers found in most phase transformations. The most probable rate controlling steps are:

a) the vacancy flux required to form the γ structure

b) the interface resistance caused by the climbing dislocation network

c) the interface resistance accompanying the interfacial ordering reaction.

d) the interface resistance due to an accumulation of transformation strain.

The structural transition requires two vacancies forming in each γ unit cell comprising 54 sites (for an interface vacancy concentration of 3.71×10^{-2}). The vacancy flux requirement necessitates the coupling of the diffusive fluxes (Russell) and the provision for appropriate source and sink terms. The primary source of vacancies during the transformation is assumed to be the quenched vacancy supersaturation formed during the heat treatments.

Vacancy concentrations of 10^{-4} for β brass specimens quenched from $850^{o}C$ have been measured by Corrie. When used in conjunction with the internal friction measurements of Clarebrough an expression for the vacancy concentration can

be formulated:

$$N_v = 0.1 \exp\left(\frac{-15,400}{RT}\right) \tag{6.6}$$

The β matrix vacancy concentrations for the 700°C solution treatment and a 520°C precipitation treatment are 3.6×10^{-5} and 0.6×10^{-5} respectively. The decay of the vacancy supersaturation, Ω^v, can be described by an equation of the form:

$$\Omega^v = \Omega^v_o \exp(-t/\tau) \tag{6.7}$$

where the relaxation time

$$\tau = \frac{\ell^2}{D\pi^2} \tag{6.8}$$

The grain boundaries offer external vacancy sinks which for $\ell \approx 0.1$ cm yield a relaxation time of 60 seconds. In this time the supersaturation will have decreased to 1/e of its original value.

The interface velocity estimates from the measured lengthening rates are for reaction times less than ~20 seconds thus the vacancy supersaturation is expected to be retained.

By considering the interface migration controlled by the vacancy flux from the supersaturated β matrix source to the interphase boundary sink, the dendrite growth expression (Ivantsov) is written:

$$\Omega^v = pe^p E_1(p) \tag{6.9}$$

where $p = vr/2D_v$ and D_v is the vacancy diffusion coefficient. Substituting $\Omega_v = 0.8 \times 10^{-3}$, $D_v = 1.6 \times 10^{-5}$ cm^2/sec (Brown 1959) yields an order of magnitude greater than that

observed. It is therefore unlikely that the dendrite growth is controlled by the vacancy flux required for the structural change.

An interfacial dislocation is subjected to a climb force, F, during boundary migration (Hirth and Lothe, 1967)

$$\frac{F}{L} = \sigma_{xx} b + \frac{-kTb}{V_a} \ln \frac{C}{C_o} \tag{6.10}$$

where the first term is the Peach-Koehler relation due to an imposed stress σ_{xx}, and the second term is the Bardeen-Herring expression for the osmotic force caused by a supersaturation C/C_o, of vacancies. Misfit dislocations remaining in the boundary plane (and hence offering negligible resistance to the boundary migration) climb at a rate: (Hirth and Lothe, 1967):

$$v = \frac{2\pi D_v \, v_a \, (F/L)}{b_e^2 \, kT \, \ln(R/b)} \tag{6.11}$$

$$\approx \frac{2\pi D_v}{b_e \ln(R/b)} \left(\frac{C}{C_o} - 1 \right) \tag{6.12}$$

Substituting R = ½λ(interdislocation spacing) yields a velocity $v \approx 1$ cm/sec indicating the climb of the interface dislocations is not controlling the rate of dendrite growth.

The advance of the γ/β interphase boundary at 520°C must be accompanied by an interfacial ordering reaction requiring specific and comparatively long range rearrangements of both atoms and vacancies. If the diffusional interface migration rate is sufficiently fast, the ordering reaction might limit the dendrite growth kinetics. A parallel ordering

reaction with only short range atomic rearrangements occurs in the $\beta \rightarrow \beta'$ transformation at a lower temperature. The kinetics of ordering have been measured by Moore with 250 μm domains obtained on 10^{2}°F/sec quenches which would correspond to velocities in the order of 100 μm/sec. The more complicated $\beta \rightarrow \gamma$ ordering reaction would be expected to be slower.

The dilational lattice strain energy for an ellipsoidal shape in an isotropic matrix has been developed by Eshelby (1963). The strain energy per unit volume of precipitate was found to be independent of precipitate size and can therefore be treated in an analogous manner as surface energies of small particles; that is, the net effect is to form a higher specific energy product phase which decreases the available free energy for the transformation. This effect would be most pronounced at low supersaturations; which is opposite to the present observations.

It therefore appears most plausible that the ordering reaction occurring during the $\beta \rightarrow \gamma$ transformation limits the growth kinetics.

CHAPTER 7

RESULTS AND DISCUSSION

THE MIGRATION OF THE γ ORDERED/β' ORDERED INTERFACE

7.1 Introduction

Dodecahedron γ precipitates were obtained by the isothermal aging at 350°C of quenched supersaturated β brass. The resulting morphologies corresponded to the equilibrium shapes (Fig. 17) used in the determination of the anisotropy of interfacial energies (Sec. 5.6). A direct transfer of the samples to a salt bath at 400°C caused precipitate growth as illustrated in Fig. 28 .

An extensive investigation of the equilibrium and growth morphologies showed the strong influence of anisotropy of surface energies. In the higher temperature regime reported by D. Robertson (1968) the planar interface readily developed perturbations during growth which would presumably, under a high enough driving force, lead to dendrite formation. At lower temperatures the {110} interface planes corresponding to cusps in the γ-plot were maintained. Surprisingly, as shown in Fig. 28 , the {110} segments exhibited the highest mobility with the edges being effectively pinned. It is proposed that the mechanism of interface migration is responsible for the morphological development during growth.

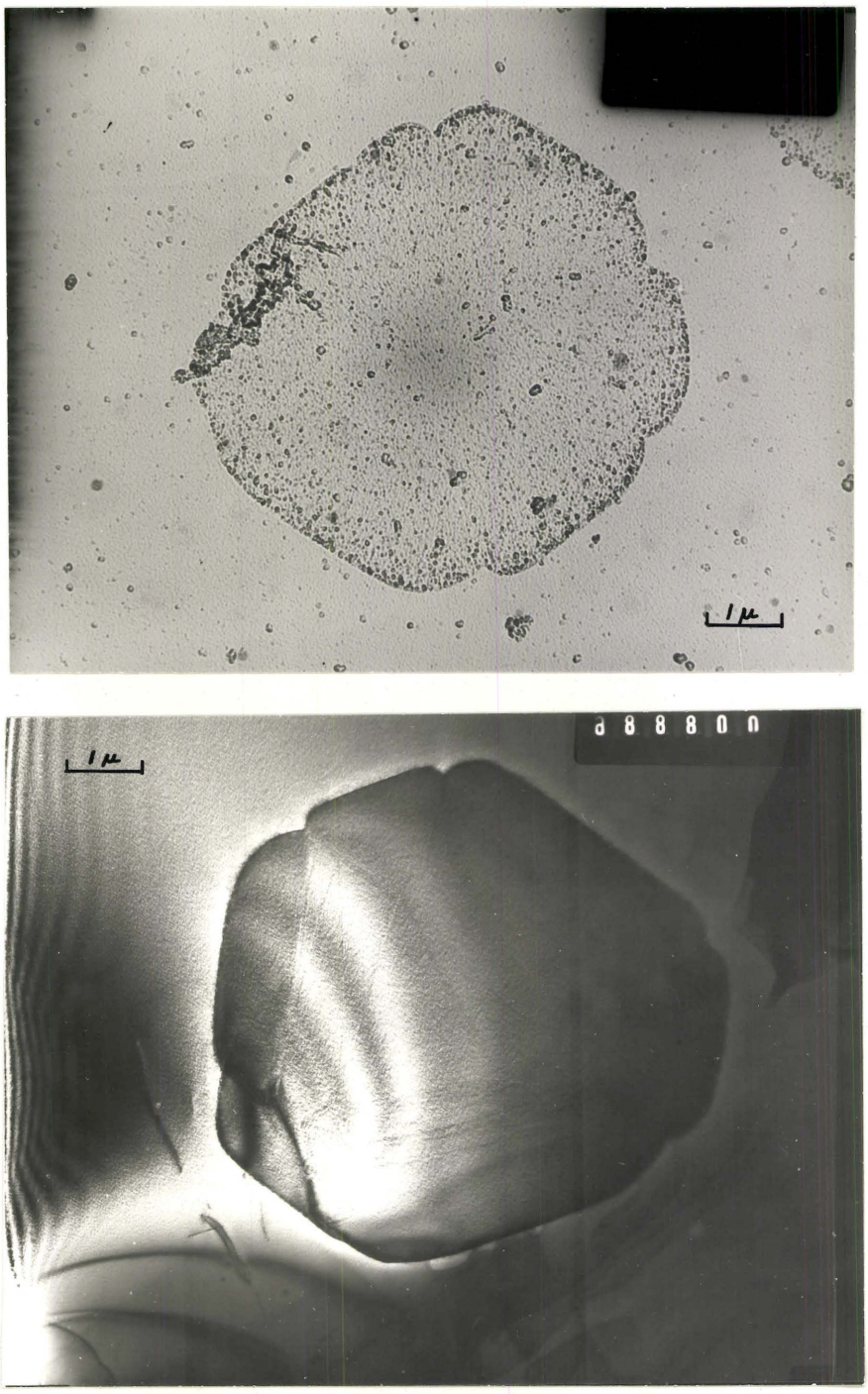

Fig. 28 : Precipitates of γ after a 500 hour isothermal treatment at 350°C to yield the equilibrium polyhedra morphology followed by an upquench to 400°C for 1 hour causing precipitate growth: observed by a) replica and b) thin film transmission electron microscopy.

The two major growth mechanisms suggested by Burton et al (1950) were: a) a surface advances by the lateral motion of steps and b) a surface advances normal to itself without needing steps. Cahn (1960) considered the diffuseness of the interface and the motion resulting from an applied driving force. When a certain critical driving force was exceeded, the surface was able to advance normal to itself without needing steps, otherwise the lateral motion of steps was required for interface migration.

The two growth mechanisms can be inferred directly by observing the antiphase boundaries formed during the precipitation of γ from the β matrix.

7.2 Antiphase Boundaries (A.P.B.) within the γ Precipitates

A metastable three dimensional grid of antiphase boundaries was formed within the γ precipitates on planes defined by the cross product of the dislocation line and climb directions. For the {110} faceted precipitates, the dislocations lie in the <112> and <110> directions within the γ/β interface and climb normal to the interface plane. The antiphase boundaries therefore form a three dimensional network of {111} and {001} planes. Fig. 29 , corresponding to a (110) section, illustrates $(1\bar{1}1)$ and $(\bar{1}11)$ A.P.B.s intersecting the (110) surface along $[\bar{1}12]$ and $[1\bar{1}2]$ directions respectively. The third set along the $[\bar{1}10]$ direction is faintly visible.

Antiphase domain boundaries in the γ lattice arise from stacking faults in the ordered structure. According to the kinematical theory of diffraction contrast (Hirsch, Howie

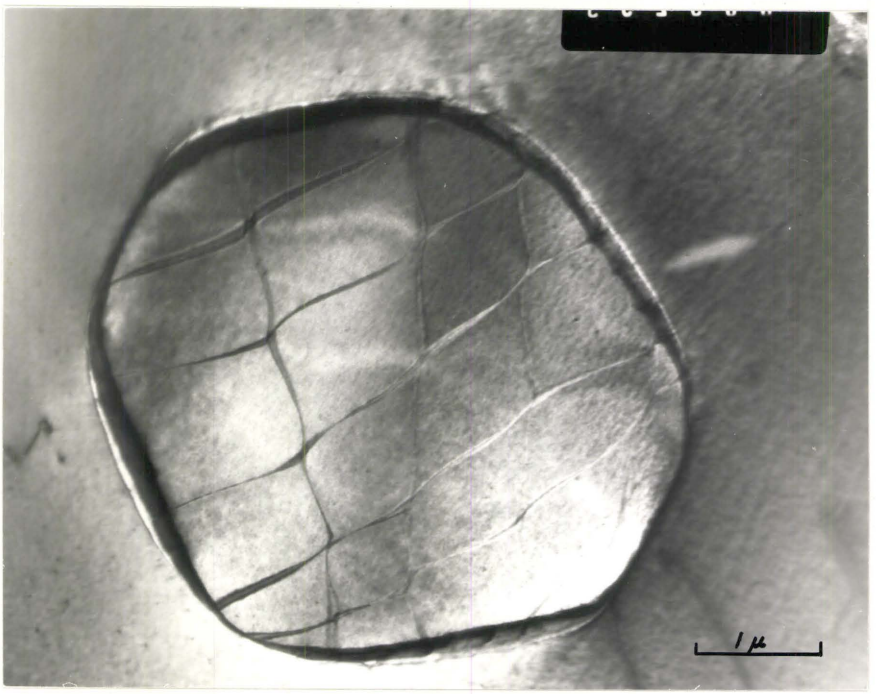

Fig. 29: A metastable configuration of antiphase boundaries (A.P.B.'s) within the γ' precipitates on a {110} section of a sample equilibrated 100 hours at 350°C.

et al, 1963) a beam of electrons crossing a stacking fault experiences a phase shift of:

$$\alpha = 2\pi \vec{g}.\vec{R}$$

where $\vec{g}$ is the [h,k,l] reciprocal lattice vector and $\vec{R}$ is the displacement vector associated with the fault. The fault produces contrast provided the phase shift does not equal $2n\pi$ where n is zero or an integer. Thus an inclined fault produces the characteristic α fringes of spacings proportional to the extinction distance. For lattice reflections having long extinction distances relative to the foil thickness, the contrast arising from the antiphase boundaries could consist of single dark or bright regions depending on the deviation of the crystal from the Bragg diffracting condition. By analysing the contrast behavior of the antiphase domains in dark field, a displacement vector can be determined.

A [331] oriented γ precipitate is presented in Fig. 30. The first micrograph a) using primarily higher order γ lattice reflections in bright field, indicates strong contrast occurring for the A.P.B. array along the $[\bar{1}10]$ direction and weaker contrast for the arrays along the <112> directions; this is opposite to the network shown on a similar {110} plane in Fig. 29. The last two micrographs, using γ lattice reflections in dark field, resolve the internal domain structure. The contrast in b) was observed for $[\bar{1}10]$ and $[\bar{1}03]$ reflections; the contrast in c) occurred with $[\bar{2}20]$ and $[2\bar{1}\bar{3}]$ reflections. The reversal of the contrast signifies a shift in the phase factor α

(a)

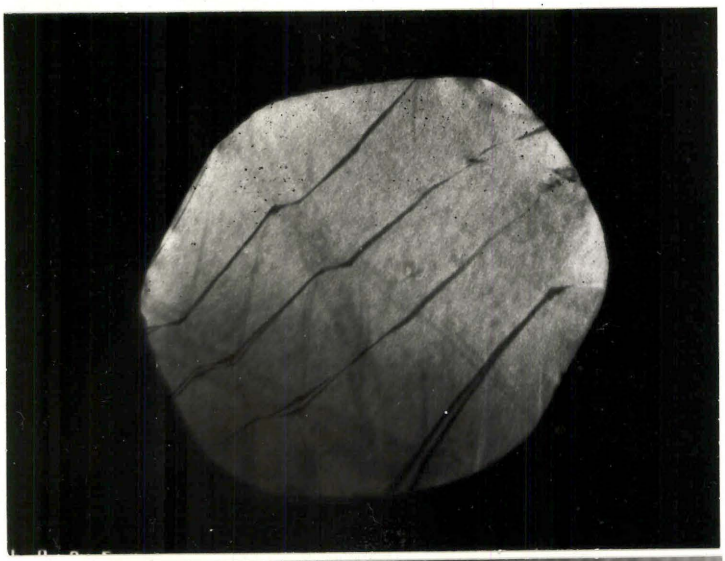

(b)

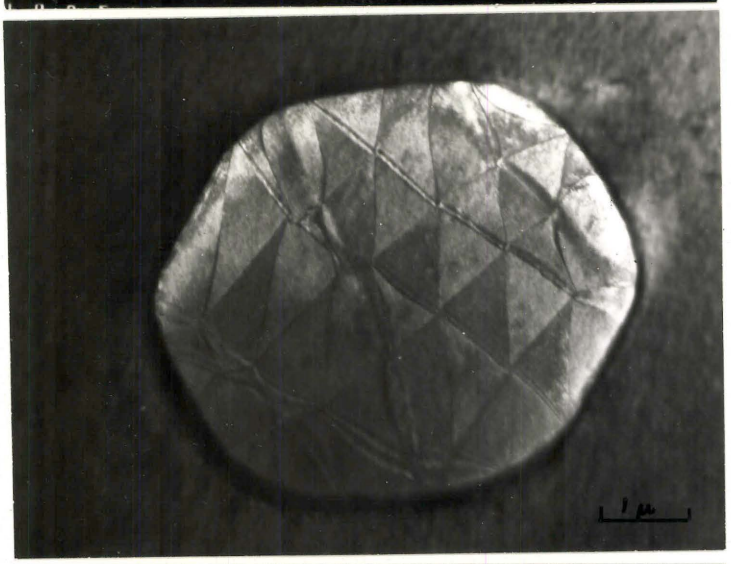

(c)

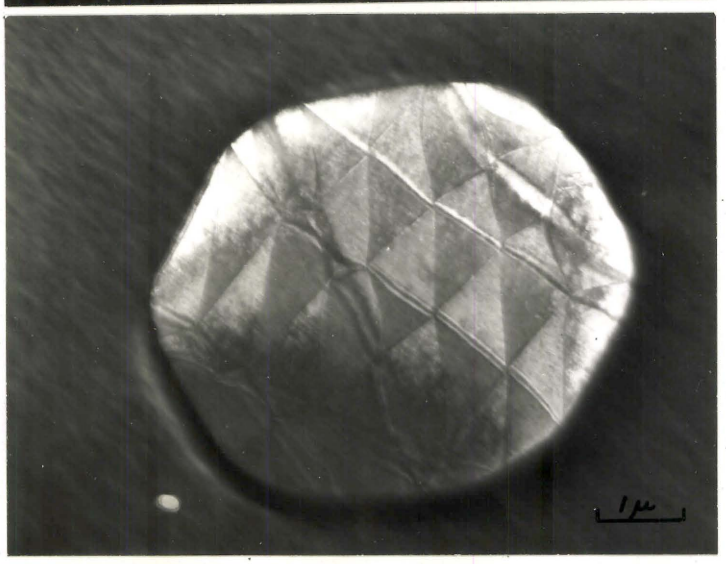

Fig. 30: A.P.B. contrast for a) [000] (bright field) and b) $[1\bar{1}0]$ c) $[2\bar{2}0]$ (dark field) reflections for a (331) section of a γ precipitate.

which is in agreement with a dislocation induced displacement; i.e. $\frac{a}{2}\langle 111\rangle_\beta$ and a $\langle 100\rangle_\beta$.

g	$[\bar{1}10]$	$[10\bar{3}]$	$[\bar{2}20]$	$[2\bar{1}\bar{3}]$
α	$2/3\pi$	$2/3\pi$	0	0

To allow a unique specification of the displacement associated with the antiphase boundary, dark field observations were made for a series of γ lattice reflections for a (110) section. Anomalous behavior was observed in both the pattern, where additional spots relating to the superlattice reflections of the basic body centered sub cell (i.e. for $F_{hkl} = F_{cu} - F_{zn}$) were noted, and in the dark field domain contrast where no unique displacement vector satisfying all the multibeam diffraction conditions was found. Similar effects have been reported by Cupschalk and Brown (1966) who attributed a [112] single contrast phenomena to the strain associated with the difference in atomic spacings across the antiphase boundary being relieved in a single <211> direction. Confirmation of the present contrast reversal experiment should allow clarification in the anomalies in the diffraction contrast behavior.

The observations based on two beam diffraction conditions are all consistent with a displacement vector of $\frac{a}{6}\langle 111\rangle_\gamma$ which is also in agreement with the expectations of the A.P.B. displacement associated with the $\frac{a}{2}\langle 111\rangle_\beta$ misfit dislocations in the ordered γ structure.

The antiphase boundaries within the γ precipitates presumably can arrange into metastable configurations which

prevent annealing out during isothermal equilibration treatments. The formation of the A.P.B.s appears to result from the dislocation climb process accompanying the interphase boundary migration during growth. This is in agreement with observations (i.e. Fig. 7) that the A.P.B.s can terminate at an interface dislocation and exhibit spacings and directions consistent with the plane of dislocation climb.

7.3 Mechanisms and Kinetics of γ/β' Interface Migration

The behavior of the A.P.B.s during the advance of a γ/β' interphase boundary provides a technique useful in determining the growth kinetics of the planar interfaces of the polyhedral shaped γ precipitates and in postulating the mechanism of interface migration occurring with precipitate growth. The present observations suggest that, depending on mode of interface motion, the A.P.B. can either a) be extended parallel to the growth direction as a consequence of dislocation climb or b) form striations perpendicular to the growth direction as a result of the lateral propagation of ledges.

The proposed dependence of the internal faulting on the growth mechanism can be visualized from Fig.31 for a precipitate equilibrated 500 hours at 350°C and upquenched to 400°C for 30 minutes to provide a supersaturation of $\Omega_o = 0.05$ for growth. The isothermal aging at 350°C results in metastable network of A.P.B.s forming and are observed near the centre of the γ precipitate. The dislocation structure within the

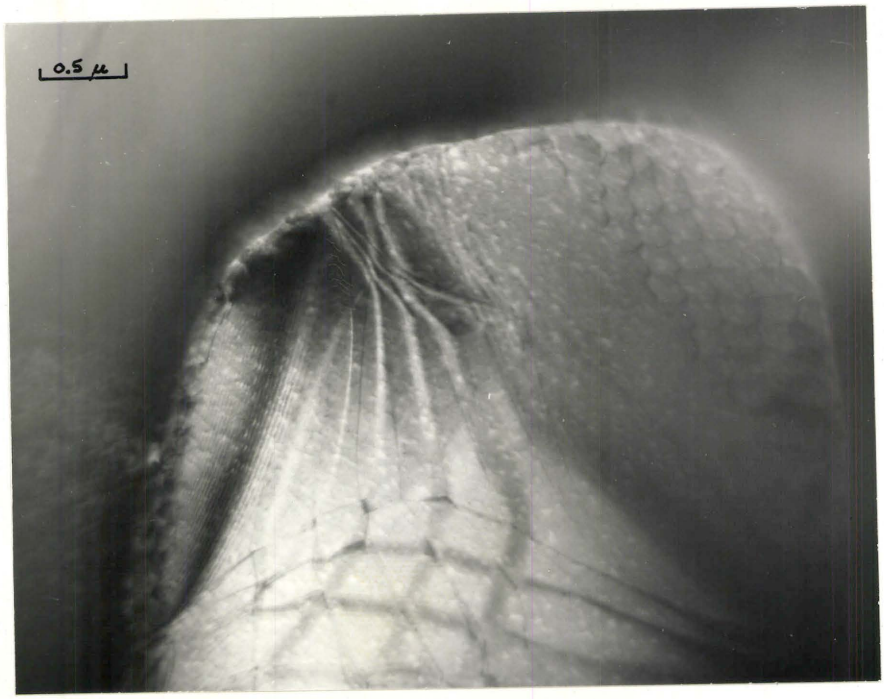

Fig. 31: Transmission electron micrograph of a γ precipitate subjected to a duplex equilibration and growth treatment illustrating an interfacial dislocation network which can either trail an A.P.B. during normal interface advance or form A.P.B. striations during a lateral propagation mechanism.

γ/β' interphase boundary is visible at the upper right. Motion of the dislocations, such as occurs during the migration of the interphase boundary, is expected to result in a plane of displaced atoms which may constitute a fault. Faulting produced by dislocation climb is presumed to be represented by the A.P.B.s terminating at the precipitate corner. The striated region at the left is thought to be a consequence of growth by the lateral propogation of steps. The antiphase boundaries appear to provide a trace of the dislocation motion and thus offer a valuable technique in studying the internal and boundary behavior of the γ precipitates.

A striking confirmation of the two mechanisms is shown in Fig. 32 for a) continuous normal interface propogation and b) advance by the lateral motion of ledges.

For normal motion of an interphase boundary, a certain critical driving force must be exceeded. In Fig. 32 a) a supersaturation of 0.2 for growth was provided by heating a supersaturated β phase alloy to 350°C for a few minutes and quenching. The resulting precipitates showed antiphase boundaries delineating the dislocation climb path. The normal interface migration mechanism would be expected to yield an isotropic interface mobility and the resulting precipitate morphology depends on stability criteria (e.g. Mullins and Sekerka, 1963).

In Fig. 32 b) the γ precipitate was held at 350°C for 500 hours, transferred to 400°C for 50 minutes, then quenched. The supersaturation during the latter growth treat-

(a)

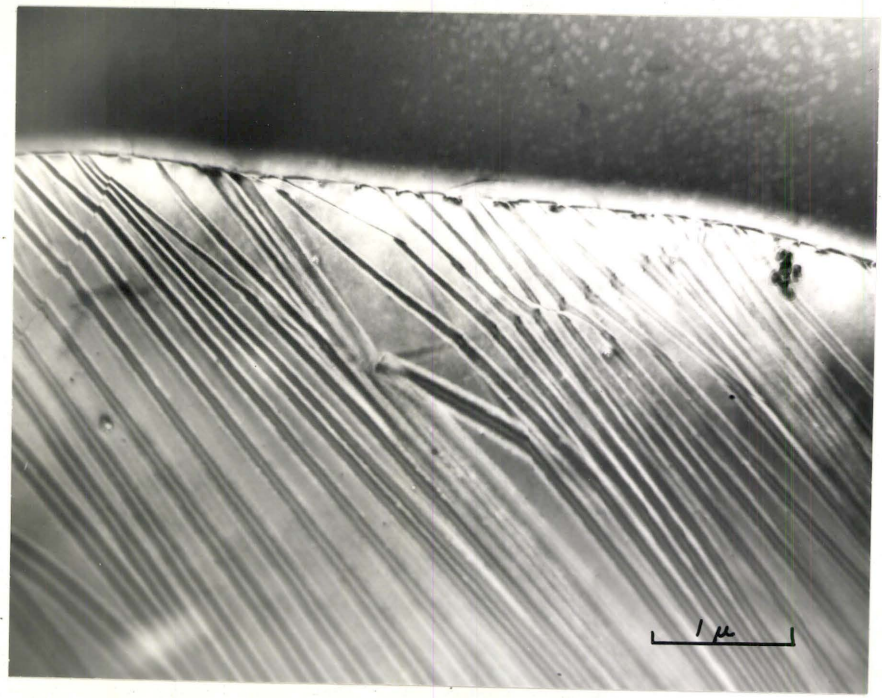

(b)

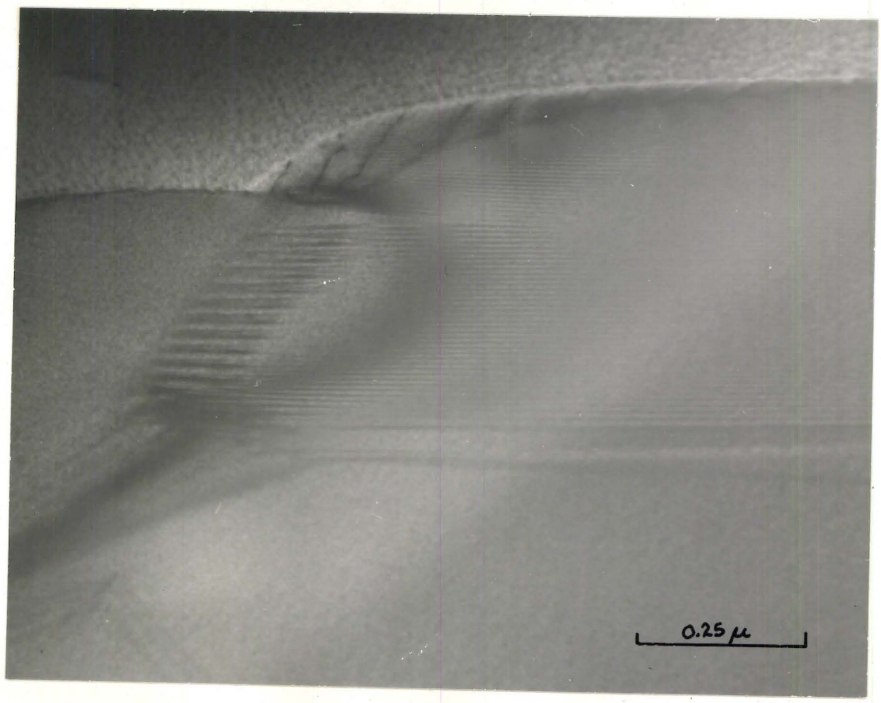

Fig. 32: Mechanisms of precipitate growth inferred by the observed A.P.B.'s: a) normal interface advance and b) the lateral propagation of steps.

ment was 0.05 and the resulting interface advance was, by inference, due to the lateral motion of ledges.

The displacement vector associated with the fault striations is in agreement with the <111> direction describing displacements in the equilibrated A.P.B. networks. The bright and dark field micrographs of Fig. 33 show the equilibrated pennant structure and the subsequent striated growth product. Fig. 33 a) is a (110) section of a precipitate in bright field and b) c) and d) correspond to the section observed with the respective $[002]$, $[\bar{1}10]$ and $[\bar{2}22]$ reflections in dark field. The observed contrast is in agreement with a displacement vector in the $[1\bar{1}1]$ direction. The magnitude of the displacement presumably would allow the excess energy of the fault to be determined, and the structural rearrangements occurring in the γ lattice during ledge migration to be better understood.

The A.P.B. contrast effects can be utilized to determine the migration kinetics of the planar {110} segments of the γ/β' boundary. The width of the growth zone formed by the lateral propogation of ledges was measured for various reaction times and is tabulated in Table 11. The overall rate of boundary migration is expected to depend on both the ledge nucleation kinetics and the subsequent lateral migration. Since the latter involves solute transport, a comparison with volume diffusion controlled interface migration is pertinent. Zener (1949) derived the following expression for planar interface migration:

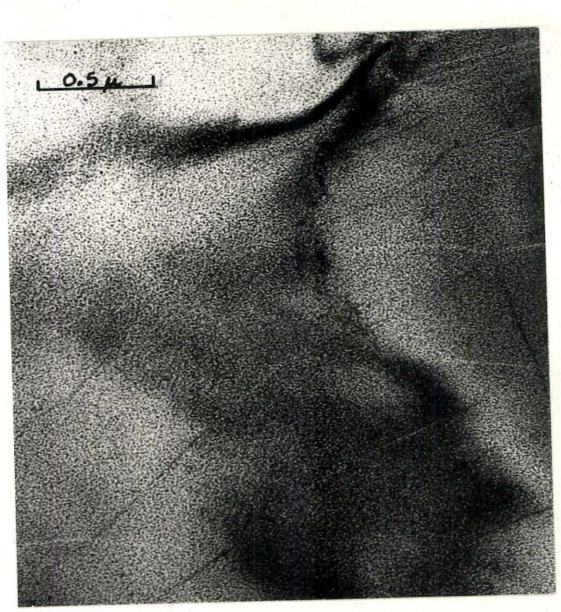

(a)

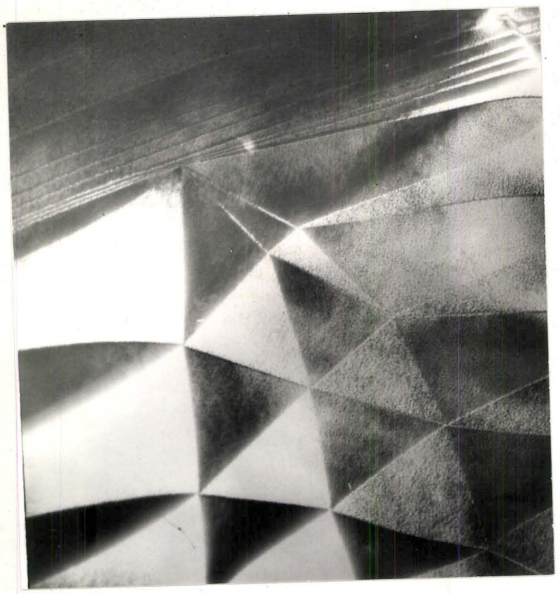

(b)

(c)

(d)

Fig. 33: The equilibrated A.P.B. pennant structure and the subsequent striated growth product of a γ precipitate in a) bright and b), c) d) dark field with $\bar{2}\bar{2}2$, $\bar{1}10$ and $00\bar{2}$ reflections respectively.

TABLE 11: Width of growth zone of polyhedra precipitates equilibrated and upquenched using A.P.B. marker technique

Isothermal reaction time at 400°C (sec)	<110> Interface Migration distances (μm)	Average (μm)
500	--	
900	0.12, 0.15, 0.09, 0.17 0.13, 0.12, 0.10, 0.06	1.2
1800	0.28, 0.30, 0.25, 0.32 0.32, 0.32, 0.25, 0.28	0.28
3600	0.51, 0.52, 0.30, 0.39 0.40, 0.45, 0.47, 0.43	0.43
7200	0.69, 0.68, 0.69, 0.64 0.68, 0.67, 0.62, 0.74	0.68

$$\frac{(x_\beta^{\beta\gamma} - x_\beta)}{(x_\beta^{\beta\gamma} - x_\gamma^{\gamma\beta})} \left(\frac{D^\beta}{\pi}\right)^{\frac{1}{2}} = \frac{\alpha}{2^e}\, \alpha^2/4D \ \operatorname{erfc}\left(\frac{\alpha}{2\sqrt{D}}\right) \tag{7.1}$$

where $\dfrac{x_\beta^{\beta\gamma} - x_\beta}{x_\beta^{\beta\gamma} - x_\gamma^{\gamma\beta}}$ = the dimensionless supersaturation

D = the diffusion coefficient in the β

α = the parabolic rate constant.

By using the linear approximation to the erfc solution a simplified formulation is:

$$V = \frac{D^{\frac{1}{2}}}{2t^{\frac{1}{2}}} \frac{(x_\beta^{\beta\gamma} - x_\beta)}{(x_\beta^{\beta\gamma} - x_\gamma^{\gamma\beta})^{\frac{1}{2}}(x_\beta - x_\gamma^{\gamma\beta})^{\frac{1}{2}}} \tag{7.2}$$

at 400°C. $D = 3.16 \times 10^{-9}$ cm^2/sec,

$x_\beta^{\beta\gamma} = 0.517$

$x_\gamma^{\beta\gamma} = 0.415$

$x_\beta = 0.512$

The distance the interface moved is:

$$y = t^{\frac{1}{2}} D^{\frac{1}{2}} \frac{(x_\beta^{\beta\gamma} - x_\beta)}{(x_\beta^{\beta\gamma} - x_\gamma^{\beta\gamma})^{\frac{1}{2}} (x_\beta - x_\gamma^{\beta\gamma})^{\frac{1}{2}}} \tag{7.3}$$

Impingement of solute fields from adjacent precipitates results in decreasing the effective supersaturation. By considering a solute reflection plane positioned at half the interprecipitate spacing, ℓ, the bulk concentration can be written:

$$x_\beta = x_\beta^{\circ} \quad \text{for } \sqrt{4Dt} < \ell/2 \tag{7.4}$$

$$x_\beta = x_\beta^{\circ} + (x_\beta^{\beta\gamma} - x_\beta^{\circ}) \left(\frac{\sqrt{4Dt}}{\ell/2} - 1\right) \quad \text{for } \ell/2 < \sqrt{4Dt} < \ell \tag{7.5}$$

where x_β^o is the initial bulk concentration and the measured $\frac{\ell}{2} \approx 30$ μm.

The theoretical curve for volume diffusion control in Fig. 34 includes the effect of solute depletion due to impingement. The measured interface migration signified that the boundary was not moving at a rate controlled by the normal diffusion flux. The observed rates corresponded to a linear kinetic coefficient:

$$\mu_o = \frac{V_c}{x_\beta^{\beta\gamma} - x_\beta} \tag{7.6}$$

of $\mu_o = 1.5 \times 10^{-6}$ cm/sec. This compares with $\mu_o = 0.08$ cm/sec for equivalent supersaturations in the dendrite growth measurements. The large difference stems from the different modes of migration. The interface of the γ dendrites advances continuously, the planar interface of the polyhedra advances by the passage of steps. The mode of growth is expected to be a function of the structure of the interface boundary and the anisotropy of interfacial energy.

The different mechanisms of growth also account for the anisotropic interfacial mobility. The normal interface advance, the mobility is nearly isotropic; for the advances by lateral ledge motion, the mobility is anisotropic. The latter condition likely causes the pinning noted at the corners in Fig. 28 during growth.

The anisotropic mobility arises from the characteristics of ledge growth. The mechanism entails both ledge formation and ledge propagation. It is proposed that the ledge nucleation occurs near the center of the {110} planar

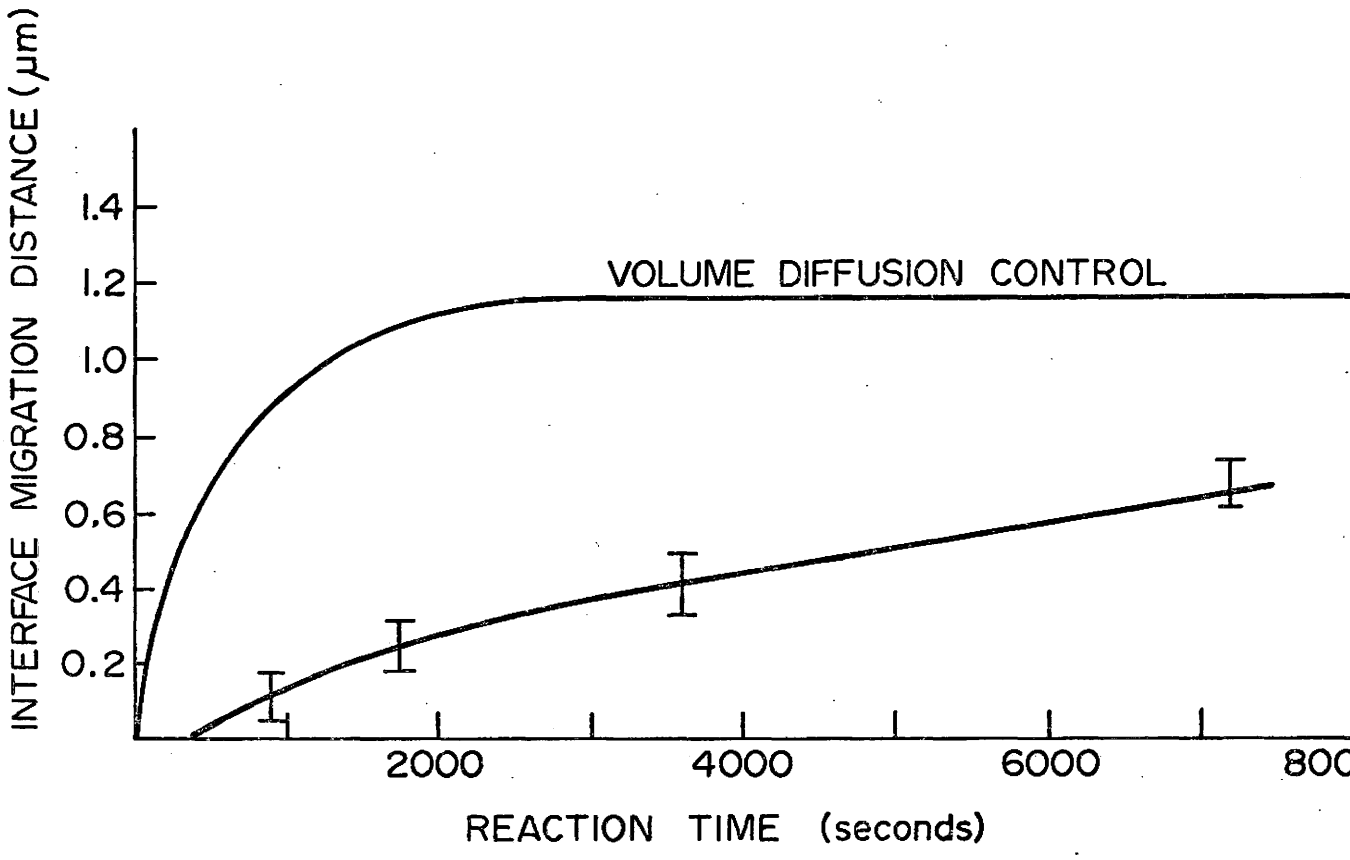

Fig. 34: The migration distance of a planar γ/β' boundary measured by an A.P.B. contrast technique is plotted as a function of reaction time. The kinetics appear consistent with interface advance by the lateral motion of ledges.

interfaces and propagates toward the edges. The nucleation mechanisms used to describe crystal growth from the vapor phase are equally applicable to the present γ/β' coherent interphase boundary. The primary mechanisms are two dimensional nucleation, (Gibbs) and growth by spiral ledges (Burton et al,1950).

Two dimensional nucleation involves formation of the customary pillbox requiring work W:

$$W = S/a\ 2\pi ra + \pi r^2 a(\Delta F_v + \Delta F_{st}) \tag{7.7}$$

which upon differentiation yields a critical radius r_c:

$$r_c = \frac{-S}{a.(\Delta F_v + \Delta F_{st})} \tag{7.8}$$

where S = the edge energy of a pillbox of height, a

$(\Delta F_v + \Delta F_{st})$ = volume free energy and volume strain energy accompanying the formation of the critical nucleus.

When the nucleation step is rate controlling the overall growth rate is proportional to the rate of nucleation of critical nuclei per unit area of the boundary. A review by Russell (1970) treats the rate of formation of boundary nuclei. In the present case, the constant height of the ledges and the existence of a fault structure indicate the likelihood of a regenerative spiral process rather than the repeated nucleation mechanism. The large step height, ($a=50\mathring{A}$), appears in accord with $a > r_c$ required for plate growth.

The spiral growth mechanism is observed on the {110} faces of γ precipitates during electrolytic dissolution as indicated in fig. 35 a). It is possible that a similar

(a)

(b)

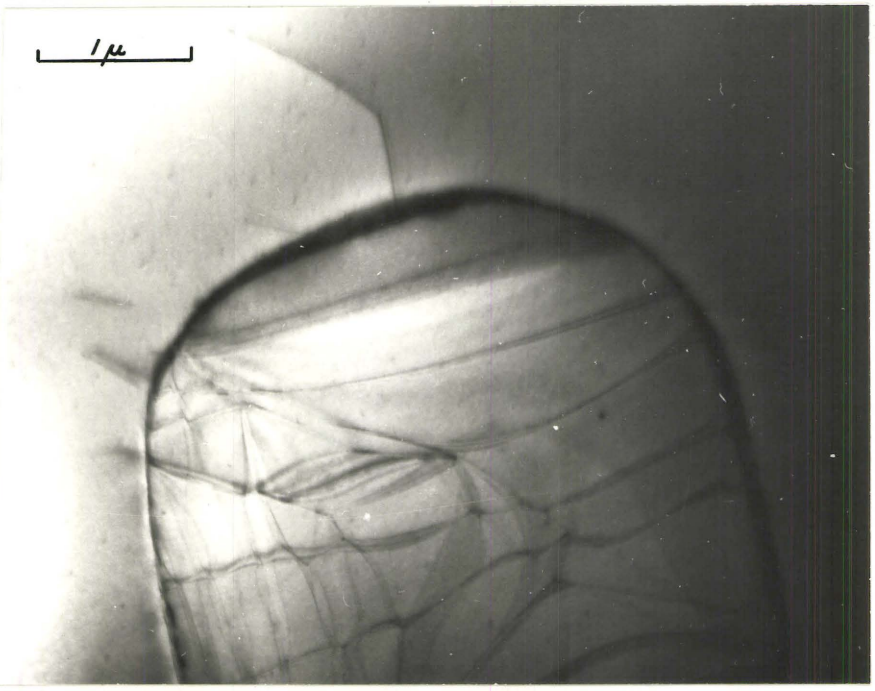

Fig. 35: a) Replica transmission electron micrographs illustrating the electrolytic dissolution of a faceted γ precipitate by a spiral growth mechanism.

b) It appears a similar spiral mechanism of a pole dislocation may occur during growth. Samples equilibrated at 350°C and upquenched to 400°C for 60 minutes.

mechanism could occur during the growth of γ precipitates at low supersaturations. With the aid of a pole dislocation, possibly as seen in Fig. 35 b), the spiral growth mechanism would yield an interface advance rate (Burton et al, 1950):

$$V = \frac{\omega a}{2\pi} \tag{7.9}$$

where ω = angular velocity of the spiral

$$\omega = \frac{v}{r_c} \tag{7.10}$$

for a critical radius, r_c, of a pillbox shaped nucleus of height a, with a linear step velocity v.

The latest refinement in the description of the linear ledge velocity is by Jones and Trivedi who found the diffusional solution could be represented by:

$$v = \frac{2D\ (x_\beta - x_\beta^{\beta\gamma})}{3a\ (x_\gamma^{\gamma\beta} - x_\beta^{\beta\gamma})} \tag{7.11}$$

Substituting $D = 3.16 \times 10^{-9}$ cm^2/sec

$a = 50 \times 10^{-8}$ cm

$\Omega_o = 0.05$

$r_c = 8 \times 10^{-5}$ cm

The ledge propagation rate is 2×10^{-4} cm/sec yielding an interface migration velocity for the spiral growth mechanism of $\sim 10^{-3}$ μm/sec. The measured growth rates were an order of magnitude less. The kinetic measurements were based on the widening rates of the growth zones produced by a lateral ledge mechanism and exhibited an incubation

period of approximately 500 seconds. Two possibilities exist for the overall precipitate growth:

a) that the initial growth occurred by the continuous normal advance of the boundary until the concentration gradient decreased sufficiently to cause the transition in modes of interface propagation (Cahn, 1960). The ledge motion occurring at later times would have a slower velocity due to the decreased supersaturation. The alternative is:

b) since the Burgers vectors of the misfit dislocations are parallel to the {110} interphase boundaries, the misfit dislocations do not contribute to the nucleation of steps. The additional nucleation step will require finite incubation times either in developing a critical nucleus on the surface or in adsorbing a structural defect to the surface (i.e. pole dislocation).

The ledge propagation rate appears to offer an explanation for the lower mobility or pinning of the corners of the γ precipitates. The lateral velocity of a ledge is inversely proportional to the ledge height. As the initial ledge approaches a rounded corner, the requirement to remain in the low energy {110} cusp-orientation dictates the ledge height and decreases the velocity. A second effect of the increased ledge height is the added accumulation of lattice strain; the height dependence parallels the epitaxial overgrowth relations suggested by Van der Merwe (1963). The sum of the effects retard the ledge velocity as the corners are reached. A net repulsion between the

ledges would result in some metastable stacking of subsequent ledges and give rise to the observed anisotropic interface mobility. The low mobility "pinned" corners grow out after ~24 hours at 400°C and the precipitate morphology is again determined by the anisotropy of interfacial free energy.

CONCLUSIONS

1. The interface disregistry caused by the difference in lattice parameters between the β brass matrix and the mutually oriented γ precipitates is accommodated by a misfit dislocation network of Burger's vector $\frac{a}{2}$ <111> and a subsequent reaction product of a<100>.

2. The energy of the γ/β interphase boundary is considered to be the sum of two independent terms; a structural contribution due to the misfit dislocation network at the interface and, a chemical contribution due to an excess energy associated with the atomic bonding across the interface. At temperatures above the ordering temperature, the structural term predominates; an anisotropic contribution arises from the varying amounts of misfit accommodation possible with four $\frac{a}{2}$ <111> dislocation arrays. At temperatures below the ordering temperature, the increase in the chemical contribution is a function of the long range order parameter. The resulting theoretical description of the boundary is in agreement with following experimentally determined interface properties.

   a) the magnitude of the γ/β surface energy
   b) the orientation dependence of the γ/β and γ/β' surface energies

c) the temperature dependence of the anisotropy of the surface energies.

3. By comparing the symmetric isothermal (520°C) precipitation reactions, of α rods and γ dendrites from a similar disordered β matrix, the uncertainty in the values of the growth parameters is eliminated. The results of the kinetic measurements indicate the α rods grow at a rate consistent with a volume diffusion control model and the γ dendrites lengthen at a rate significantly slower than limited by diffusion in the matrix. A linear kinetic coefficient of 0.08 provides agreement with the measurements; this is tentatively attributed to the ordering reaction accompanying the $\beta \rightarrow \gamma$ phase transformation.

4. During interface migration within the ordered regime, the mechanism of interface advance depends on the supersaturation. At low supersaturations, a lateral ledge mechanism is proposed in accord with the observed fault striations parallel to the γ/β interface. These are presumably formed by the displacement accompanying the lateral propagation of the ledges. At higher supersaturations, normal interface advance requires the climb of the interfacial dislocation and results in the formation of an A.P.B. delineating the climb path. The proposed mechanisms are consistent with the measured interface migration kinetics and the observed growth morphologies.

APPENDIX I

The procedure for obtaining selected area diffraction patterns for various camera constants is not well outlined in the instruction manual; a brief description of the procedure follows. Select the region of interest and insert and centre the selected area aperture With the mode switch in SA position, accurately focus the specimen (with objective lens potentiometer) and the aperture (with selected area potentiometer). Switch to mode D+1 and remove the objective aperature to obtain the pattern. This diffraction pattern may now be viewed while using three different sets of operating conditions, as was illustrated in Fig. 5. Basically, the diffraction lens is used for focussing the pattern and the intermediate lens is used for changing the camera constant (or pattern magnification); thus both lens currents will vary.

The potentiometers of both lenses have a stepwise variable coarse control and an infinitely variable fine control. Calibrations are restricted to each step on the course potentiometer of the intermediate lens, with the fine control preset either in the minimum or maximum positions. Both course and fine potentiometers of the diffraction lens are employed in focussing.

A fixed pattern is obtained with the intermediate lens off and gives the best conditions when the electron optics are misaligned (Feltner and Sefton). Ranges 1 and 2 (course I.L. potentiometer) reduce this pattern while Ranges > 4 give the complete range of possible pattern sizes. The latter range offers the greatest versatility and the normal patterns are taken at 4, the maximum position.

The magnifications are tabulated (Table 12) and plotted (Fig. 36) for both M and SA. operational modes. It is important when using SA always to have the specimen and selected area aperture simultaneously focussed for each position of the magnification switch.

The different pattern magnifications or camera constants were measured by Eyre using gold foils and are included here for completeness (Fig. 37).

Relative rotations with respect to actual specimen placement are measured in Table 13. This includes both images and diffraction patterns, with measurements being in a clockwise direction as viewed on the screen. Making prints involves either reversing the negative during printing or measuring these angles in an anticlockwise direction. A simple subtraction gives the rotation between any two conditions; for example, image to diffraction pattern relation.

In Fig. 38 a polar plot of directions with reference to the specimen tilt axis is given. This corresponds to Eyre's object to image relations but provides a more convenient representation of the rotations for all normal operating conditions. Curves can be constructed for each specific

rotation used; for example, see Fig. 39.

In most quantitative work requiring definite diffraction contrast conditions, the specimen must be tilted or rotated to certain pre-determined orientation. In-situ analyses of the diffraction pattern and knowledge of the tilt axis on the diffraction pattern allow navigation in reciprocal space. The tilt directions, perpendicular to the tilt axis, give the direction on the pattern of the trace of an upward normal to the surface plane during a clockwise specimen tilt. Fig. 40 indicates the tilt directions for various methods of obtaining the diffraction pattern and therefore gives the necessary alignment of the diffraction pattern for specific orientation requirements.

TABLE 12: Magnifications for M and SA modes (Goniometer stage at 100 KV)

Position	M	SA
2	1500	11,600
4	2200	11,600
6	3250	11,600
8	5000	11,600
10	7900	11,600
11	10,600	9,200
12	13,500	11,000
13	17,100	13,500
14	21,400	16,300
15	27,200	18,500
16	34,400	23,000
17	43,200	27,800
18	53,000	34,700
19	65,300	42,000
20	79,300	50,000
21	100,000	62,500
22	127,000	75,000
23	157,000	
24	194,000	112,000

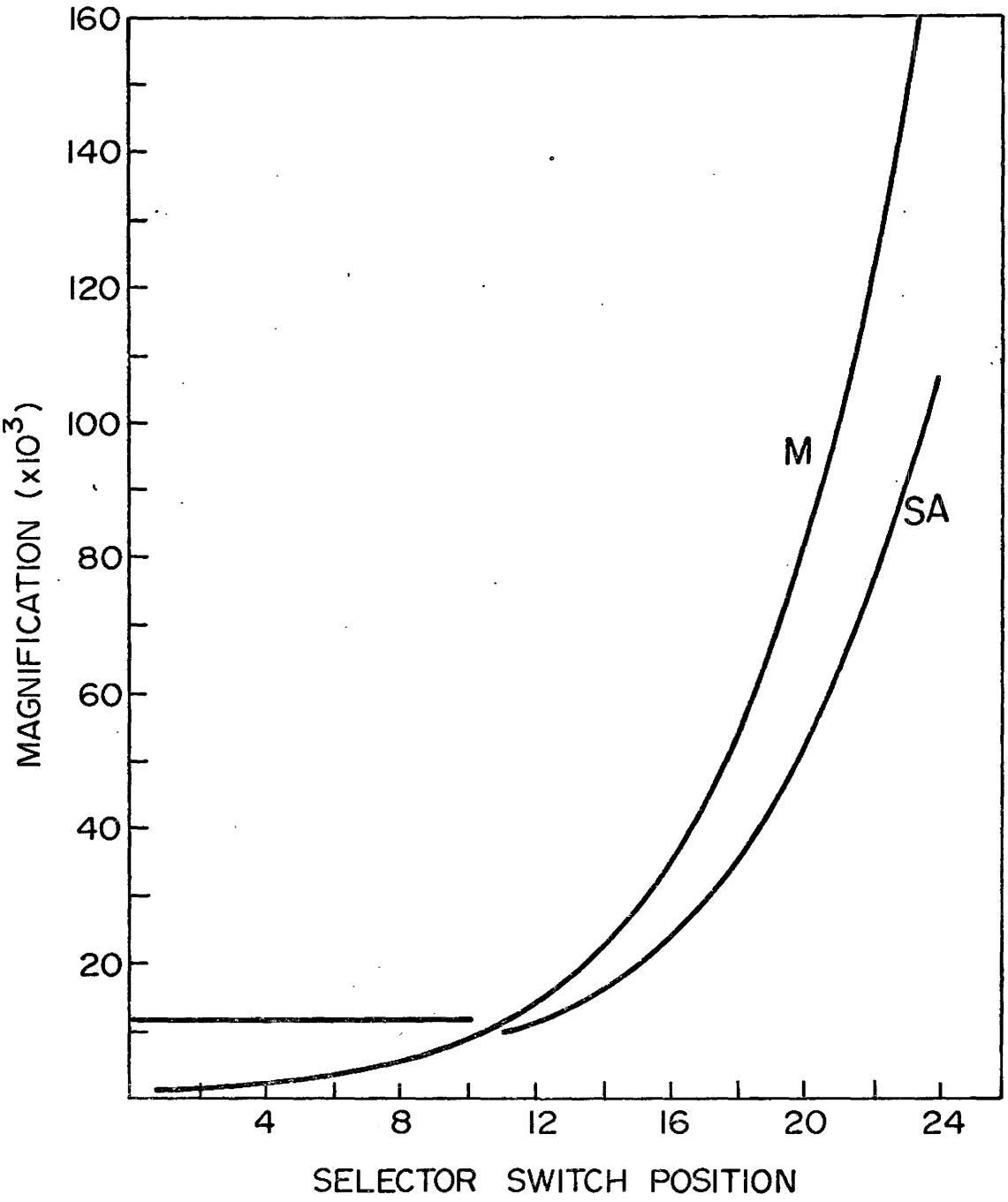

Fig. 36: Magnification as a function of selector switch position for the ranges "M" and "SA" of the Phillips EM 300

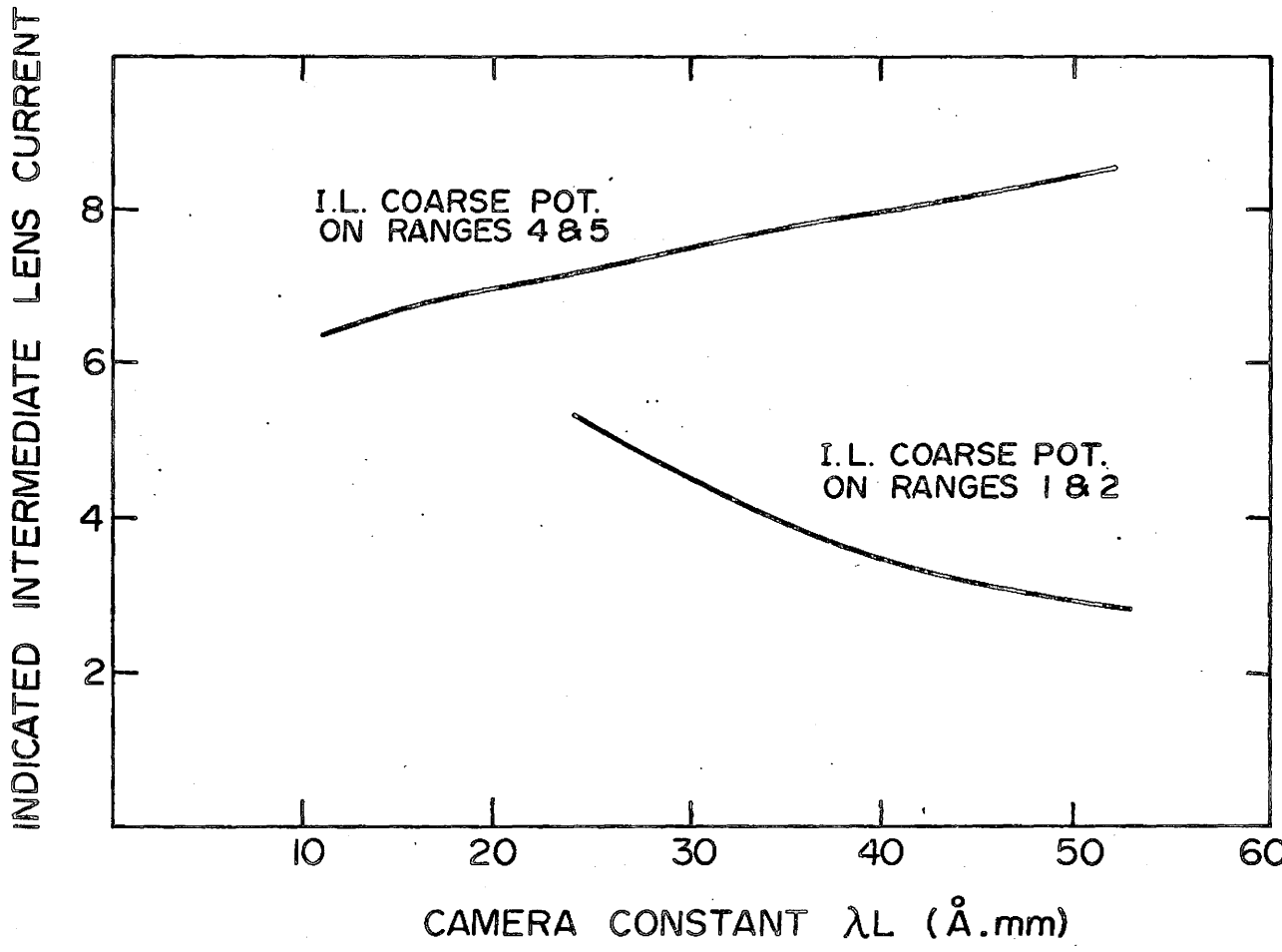

Fig. 37: Variation in Camera constant with indicated intermediate lens current (Eyre)

TABLE 13: Rotations: Measured with respect to Object
(a) Clockwise as viewed on screen
(b) Counterclockwise on prints

Image Rotations				Diffraction pattern Rotations	
M 2	83°	SA 2	276°	Int. Lens Off	70°
M 3	80°	SA 3	276°	1,0	79°
M 4	75°	SA 4	276°	2,0	78°
M 5	72°	SA 5	276°	3,0	64°
M 6	67°	SA 6	276°		
M 7	63°	SA 7	276°	4,0	319°
M 8	58°	SA 8	276°	5,0	307°
M 9	47°	SA 9	276°	6,0	306°
M 10	36°	SA 10	276°		
				4,max	309°
M 11	156°	SA 11	151°	5,max	306°
M 12	157°	SA 12	151°	6,max	305°
M 13	159°	SA 13	152°		
M 14	162°	SA 14	153°		
M 15	165°	SA 15	155°		
M 16	169°	SA 16	158°		
M 17	172°	SA 17	161°		
M 18	178°	SA 18	166°		
M 19	182°	SA 19	171°		
M 20	188°	SA 20	174°		
M 21	194°	SA 21	180°		
M 22	206°	SA 22	189°		
M 23	217°	SA 23	202°		
M 24	234°	SA 24	217°		

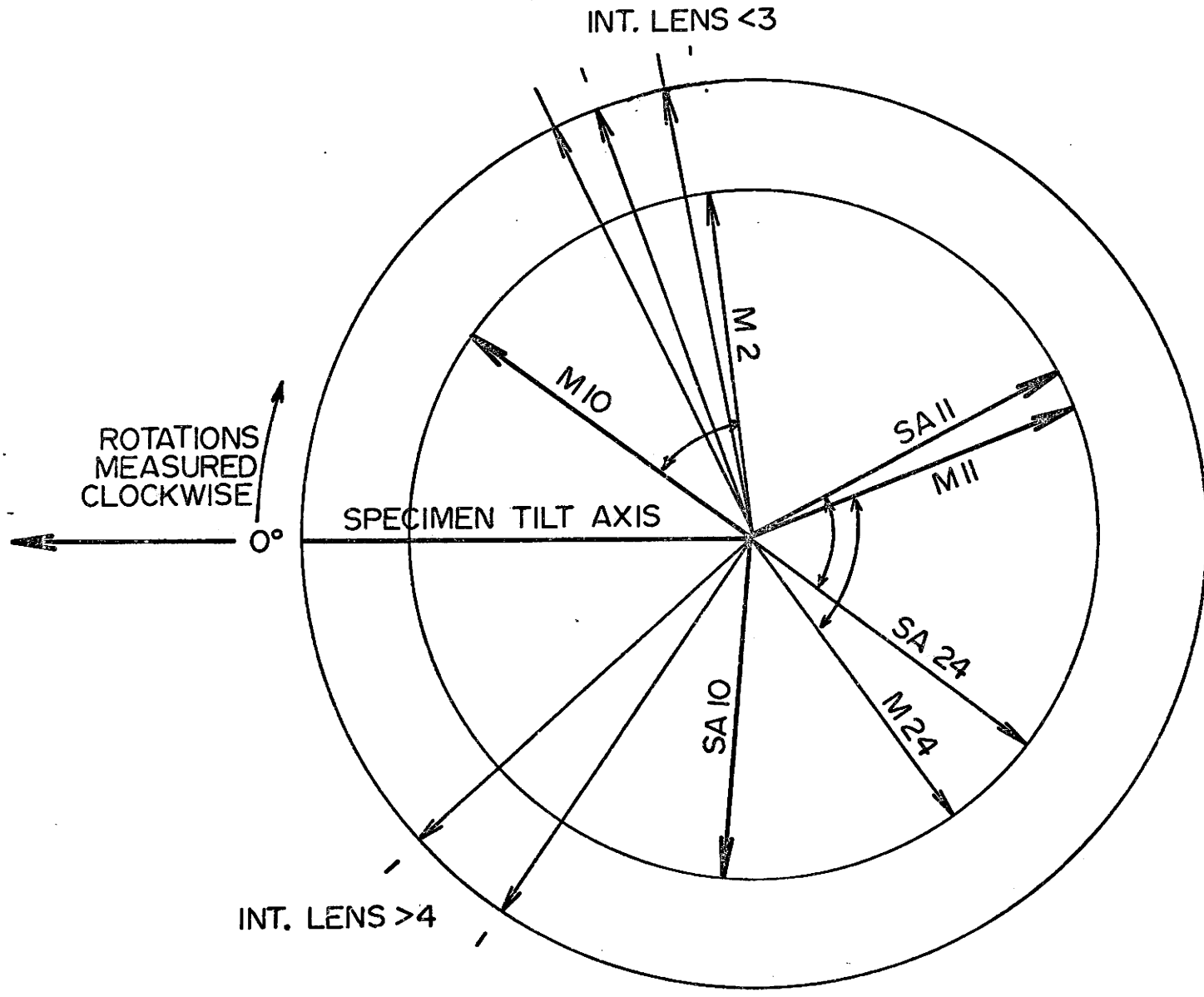

Fig. 38: A polar representation of the rotations of the image and diffraction patterns for the designated settings referenced to the specimen tilt axis.

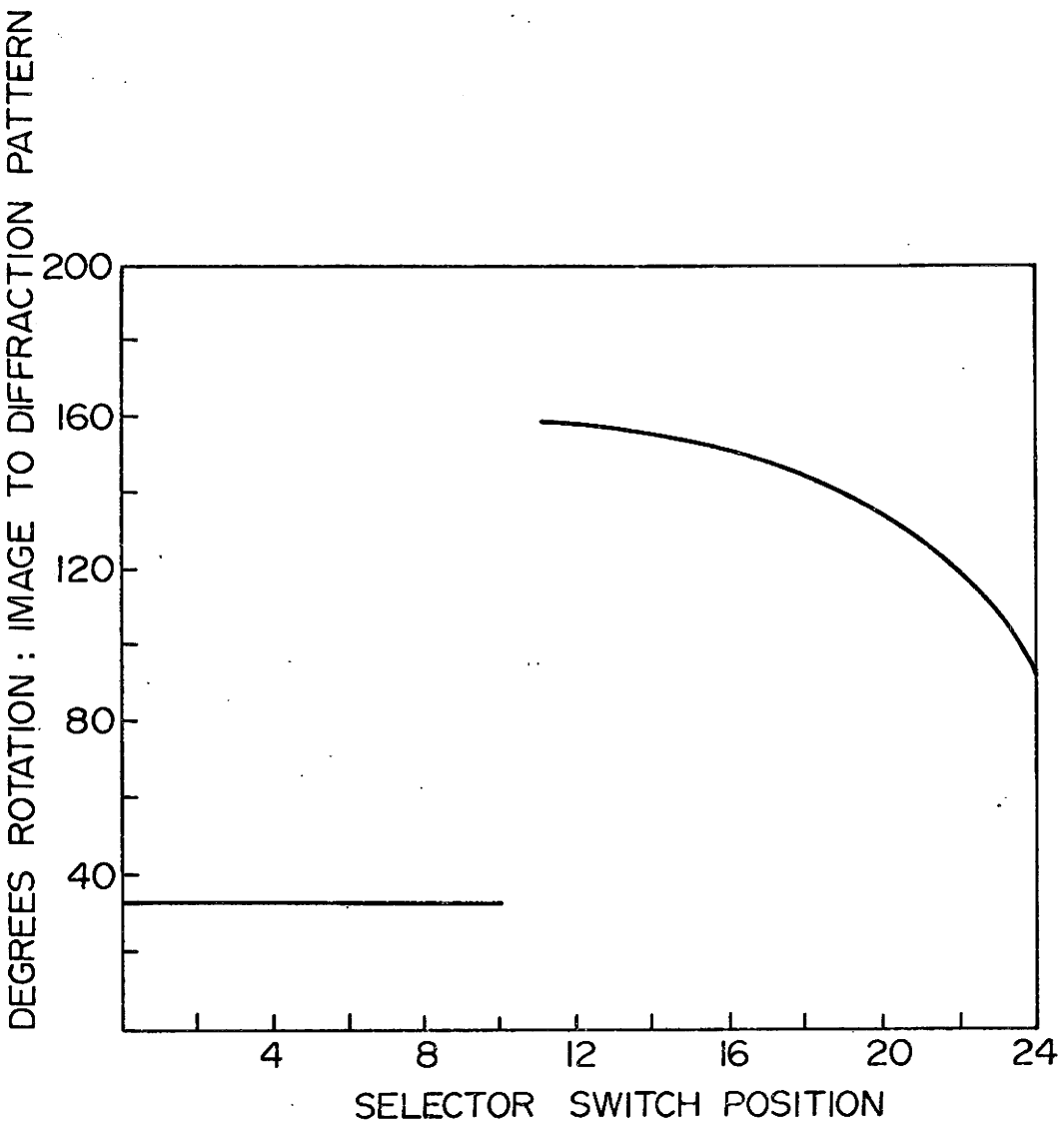

Fig. 39: Relative rotations between the S.A. image and the diffraction pattern for an intermediate lens setting of 4 : max. on the respective coarse: fine potentiometer

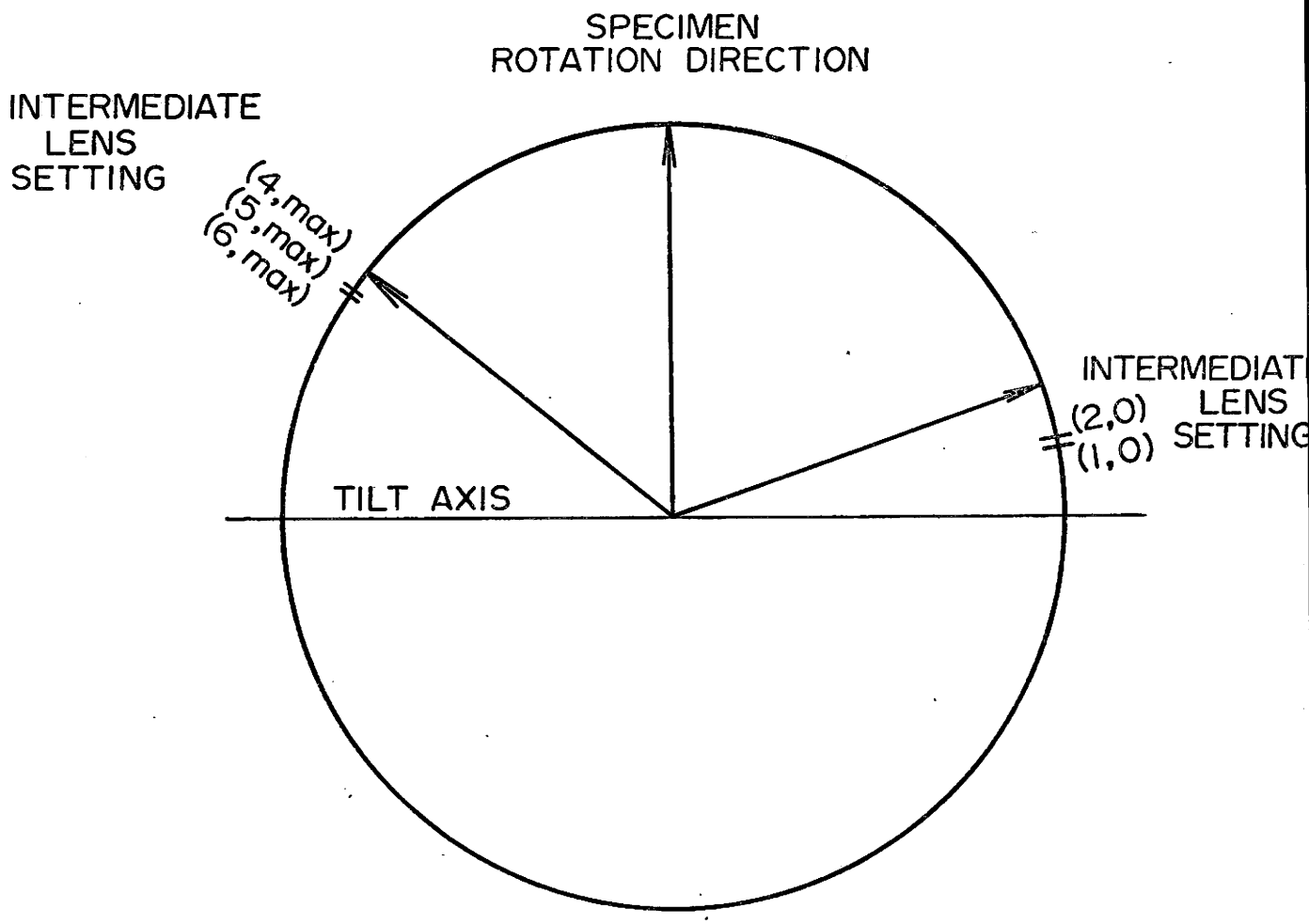

Fig. 40: The trace of the specimen tilt axis and rotation direction on the diffraction pattern when observed on the screen of the Phillips EM 300.

REFERENCES

Aaronson, H. I., Laird, C., Acta Met. 15, 73 (1967)

Aaronson, H. I., Laird, C., T. AIME 242, 1437 (1968)

Aaronson, H. I., Clark, J. B., Laird, C., Met. Science JRL 2, 155 (1968)

Aaronson, H. I.,Laird,C.,Kinsman,K.R.,"Phase Transformations" American Society for Metals,(1970)

Aaronson, H. I., "The Mechanism of Phase Transformations in Crystalline Solids" Ins. of Met. Mon. 33 Inst. of Met. London (1969).

Ashby, M. F., Johnson, L., Phil. Mag. 20, 1009 (1969)

Ashby, M. F., Gelles, S. H. Tanner, L. E., Phil. Mag. 19, 757 (1969).

Bainbridge, B. G., Doherty, R. D., "Proc. Haifa Conference on Phase Transformations" (1970).

Balluffi, R. W., Seigle, L. I., Acta Met. 3, 170 (1955)

Barnes, R. S., J. Nucl. Mat. 11, 135 (1964)

Basterfield, J., Miller, W. A., Weatherly, G. C., Can . Met. Quart. 8 131 (1970)

Bevis, M., Swindells, N., Phys. Stat.Sol. 20, 197 (1967)

Bolling, G. F., Tiller, W. A., J. Appl. Phys. 32, 2587 (1961)

Bradley, A. J., Gregory, C. H., Phil. Mag. 12, 143 (1931)

Brandon, D. G., Acta Met. 14, 1479 (1966).

Brooks, H., "Metal Interfaces" ASM (1952)

Brown, N., Acta Met. 7, 210 (1959)

Brown, N., Lenton, D. R., Acta Met. 17, 669 (1969)

Brown, L. M., Woolhouse, G. R., Phil. Mag. 21, 329 (1970)

Burton, W. K., Cabrera, N., Frank, F. C., Phil. Trans. A243 299 (1950)

Cahn, J. W., Hilliard, J. E., J. Chem. Phys. 28, 258 (1959).

Cahn, J. W., Acta Met. 8, 554 (1960); 8, 681 (1960).

Cahn, J. W., Acta Met. 9, 795 (1961)

Cahn, J. W., Acta Met. 10, 907 (1962)

Cahn, J. W., "The Mechanism of phase transformations in Crystalline Solids", Inst. of Met. Mon. 33, Inst. of Met. London (1969).

Cahn, J. W., Hillig, W. B., Sears, G. W., Acta Met. 12, 1421 (1964).

Callen, H. B., "Thermodynamics", p. 231, Wiley (1966).

Chalmers, B., Rutter, J. W., Can. J. Phys. 31, 15 (1953)

Clarebrough, E. M., Acta Met. 5, 413 (1957)

Cline, H. E., Walter, J. L., Koch, E. F., Osika, L. M., Acta Met. 19, 405 (1971)

Cook, H. E., Hilliard, J. E., J. Appl. Phys. 40, 2191 (1969)

Corrie, J. A., M.S. Thesis, University of Pennsylvania (1958)

Crawford, R. C., Miller, D. R., Phil. Mag. 14, 1071 (1964)

Crombie, R., Downie, D. B., Acta Met. 19, 1227 (1971)

Cupschalk, S. G., Brown, N., Acta Met. 16, 657 (1968)

Cupschalk, S. G., Brown, N., Acta Met. 15, 847 (1967)

Cupschalk, S. G., Brown, N., Phil. Mag. 14, 1077 (1966)

Darken, L. S., Trans AIME 175, 184 (1948)

Drechsler, M., Nichols, J. F., J. Phys. Chem. Solids 28, 2609 (1967)

Elliott, R. P., "Constitution of Binary Alloys", 1st suppl., McGraw Hill, N.Y. (1965).

Eyre, B. L., Harwell Atomic Energy Report R6525 (1970)

Farrell, K., Loh, B.T.M., Stiegler, J.O., Trans. ASM 60, 485 (1967)

Feltner, C.E., Sefton, L.R., Phillips Bulletin (1966)

Fletcher, N.H., "Interfaces" Proceedings of Int. Conf. Melbourne 1969, Butterworths (1965)

Foreman, A.J.E., Acta Met. 3, 322 (1955)

Frank, F. C., Symposium on Plastic Deformation of Crystalline Solids, Carnegie Inst. of Tech. 150 (1950)

Gibbs, J. W., "Collected Works", Longmans, Green & Co., London, 1928 p. 325

Hansen, M., "Constitution of Binary Alloys", McGraw Hill (1958)

Hawbolt, B., University of British Columbia, unpublished research (1971)

Head, A.K., Loretto, M.H., Humble, P., Phys. Stat. Sol. 20, 505 (1967)

Heidenstam, O.V., Johansson, A., Westman, V.S., Acta Chem. Scand. 22, 653 (1968)

Herring, C., Phys. Rev. B2, 87 (1951)

Hillert, M., Jernkont. Ann. 141, 756 (1957)

Hillert, M., "The Mechanism of Phase Transformations in Crystalline Solids" Inst. of Metals Mon 33, Inst. of Metals, London (1969)

Hirth J.P., Lothe J., J. Appl. Phys. 38, 845 (1967)

Holzman, E.G., J. Appl. Phys. 41, 1460 (1970); 41, 4769 (1970)

Hondros, E.D., "Interfaces" Proceedings of Int. Conf. Melbourne Aug. 1969, Butterworths, 1969

Hone, M. R., Ph.D. Thesis, McMaster University,(1970)

Horvay, G., Cahn, J. W., Acta Met. 9, 695 (1961)

Hultgren, R.A., Orr, R.L., Anderson, P.D., Kelley, K.K., "Selected Values of Thermodynamic Properties of Metals & Alloys" Wiley (1963)

Ishida Y., Hasegawa, T., Nagata, F., J. Appl. Phys.40, 2182 (1968)

Ivantsov, G. P., Dokl. Akad. Nauk. SSSR, 58, 567 (1947)

Johansson, A., Ljung, H., Westman, V.S., Acta Chem. Scand. 22, 2743 (1968)

Jolley, W., Hull D., J.I.M. 92, 129 (1964).

Jones, G. V., Trivedi, R., ref. 104 in Aaronson et al. "Phase Transformations" ASM (1970)

Kinsman, K. R., Aaronson, H.I., "Theory of Microstructure" from Seminar in Sept. 1971, I.M.S., Denver (1972).

Kinsman, K. R., Aaronson, H.I., Laird, C., Acta Met. 15, 1244 (1967)

Kirchner, H.O.K., Chadwick, G.A., Phil. Mag. 20, 405 (1969)

Kotler, G.R., Tarshis, L.A., J. Cryst. Growth 5, 90 (1969).

Landau , L.D., and Lifshitz, E.M., "Statistical Physics", Addison Wesley, Mass. 1958, p. 368

Laird, C., Aaronson, H.I., Trans. AIME 242, 1393 (1968)

Laird, C., Aaronson, H.I., Acta Met. 15, 73 (1967)

Landergren, V.S., Birchenall, C.E., Mehl, R. F., J. of Met. 73 (1956)

Lonsdale, K., Phil. Trans. Roy. Soc. 240, 219 (1947)

Mackenzie, J.K., Moore, A.J.W., Nicholas, J.F., J. Phys. Chem. Solids 23, 185 (1962)

Malcolm, J.A., Purdy, G.R., T.A.I.M.E. 239, 1391 (1967).

Marcinkowski, M.J., Thomas, G., and Washburn, J., "Electron Microscopy & Strength of Crystals" Interscience, N.Y., p. 333 (1963)

Massalski, T.B., Kittl, J.E., J. Aust. Inst. of Metals, 8, 91 (1963)

McLean, M., Acta Met. 19, 387 (1971)

McManus, G.M., Phys. Rev. 129, 2004 (1963)

Mehl, R.F., Marzke, O.T., Trans. AIME 93, 123 (1931)

Mehl, R.F., Lutz, C.F., Trans. AIME, 221, 561 (1961)

Kasymbekova, K.K., Polyakova T.P., Presnyakov, A.A., Phys. Met. Metalog. USSR 16, 54 (1963)

Miller, W.A., Chadwick, G.A., in "The Solidification of Metals" p.49 ISI pub. 110, 1968

Miller, W.A., Carpenter, G.J.C, Chadwick, G.A., Phil. Mag. 19, 305 (1969).

Moore, E.M., Scripta Met. 2, 491 (1968)

Morris, W.G., J. Appl. Phys. 39, 1813 (1968)

Morton, A.J., Head, A.K., Phys. Stat. Sol. 37, 317 (1970)

Morton, A.J., Phil. Mag. 22, 483 (1970)

Mullins, W.W., Sekerka, R.F., J. Appl. Phys. 34, 323 (1963)

Mullins, W.W., Sekerka, R.F., J. Appl. Phys. 35, 444 (1964)

Nelson, R.S., Mazey , D.J., Barnes, R.S., Phil. Mag. 11, 91 (1965)

Nicholson, R.B., "Interfaces" Proceedings Int. Conf. Melbourne Aug. 1969, Butterworths, London 1969

Nichols, F.A., Mullins, W.W., Trans. AIME 233, 1840 (1965)

Pearson, W. B., "Handbook of Lattice Spacings and Structures of Metals and Alloys, Vol. 2, Pergamon (1967)

Pearson, W. B., "The Crystal Chemistry and Physics of Metals and Alloys", Wiley - Interscience (1972)

Peter E.T., Ogilvie, R.E., Trans. AIME 233, 82 (1965)

Phillips, V.A., Acta Met. 14, 271 (1966)

Purdy, G.R., "Theory of Microstructure" from seminar, Sept. 1971 I.M.S. Denver, (1972)

Purdy, G. R., Met. Sci. J. 5, 81 (1971)

Rastogi, P.K., Ardell, A.J., Acta Met. 19, 321 (1971)

Read, W. T., Shockley, W., Phys. Rev. 78, 275 (1950)

Repas, P.E., Heheman, R. F., Tech. Report #6 to U.S. Office of Naval Research, 212(1967) Contract NONR 1141 (5) (1967)

Robertson, D., M.Sc. Thesis, McMaster University (1968)

Russell,K.C., Acta Met. 16, 761 (1962)

Russell,K. C., "Phase Transformations" American Society for Metals (1970) Ch. 6.

Schober, T., Balluffi, R.W., Phil. Mag. 21, 109 (1970)

Schober, T., Balluffi, R.W., Phil. Mag. 20, 511 (1969)

Schober, T., Balluffi, R. W., Phys. Stat. Sol. 44, 103 (1971); 44, 115 (1971).

Sekerka, R.F., J. Phys. Chem. Solids 28, 983 (1967)

Servi, I. , Turnbull, D., Acta Met. 14, 161 (1966)

Shewmon, P.G., Trans. AIME, 233, 736 (1965)

Sundquist, B.E., Acta Met. 12, 67 (1964)

Sundquist, B.E., Acta Met. 12, 585 (1964)

Swalin, R.A., "Thermodynamics of Solids", Wiley, New York, 1967, p. 120

Temkin, D.E., Doklady Akad. Nauk SSSR 132, 1307 (1960)

Tiller, W. A., Cdn. Met. Quart. 8, 77

Trivedi, R., Pound, G.M., J. Appl. Phys. 40, 4293 (1969)

Trivedi, R., Metall. Trans. 1, 921 (1920)

Trivedi, R., Acta Met. 18, 287 (1920)

Turnbull, D., "Impurities and Imperfections", American Society for Metals, 1955 p. 121

van der Merwe, J.H., Proc. Phys. Soc. 63A, 616 (1950)

van der Merwe, J.H., J. Appl. Phys. 34, 117 (1963)

Vaughan, D., Phil. Mag. 18, 1305 (1968)

Weatherly, G.C., Nicholson, R.B., Phil. Mag. 17, 801 (1968)

Weatherly, G.C,, Phil. Mag. 17, 791 (1968)

Weatherly, G.C., Met. Sc. Jr. 2, 237 (1968)

Weatherly, G.C., Cdn. Met. Quart. 8, 105

Weatherly, G.C., Sargent, C.M., Phil. Mag. 22, 1049 (1970)

Weatherly, G.C., Acta Met. 18, 15 (1970)

Weatherly, G.C., Acta Met. 19, 181 (1971)

Winterbottom, W.L., Gjostein, N.A., Acta Met. 14, 1041 (1966)

Winterbottom, W.L., Acta Met. 15, 303 (1967)

Winterbottom, W.L., Gjostein, N.A., Acta Met. 14, 1033 (1966)

Wulff, G., Z. Krist. 34, 449 (1901)

Zener, C., J. Appl. Phys. 20, 950 (1949)